Microstructure Evolution during Friction Stir Spot Welding of TRIP steel

Lomholt, Trine Colding

Publication date:
2013

Document Version
Publisher's PDF, also known as Version of record

Technical University of Denmark
Department of Mechanical Engineering

Microstructure Evolution during Friction Stir Spot Welding of TRIP steel

Ph.d. Thesis by

Trine Colding Lomholt

Supervisors:
Marcel A. J. Somers
Karen Pantleon
Alice Bastos da Silva Fanta

Preface

The present thesis is submitted in partial fulfillment of a Ph.D. degree from the Technical University of Denmark. The work presented in the thesis was carried out during the period August 2008 to October 2011 at the Department of Mechanical Engineering, under the supervision by Professor Marcel A. J. Somers and Associate Professor Karen Pantleon. Dr. Alice Bastos da Silva Fanta of DTU Center for Electron Nanoscopy has co-supervised the work on electron back-scatter diffraction. The project was part of the framework project Innojoint (Innovative joining processes applying integrated modeling), financially supported by the Danish Research Council for Independent Research, Production and Technology under grant 274-05-0232.

Kgs. Lyngby, October 2011

Trine Colding Lomholt

Abstract

Transformation Induced Plasticity (TRIP) steels have been developed for automotive applications due to the excellent high strength and formability. The microstructure of TRIP steels is a complex mixture of various microstructural constituents; ferrite, bainite, martensite and retained austenite. The TRIP effect is activated under the influence of an external load, thereby leading to a martensitic transformation of the retained austenite. This transformation induced plasticity contributes to the excellent mechanical properties of this class of steels and provides high tensile strength without deteriorating the uniform elongation. The unique deformation properties can be exploited in automotive applications for crash resistant parts due to the high energy absorption, thus improving passenger safety. Furthermore, the high strength and good formability permits the application of thinner sheet material and thereby reduced weight of the vehicles.

One of the limitations for the wide application of TRIP steel is associated with joining, since so far no method has succeeded in joining TRIP steel, without comprising the steel properties. In this study, the potential of joining TRIP steel with Friction Stir Spot Welding (FSSW) is investigated. The aim of the study is to assess whether high quality welds can be produced and, in particular, to obtain an understanding of the microstructural changes during welding.

The microstructure of the welded samples was investigated by means of reflected light microscopy, scanning electron microscopy and electron backscatter diffraction. Microhardness measurements and lab-shear tests completed the investigations of the welded samples and allow evaluation of the quality of the welds as seen from a practical point of view. Selected samples were also investigated by X-ray diffraction.

The complementary use of the various characterization techniques allowed subdivision of the microstructure in the weld in different zones: two thermo-mechanically affected zones (TMAZs), and two heat-affected zones (HAZs). The dual behavior of the microstructure in the

zones is related to the two transition temperatures in steel: Ac_1 and Ac_3. The following zones are identified; HAZ-lowT, HAZ-highT, TMAZ-lowT and TMAZ-highT.

In the HAZ-lowT zone the temperature is below Ac_1, where austenite transforms into bainitic ferrite and/or ferrite. On entering the HAZ-highT zone, the microstructure reaches an intercritical temperature, which upon cooling leads to a ferritic-martensitic microstructure. In the TMAZ-lowT the temperature was also in the intercritical range, but simultaneously the effect of deformation can be recognized. This leads to various transformations occurring in the ferrite phase. At relatively low strain, dynamic recovery takes place by means of fragmentation of grains and formation of subgrain boundaries. On approaching the weld center, deformation and temperature increase, which is associated with continuous dynamic recrystallization as the mechanism for formation of fine ferrite grains. Close to Ac_3, fine ferrite grains also develop from strain-induced transformation, which develop intragranularly in austenite. In the TMAZ-highT zone the temperature is above Ac_3, which formed an almost fully martensitic microstructure from recrystallized austenite grains. A narrow region of the TMAZ-highT parallel to the pin hole contains ferrite, which has developed as δ-ferrite or decarburization, or by a combination of the two mechanisms.

Resumé

TRansformation Induced Plasticity (TRIP) stål er udviklet til anvendelse i bilindustrien på grund af den fremragende kombination af høj styrke og formbarhed. Mikrostrukturen af TRIP stål er en kompleks blanding af mange mikrostruktur-dele: ferrit, bainit, martensit og austenit. TRIP effekten er aktiveret under indflydelse af ekstern mekanisk belastning, der fører til en martensitisk transformation af austenit. Martensit-dannelsen under deformation bidrager til de fremragende mekaniske egenskaber af TRIP stål såsom høj trækstyrke uden at den høje brudforlængelse reduceres. De unikke deformationsegenskaber kan udnyttes i køretøjer til de dele, der skal forhindre sammenkrølning under sammenstød som følge af høj energi absorption, og dette vil føre til øget sikkerhed for passagererne. Desuden betyder den høje styrke og gode formbarhed, at stålet kan fremstilles med en lavere godstykkelse og dermed reducere vægten af køretøjet.

En af begrænsningerne for anvendelsen af TRIP stål er forbundet med sammenføjning, da der hidtil ikke er fundet nogen acceptabel svejseteknik, der kan sammenføje TRIP stål. I dette studie undersøges muligheden for at anvende friktions punkt-svejsning til at sammenføje TRIP stål. Derudover er det et mål med dette studie at opnå en grundlæggende forståelse af de mikrostrukturelle ændringer, der sker under svejsningen.

Mikrostrukturen af det svejsede stål blev undersøgt ved hjælp af reflekteret lys optisk mikroskopi, scanning elektronmikroskopi og elektron backscatter diffraktion. Mikro-hårdhedsmålinger og lap-shear trækprøvning udgjorde en evaluering af kvaliteten af svejsningerne. Enkelte emner blev undersøgt med røntgendiffraktion.

Mikrostrukturen efter svejsning kan opdeles i to termo-mekanisk påvirkede zoner (TMAZ), og to varme-påvirkede zoner (HAZ). Opdelingen i to underzoner er relateret til de to overgangs-temperaturer i stål: Ac_1 og Ac_3. Følgende zoner er identificeret i dette studie: HAZ-lowT, HAZ-highT, TMAZ-lowT og TMAZ-highT.

I HAZ-lowT zonen var temperaturen under Ac_1, hvor austenit omdannes til bainitisk ferrit og/eller ferrit. I overgangen til HAZ-highT zonen, blev mikrostrukturen udsat for en interkritisk temperatur, som fører til dannelsen af en ferritisk-martensitisk mikrostruktur. I TMAZ-lowT zonen var temperaturen også i det interkritiske område samtidig med at deformation fandt sted. Det fører til forskellige transformationer i ferrit fasen. Ved relativt lav belastning, gennemgår ferrit *dynamic recovery*, hvilket sker som fragmentering af korn og dannelse af sub-korn. Tættere på svejsningens centrum stiger temperatur og deformationsgraden, hvilket fører til *continuous dynamic recrystallization*, hvilket medfører dannelse af fine ferrit korn. Tæt på Ac_3, udvikles der også fine ferrit korn gennem *strain-induced transformation*. I TMAZ-highT zonen var temperaturen over Ac_3, hvilket resulterer i en næsten fuldstændig martensitisk mikrostruktur. En smal region af TMAZ-highT, parallelt med hullet efter værktøjet, var der et indhold af ferrit. Dette kan fortolkes som dannelse af δ-ferrit eller afkulning nær overfladen eller ved en kombination af de to mekanismer.

Acknowledgements

First and foremost, I would like to thank my main supervisors Karen Pantleon and Marcel A. J. Somers for their invaluable support and for being a great inspiration throughout the Ph.D. project.

Alice Bastos da Silva Fanta, DTU Cen, is gratefully acknowledged for fruitful scientific discussions and supervision throughout the project. Also thanks to Yoshitaka Adachi for allowing me to spend two inspiring months with the group at NIMS in Japan.

Thanks to all of my colleagues from Section of Materials and Surface Engineering for assistance during my work, and for the good social atmosphere. My good friend and colleague Hossein Alimadadi is gratefully acknowledged for many scientific discussions and for pleasant company at the office.

Russell Steel and Jeremy Peterson from MegaStir Technologies are gratefully acknowledged for providing a welding facility and their expertise for the production of welds.

Special thanks to Cem Celal Tutum, Kim Lau Nielsen, Kasper Storgaard Friis, Chris Valentin Nielsen, Nils Elmegaard-Fessel, all from DTU, and Karsten Agersted Nielsen, Risø-DTU for assisting and providing knowledge about experimental work conducted during the project. Also thanks to Jacek Komenda, Swerea Kimab in Sweden for contributing with image analysis.

Finally, I will give my deepest gratitude to my beloved Henrik for endless support and encouragement throughout the making of the thesis.

Contents

List of Publications

P-1 T.C. Lomholt, K. Pantleon, M.A.J. Somers
Microstructure characterization of TRIP steel by means of complementary metallographic techniques
First draft is produced. The manuscript is planned to be published in Journal of Microscopy or Materials Characterization. The results are included in this thesis in Chapter 4.3.

P-2 T. C. Lomholt, Y. Adachi, A. Bastos, K. Pantleon, M. A. J. Somers
Gradual Transformation of Austenite in Al-Mn-Si TRIP Steel upon Tensile Straining; an In Situ EBSD Study
The manuscript was submitted on Oct 5th 2011 for publication in Acta Materialia. At the deadline of the thesis, the review process was still ongoing. The results are included in this thesis in Section 5.1.

P-3 Trine C. Lomholt, Karen Pantleon, Marcel A. J. Somers
Mikrostruktur udvikling i TRIP-stål under Friction Stir Spot svejsning
Dansk Metallurgisk Selskabs Vintermøde, Göteborg, Sweden, 2010.

P-4 Trine C. Lomholt, Karen Pantleon, Marcel A. J. Somers
Microstructure Evolution during Friction Stir Spot Welding of TRIP Steel
8th International Symposium on Friction Stir Welding, Timmendorfer Strand, Germany, 2010.

P-5 T.C. Lomholt, J. Peterson, R. Steel, K. Pantleon, M.A.J. Somers
Friction Stir Spot Welding of TRIP steel
JOM16 - Joining of Materials, Tisvilde, Denmark, 2011.

P-6 Trine C. Lomholt, Yoshitaka Adachi, Jeremy Peterson, Russell Steel, Karen Pantleon, Marcel A.J. Somers
Microstructure Characterization of Friction Stir Spot Welded TRIP Steel
Thermec 2011, Quebec, Canada, 2011.

Abbreviations

AHSS	Advanced high strength steels
AWS	American welding society
b.c.c.	Body-centered cubic
b.c.t.	Body-centered tetragonal
BEI	Backscattered electron imaging
BF	Bright field
BM	Base material
CBED	Convergent beam electron diffraction
CDRX	Continuous dynamic recrystallization
CI	Confidence index (TSL OIM analysis software)
CR	Cold rolling
DF	Dark field
DP	Dual phase
DRV	Dynamic recovery
DRX	Dynamic recrystallization
EBSD	Electron backscatter diffraction
EDS	Energy-dispersive x-ray spectroscopy (or EDX)
f.c.c.	Face-centered cubic
FIB	Focused ion beam
FSSW	Friction stir spot welding
FSW	Friction stir welding
FWHM	Full-width half maximum (XRD term)
GAIQ	Grain Average Image Quality (TSL OIM analysis software)
GAM	Grain Average Misorientation (TSL OIM analysis software)
GROD	Grain Reference Orientation Deviation (TSL OIM analysis software)
GSAR	Grain shape aspect ratio (TSL OIM analysis software)
HSS	High strength steels

HAGB	High angle grain boundary (>15°)
HAZ	Heat-affected zone
IF	Interstitial free
IPF	Inverse pole figure
IQ	Image quality (TSL OIM analysis software)
KAM	Kernel Average Misorientation (TSL OIM analysis software)
K-S	Kurdjumov-Sachs
LAGB	Low angle grain boundary (<15°)
LD	Loading direction
LW	Laser welding
ND	Normal direction
ODF	Orientation distribution function
ppm	parts per million
PCBN	Poly crystalline boron nitride
Q & P	Quenching and partitioning

1 Introduction

In a time with persistent focus on the environment it is of greatest importance for the automotive industry to reduce the fuel consumption and fuel emissions. Weight reduction is an important approach for the reduction of fuel consumption but also an improved passenger safety is of high priority. In recent years, the focus on passenger safety and the ability of the materials to withstand the high impacts during crash have increased. High strength steels meet all these requirements by their superior mechanical properties where a combination of high strength and good formability allows a reduction in sheet thickness without assigning lower priority to the formability. Transformation-induced plasticity (TRIP) steel is a high strength steel with improved properties due to the deformation-induced austenite-to-martensite transformation. The martensite formation contributes to a higher tensile strength without deteriorating the uniform elongation, and it results in mechanical properties of TRIP steels, which are unique and highly improved compared to other high strength steel grades [1][2]. TRIP steels are of greatest interest for the automotive industry but the limitation for the wide application of TRIP steel is associated with joining. Weldability problems are found by using regular fusion welding processes for joining of TRIP steel, and friction stir welding (FSW) and friction stir spot welding (FSSW) are promising welding techniques allowing TRIP steel to be used in vehicles.

In this Ph.D. project, the feasibility of joining TRIP steel with FSSW is investigated. It is the aim to verify if FSSW is suitable to produce strong and reproducible welds in TRIP steel. The two main parameters to control during friction stir spot welding are the rotational speed of the tool and the dwell time of the tool before retracting from the weld. Variations in the two main parameters were performed and the influence of the parameters on the microstructure and mechanical properties were investigated. Furthermore, detailed microstructure characterization of one selected weld is performed, with the aim of verifying the mechanisms occurring in the microstructure during FSSW. FSSW is a complex process involving a combined action of heat and deformation and it is also of interest to investigate the effect of heat and deformation

individually. TRIP steel base material was heat treated to different temperatures and subsequently characterized to determine the phase transformations occurring at the various temperatures. Deformation of TRIP steel base material was investigated by an in situ tensile test, to investigate the microstructural changes during deformation without the influence from heat. The transformation from austenite to martensite is the main effect of interest to investigate during deformation. The studies of the individual effects of temperature and deformation are intended for a better understanding of the microstructure changes in TRIP steel from heat and temperature, respectively, and it will enable a better understanding of the microstructure evolution during FSSW.

The experimental work conducted in this Ph.D. project can be subdivided into four chapters:

- **Chapter 4:** the TRIP steel base material is investigated. The characterization and identification of micro-constituents in a TRIP steel base material is not straightforward due to the complex microstructure. Various preparation methods were investigated for the various characterization techniques, and by the comparative use of several techniques, the microstructure was characterized.
- **Chapter 5**: The individual effects of heat and deformation on TRIP steel are described.
- **Chapter 6:** A comparable study of all welds for the comparison of properties and quality. Mechanical tests were conducted and held together with cross sections showing the width of the weld zones. Modeling of the thermal behavior during welding contributed to the determination of temperature spread in the regions in and around the weld, as a function of the welding parameters. The investigations yield to a recommended choice of weld parameters for optimal weld properties.
- **Chapter 7:** The fundamental understanding of the microstructure evolution during welding is an essential part of the thesis. In this chapter, a thorough investigation of one selected weld is described. The chapter will apply numerous characterization techniques and by the comparative use, provide an understanding of the phase transformations occurring during welding.

All chapters will include discussions of the observations and comparison with reports from the literature.

2 Background

2.1 TRIP steel

2.1.1 Classification and application

TRIP steels belong to the class of automotive steels known as Advanced High Strength Steels (AHSS), which covers steels with a minimum tensile strength of 500-800 MPa [2]. The relationship between tensile strength and elongation of some common automotive steels are shown in Fig. 2-1.

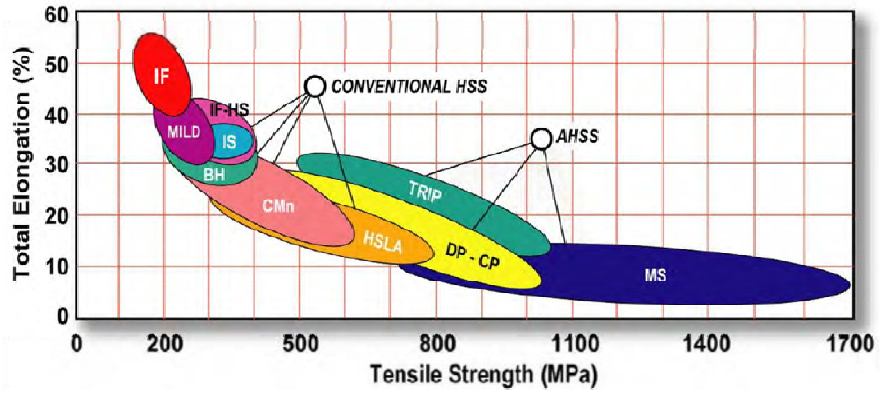

Fig. 2-1. Relationship between ultimate tensile strength and total elongation for various automotive steel grades [2].

It is seen from the diagram that the AHSS grades possess a combination of higher strength and elongation compared to the conventional high strength steels (HSS). The microstructure of

conventional HSS consists of a pure ferritic microstructure, whereas AHSS has a ferritic matrix and, additionally contains one or more other phases, such as martensite, pearlite, austenite etc. TRIP steels contain ferrite, bainite, retained austenite and martensite. The deformation behavior of TRIP steel is unique due to the austenite-to-martensite transformation occurring upon deformation, which gives a very high and uniform elongation. As seen in Fig. 2-1 TRIP steel has a high strength and concurrently the elongation is high as compared to the other AHSS grades in the diagram. TRIP steels are indeed the most formable steel in the strength level higher than 500 MPa because of the TRIP effect [2][3].

2.1.2 Processing

The microstructure of TRIP steel can be obtained by mainly two different heat treatment processing routes. In Fig. 2-2 is shown illustrations of the time-temperature scheme for the two processes.

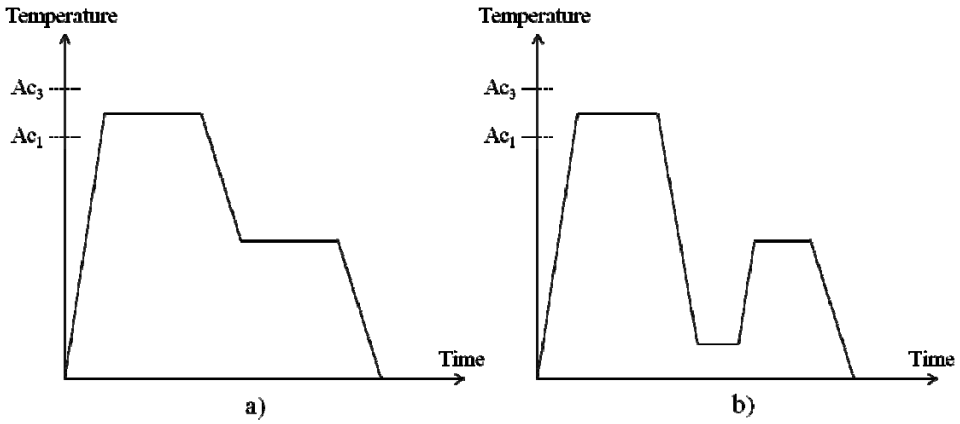

Fig. 2-2. Two common processing routes for the production of a TRIP steel microstructure. In a) is shown the conventional process [4][5], and in b) the quenching and partitioning process [6].

The most common heat treatment procedure applied for the production of TRIP steel is the process in Fig. 2-2 a) whereas the quenching and partitioning (Q & P) process in b) is an alternative and a relatively new technique. The overall principle of the two processes is comparable since both heat treatments are split in two processes. First, the material is annealed between Ac_1 and Ac_3 to dissolve the original microstructure, which is commonly pearlite. During the annealing, austenite grains are growing and after a certain time, the microstructure has transformed into pure austenite and ferrite. This annealing step is also known as intercritical annealing due to the temperature between Ac_1 and Ac_3. After the intercritical annealing the steel

is rapidly cooled to a temperature between 375°C and 450°C, where bainite will form. This step is also known as intermediate aging, and the temperature is called the bainite holding temperature. Under the bainitic ferrite formation, carbon is redistributed from bainitic ferrite into the surrounding austenite, thereby contributing to the stabilization of the retained austenite in the final microstructure. The heat treatment procedure ends with a final cooling to room temperature without considerable martensite transformation [4][7][5][8][9]. The Q & P process differs from the conventional TRIP steel processing in the cooling step from intercritical annealing. Instead of quenching directly to the intermediate aging temperature, quenching is performed to a lower temperature (100-200°C), before heating up to the intermediate aging temperature again. The quenching temperature is between M_s and M_f, thereby giving a mixture of austenite and martensite, and in the aging treatment (called partitioning in the Q & P process), carbon is transferred from the supersaturated martensite into austenite [6][10]. The temperatures for annealing and aging are in principle similar for the two processes but the lower quenching temperature in Q & P makes the difference. After the Q & P procedure the TRIP steel microstructure contains carbon-depleted martensite instead of bainite, thereby giving a higher strength than conventional TRIP steel but maintaining the good formability because of the retained austenite [10].

TRIP steels are produced as thin steel sheets, and the sheet geometry is obtained by hot or cold rolling. Cold rolling is performed on the initial steel before performing the heat treatments described above. Hot rolling is a relatively new process for TRIP steels, which can be applied during the intercritical annealing process, and it is expected to improve the mechanical properties of the steel due to enhanced nucleation of ferrite and bainitic ferrite during heat treatment. [11][12][13][14]. However, cold rolling is still the most used process for forming the TRIP steel sheets.

The final step in the processing of TRIP steel is to form the sheets into the shape to fit to the application. There is a risk of austenite-to-martensite transformation occurring when forming the sheets, which will reduce the amount of retained austenite available for transformation in the TRIP steel in case of a crash [15]. As a result, it is important to optimize the processing of TRIP steel in order to retain the austenite until the transformation is wanted in the application. Not only processing is important to optimize, also the composition of the steel is critical for the final microstructure. If the aging time and temperature is too high, austenite becomes too stable and the TRIP effect is lost. Furthermore, the precipitation of cementite will occur if the aging time is too high.

Due to the poor corrosion properties of the low alloyed TRIP steels, the steel sheets are normally manufactured with a protective Zn coating. It is either hot dip galvanized or electroplated with Zn.

2.1.3 Composition and microstructure

TRIP steels are generally low alloy steels with a relatively low carbon content (0.1-0.5 wt%) but they can also belong to the group of austenitic stainless steels containing high amounts of Cr and Ni [1][5][16]. Only low alloyed TRIP steel is treated in the present study, so only this type of steel will be described. The multiphase microstructure of TRIP steel is obtained by the advanced heat treatment procedure as described in the previous chapter, and only a few alloying elements are needed to obtain the microstructure in TRIP steels. The most important and frequently used alloying elements in TRIP steels are; C, Si, Al and Mn.

C plays a central role for the properties of TRIP steel but the main purpose is to retain austenite, which is accomplished through the adjustment of the M_s temperature.

Si and Al are ferrite stabilizers and contribute to hardening by solid solution hardening but the most important property of Si and Al is the prevention of cementite precipitation. Hence, during the intermediate aging temperature, bainite is formed as a combined structure of austenite and bainitic ferrite. The formation of bainite is normally associated with cementite precipitation but it can be avoided by the addition of Si and/or Al. Si and Al slow down or prevent the precipitation of cementite and instead austenite is enriched with carbon, and thereby retained upon cooling to room temperature. Si creates oxides on the surface, which has a detrimental effect on the adhesion of galvanic coatings. Therefore, Si is unwanted for the automotive industry. Si can be replaced by Al but the cementite preventing effect is weaker for Al than for Si. A partial substitution of Si with Al gives excellent mechanical properties [17], whereas a full substitution has lead to deterioration of the strength/ductility balance [7]. The solid solution hardening of Al is also significantly lower than that of Si [8].

Mn is an austenite stabilizer and also improves the hardenability by solid solution hardening [5]. Furthermore, Mn increases the C solubility in ferrite, which also leads to higher hardness. The content of Mn is normally less than 2.5 wt% [18] because a higher content will lead to segregation and thereby formation of a banded structure of austenite grains in the microstructure. New developments of TRIP steels include an increased Mn content of up to 7 wt%, to improve the strength and ductility even further [19][20]. However, only the typical low alloyed TRIP steels will be considered in the present study.

A typical low alloyed TRIP steel microstructure contains four main micro-constituents, which are listed in Table 2-1.

Table 2-1. The four common micro-constituents in TRIP steels.

Micro-constituent	Symbol	Crystal structure
Ferrite	α	b.c.c.
Retained austenite	γ	f.c.c.
Bainite	$\alpha_b + \gamma$	b.c.c.+ f c.c.
Martensite	α'	b.c.t. close to b.c.c.

The volume fraction of the micro-constituents in TRIP steel is highly dependent on composition, heat treatment and processing treatments and as a result, no general prediction of volume fractions of the micro-constituents can be made. The presence of martensite in the initial microstructure varies among different TRIP steels. If the aging time has not been sufficient to stabilize the austenite grains, they will transform into martensite upon cooling. If aging has been sufficient, austenite has been enriched with carbon thereby lowering the M_s temperature and the martensite transformation is inhibited during cooling.

Fig. 2-3 shows the microstructure of two different TRIP steels.

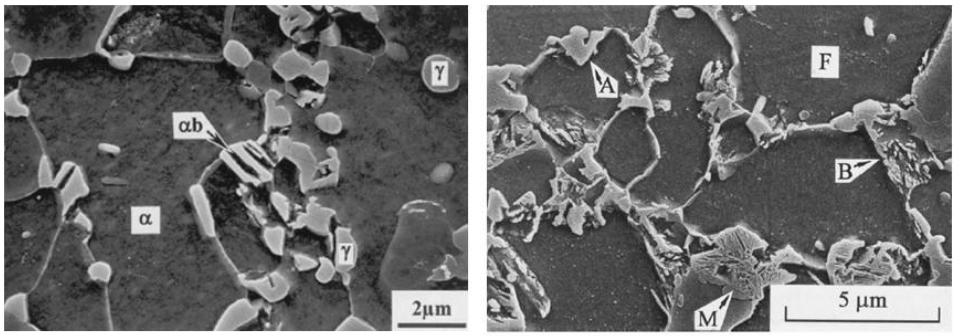

Fig. 2-3. SEM micrographs of two different TRIP steels [7][21].

In the transition from intercritical annealing to intermediate aging there is a shift of the growth mechanism from austenite. During cooling from intercritical annealing, the transformation from austenite occurs reconstructively into ferrite. When the temperature is lowered to intermediate aging, the transformation changes into a displacive growth to bainitic ferrite [8][22]. The change of transformation mechanism can be identified by two changes in the microstructure: first, a slight change of orientation from ferrite to bainitic ferrite, which appears in the form of a diffuse small angle grain boundary between bainitic ferrite and the ferrite. Second, there is an increased dislocation density in the bainitic ferrite due to the shape and volume change occurring during growth of bainitic ferrite [8]. Fig. 2-4 illustrates the alignment of the micro-constituents in TRIP steel, and the shift in growth mechanism between ferrite and bainitic ferrite is also seen in the illustration.

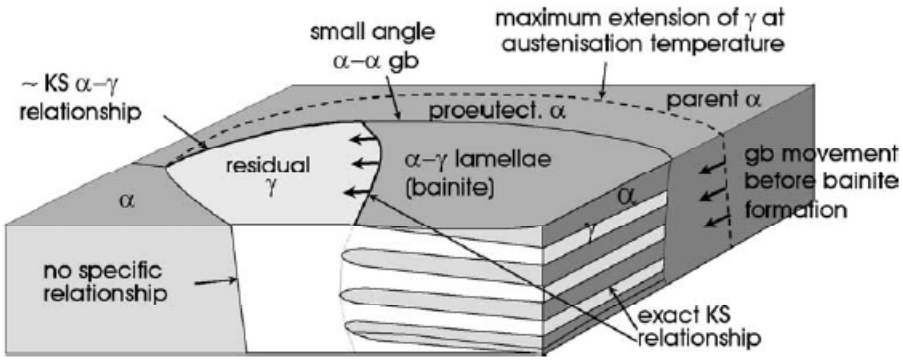

Fig. 2-4. Illustration of TRIP steel microstructure [8].

The hardness varies for the micro-constituents in TRIP steel, which is mainly controlled by the carbon content. In [23] the hardness was measured with nano-indenter in the various microconstituents of a TRIP steel, and the results is seen in Fig. 2-5.

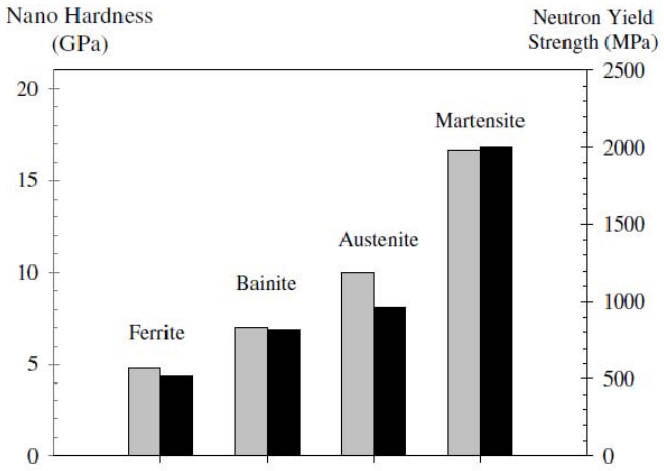

Fig. 2-5. Hardness of the micro-constituents, as measured in [23]

The graph shows the nanohardness of the individual phases in TRIP steel. Although the hardness cannot be directly compared with other TRIP steel grades, because it is strongly affected by the composition, the relative hardness of the phases compared to each other can be used. The results are confirmed by [24], where it is found that the hardness increases as follows: ferrite, bainite, austenite, and martensite.

2.1.4 Welding of TRIP steel

One of the limitations for the wide application potential of TRIP steel is associated with joining. Until now, there have been many investigations in the literature with the aim of finding a suitable welding method for TRIP steel but with no success. Regular fusion welding techniques face problems, which will be presented in the following.

Resistance spot welding currently the most frequently used spot welding process in car assembly operations [25]. Laser welding is also very frequently used in vehicles, and the use of laser welding is increasing due to the huge development in the field currently [26]. Gas metal arc welding techniques are used to a lesser degree. These welding techniques are all fusion welding techniques, which involve melting of the material in the nugget.

Joining of TRIP steel has been a field of major concern in the recent years, and fusion welding has been widely studied as a potential candidate for joining of TRIP steel. Many studies have been published, but there appear to be many problems associated with joining of TRIP steel with the various fusion welding techniques. One problem, which has been reported very often is the formation of inclusions or oxide particles in the welds of gas metal arc, laser and resistance welding. Particularly, oxides of Al or Si tend to form during the melting process. Furthermore, there are problems associated with the formation of delta ferrite in parts of the melted zone leading to a softened zone [27][28][29][30]. Porosities have also been observed after gas metal arc welding or laser welding [31].

There have been many attempts to improve the properties of fusion welds in TRIP steels by adjusting the welding technique. For laser welding an increased welding speed and the use of shielding gas has an improving effect by reducing the porosity fraction [31]. Resistance welding in TRIP steel can be improved by optimization of the welding parameters such as welding current, time and force but still inclusions are formed [32]. In resistance welding, pre-and post-weld heat treatments have been found to improve the mechanical properties of the welds [33] [34][35]. Despite the many attempts to improve the fusion welding techniques for joining of TRIP steel, many problems remain unresolved.

2.1.5 Feasibility of joining TRIP steel with FSSW

FSSW has already gained some interest in the literature as a potential joining technique for TRIP steel and a few studies have been published. The feasibility of FSSW in TRIP steel can be shown by comparing the shear tension strength of the welds of FSSW, resistance welding (RW) and laser welding (LW). The comparison is shown in Fig. 2-6, as a function of the sheet thickness of the steels. The black curve in the graph is the minimum required shear tension strength as specified by the American Welding Society (AWS) [36].

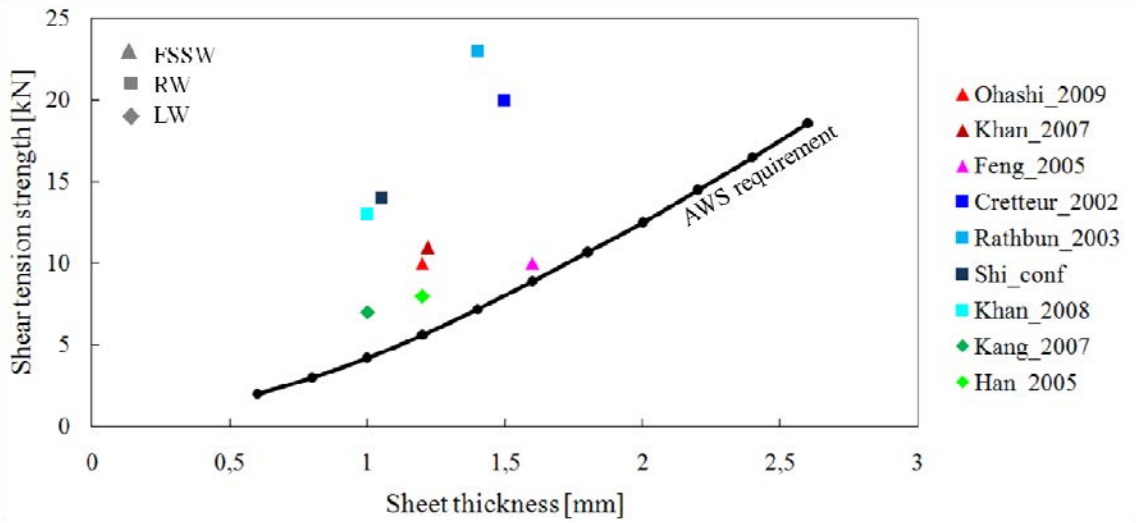

Fig. 2-6. Shear tension strength of spot welds of TRIP steels and DP steels [33][37][34][25][26][31][38][39][40]. All steels have a minimum tensile strength of 600 MPa. The minimum required shear tension strength, as specified by AWS, is also included in the graph [36].

Due to the limited number of welding studies of TRIP steel [33][37][34][25][26][31], also results on dual-phase steel are presented in the graph [38][39][40]. It is observed from the graph that the strength of the welds after FSSW meet the strength after RW and laser welding, and more important, fulfills the requirements for spots welds for the automotive industry. It is therefore considered to be acceptable to implement FSSW as a welding method for these steel grades.

From Fig. 2-6 it is observed that the fusion welds generally have a higher strength than FSSW but there are many other advantages of FSSW compared to fusion welding, which do not appear from the graph. The formability is better after FSSW, and one study reports on a 20% better formability of FSSW compared to laser welding [41]. In another study, the hardness distribution was found to be much more uniform after FSW compared to fusion welding, in DP steel [41]. Porosities are never reported to be found in welds of FSSW, and neither delta ferrite is observed, which is most likely caused by the lower temperature in FSSW. In a few recent publications TRIP steel was successfully joined with FSW and FSSW, which also supports the above findings that FSSW is a promising joining method of TRIP steel [42][43].

Not only are the properties of the weld important for the feasibility of FSSW, also the energy consumption and investment costs must be competitive. FSSW requires only 2.5% of the energy needed for a laser weld, which is a crucial advantage for the automotive industry due to the huge number of welds in one vehicle [44]. It was also reported in another study that shifting from RW to FSSW yields a reduction of 90% in energy and 40% in investment costs [45]. One significant drawback of FSSW is the duration of each weld cycle, which takes significantly longer time for

FSSW compared to any of the fusion welding techniques. If the economic and ecological advantages are so competitive, the importance of weld cycle time can be compromised.

2.2 Friction Stir Spot Welding

2.2.1 Friction Stir Welding

Friction Stir Welding (FSW) was patented in 1991 by The Welding Institute (TWI) in UK [46]. The process was originally invented for joining of aluminum and aluminum alloys, which are very difficult to join by traditional welding techniques [46]. In the past decades the welding technique has been applied to a wider range of materials.

FSW is a solid-state joining process where a non-consumable rotating tool is inserted into the workpiece, and the friction created between tool and workpiece generates heat and the material adjacent to the tool is softened. The localized region of softened material is moved around the tool under a plastic flow resulting in a solid-phase bond between the materials to be welded. The particular advantage of FSW as compared to conventional fusion welding processes is the temperature, which is held below the melting temperature. As a result, the properties of the joint are improved because some of the problems associated with melting in the weld are avoided. Some of the most outstanding advantages of FSW compared to conventional fusion welding processes are [44][47]:

- Good metallurgical properties of the weld
- Good mechanical properties of the weld
- Reduced amount of stresses
- Low distortion of the workpiece after welding
- No loss of alloying elements
- No preparation of the surface before welding
- No air pollution or ultra violet light emission
- Hydrogen cracking is reduced
- Shielding gas is not always necessary

While most efforts to date have focused on joining aluminum alloys, there is a considerable interest for joining other materials such as magnesium, titanium, copper, and their alloys [48][44]. FSW also enables joining of polymers, dissimilar materials [49][50][51] and composites [52][53], which so far has been associated with huge constraints when applying

conventional welding processes. Joining of steel with FSW was investigated for the first time in 1999 [54] but the technique has not progressed as rapidly as it has for aluminum. This is mainly caused by two reasons: high demands on the tool and the presence of many competitive techniques for joining of steel. Some niche applications are nevertheless being considered, where conventional welding processes are not suitable. In the automotive industry steel sheets are normally joined by regular spot welding techniques such as resistance welding or laser welding but newly developed high strength steels are not joinable by the fusion welding processes and spot FSW is a potential candidate to replace the conventional joining techniques.

2.2.2 Friction Stir Spot Welding

Friction stir spot welding (FSSW) is a spot variant of FSW applied to a lap joint consisting of an upper and lower plate. There are several versions of FSSW, such as Refill FSSW and Swing FSSW [47] but only the pure FSSW technique is considered in the present study. A schematic illustration of FSSW is shown in Fig. 2-7.

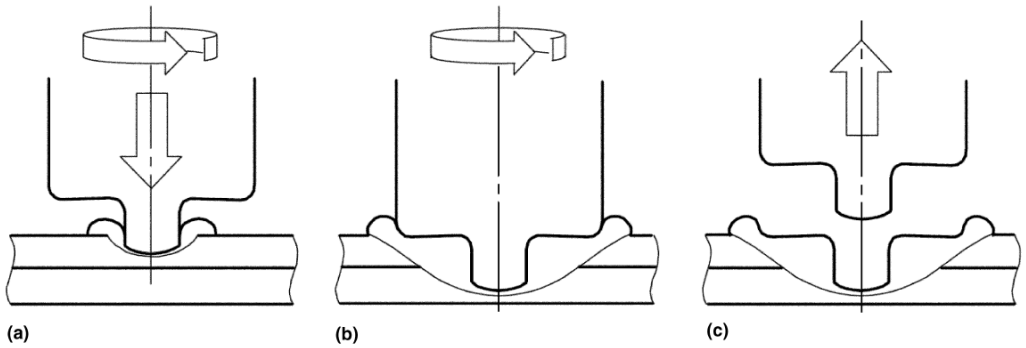

Fig. 2-7. Schematic illustration of FSSW [47].

Similar as in FSW a rotating tool is plunged into the workpiece but there is no linear movement of the tool as there is in FSW. The rotating tool is held in the workpiece for a certain time before it is retracted, the so-called dwell time. When the tool is retracted from the workpiece, a hole is left in the weld after the tool. As is normally the case for spot welds, only overlapping joint configurations are possible. The setup for FSSW also includes a backing plate below the workpiece, to support the downward force, and to conduct heat away from the workpiece.

The bonding region between the sheets is very narrow because of the presence of the pin hole, and therefore it is of outermost importance in FSSW to optimize the bonding region between the two plates in order to obtain the highest strength of the weld. The strength of the weld can be increased by creating a larger bonding region but it can also be done by producing a certain

microstructure in the bonding region. The adjustment of the microstructure in the weld is obtained by a range of weld parameters.

There are many parameters to vary in FSSW; the most important are listed in Table 2-2.

Table 2-2. Weld parameters in FSSW.

Welding	Tool	External factors	Pre- or post treatment
Rotation speed	Material	Shielding gas	Preheating
Dwell time	Design	Cooling of workpiece	Post-heat treatment
Plunge rate	Tool cooling		Post-surface treatment
	Tilt		

2.2.3 Welding parameters

Rotation speed

In FSW of steels it is generally recommended to keep the rotation speed low in order to preserve the original properties of the steel [55][56]. A rotation speed lower than 500 rpm is recommended for FSW of low carbon steel [55][57]. These recommendations apply for linear FSW, where the traversing movement of the tool contributes to the stirring of the material around the tool. These recommendations are not applicable for FSSW. Only very little is reported in the literature about varying the rotation speed in FSSW of steel but there is a study dealing with FSSW of low carbon steels and low alloy steels and they conclude that increasing the rotation speed to 1500 rpm and higher will create better welds [40][43]. However, the studies in the literature are not very extensive and the effect of the rotation speed on the microstructure evolution in the weld is not fully understood.

Dwell time

The dwell time is also a significant parameter for the microstructure evolution and bonding length in FSSW. A longer dwell time is expected to induce a larger heat generation in the weld because there is more time for the tool to generate heat in the weld. In the literature, there are only a few studies, which describe the effect of dwell time on FSSW of steel. In [58] a dual-phase steel is joined with FSSW applying dwell times from 0-4 seconds and it was found that a higher dwell time induced a higher bonding length and higher tensile strength. In [43] a dwell time of 2-3 seconds was applied for joining TRIP steel with FSSW but no significant effect of the dwell time variation was found.

In [59] Al and steel were joined by FSSW and it was found that a longer dwell time gave increased tensile shear strength, but also a higher quantity of intermetallic compounds, which

have a detrimental effect on the weld. The formation of intermetallic compounds originates from Al and not steel but there can be other unknown detrimental effects when increasing the dwell time. For instance, the contact between tool and workpiece during rotation can be lost at higher dwell times whereby the effect of extra applied dwell time is lost. Another drawback of increasing the dwell time is that the process time is increased. A normal vehicle contains more than 7000 spot welds [60] and the dwell time cannot be endlessly increased without regard to economics.

Plunge rate

The plunge rate is a parameter, which has not received much attention in the literature. During plunging of the tool into the workpiece, the tool and workpiece are heated up. A higher plunge rate will give a higher heating rate and the microstructure is more rapidly affected in the beginning of the weld cycle. A fast plunge rate will also induce more wear on the tool because the material is less softened in the initial plunging stage. It is not yet understood how significant the plunge rate is on the resulting microstructure since it is not investigated in the literature.

Tool

There are high demands on the tool used for joining of steel. The major reason for this is the higher melting temperature and yield strength of steel compared to aluminum. Degradation of the tool is by far the most limiting factor for the development of FSW and FSSW of steels. Many materials have been investigated as a candidate for the tool, and basically there are two types of tools; metal-based and ceramic tools. The metal-based tools include W, Re, W-Re, WC-Co and Mo-based materials, which all have been investigated as tool materials for FSW and FSSW of various steel grades. It is recognized that wear occurs in most of the studies with the metal-based tools [61][15][62]. The ceramic tool materials include Si_3N_4, TiC/TiN and polycrystalline boron nitride (PCBN) [40][44][42][63] and the most common problem with these tools is fracture of the tool due to the brittle nature of the ceramics [64]. According to the recommendations in the literature, the most promising tool material is PCBN [40].

The tool consists of a pin and a shoulder, as illustrated in Fig. 2-8.

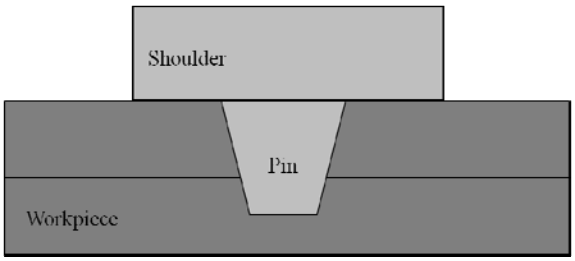

Fig. 2-8. Simple schematic illustration of the tool.

The shoulder generates most of the heat while the pin creates the material flow in a combined action with the shoulder [47]. The length of the pin is desired to be halfway through the lower plate for the optimum stirring in the workpiece. The design of the tool is a critical parameter for the outcome of the weld since the material flow around the pin is highly dependent on the design. However, since no optimum material has been found yet, the development and design of the tool has been very limited. Due to wear of the metal-based tools, complicated designs are not feasible because small details will easily break off. For the ceramic-based tools, complicated designs are restricted by the production process involving sintering, which complicates the creation of detailed designs. Therefore, the design of the tool is highly restrained by the material, and it is a field with a huge need for improvement.

Summary of parameters

Rotation speed and dwell time are the key parameters for the size of the stirred zone during welding, and these are investigated in this study. The plunge rate is also of high importance for the weld outcome, but was not investigated in this study because it is considered a second-order parameter. From the literature the recommended tool material is PCBN with a simple design, which is used in this study. Shielding gas is recommended in order to avoid oxidation during welding, and this was also employed in the present study. In the automotive industry, the main criterion for welding is that it has to be a fast and simple process. As a result, the external weld parameters such as cooling of workpiece during welding, preheating, post-welding heat treatment and post-weld surface treatment are not recommended, and therefore not investigated in the present study.

2.2.4 Material flow

The material flow during FSW is widely studied in the literature but the knowledge cannot be directly transferred to FSSW [51][65][66]. Only a few studies have investigated the material flow during FSSW and a simple illustration is shown in Fig. 2-9.

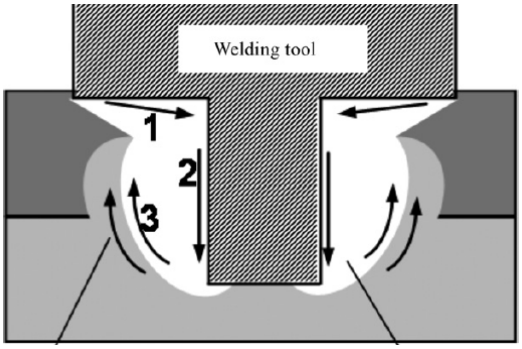

Fig. 2-9. Illustration of material flow during FSSW [67].

It is seen from the illustration that there is a downward material flow closest to the pin (2), and further away from the pin the flow is upwards (3). Just below the shoulder the material flow is moving towards the pin (1). The model is very simple and based on a simple tool geometry. By applying other geometrical shapes of the tool, the material flow will be different and it is complicated to predict the difference. Therefore, the flow illustrated in Fig. 2-9 shall be seen as an example of material flow with limited validity for other tool geometries.

2.2.5 Metallurgical zones in the weld

A schematic illustration of the cross section with indication of the zones in FSW is shown in Fig. 2-10.

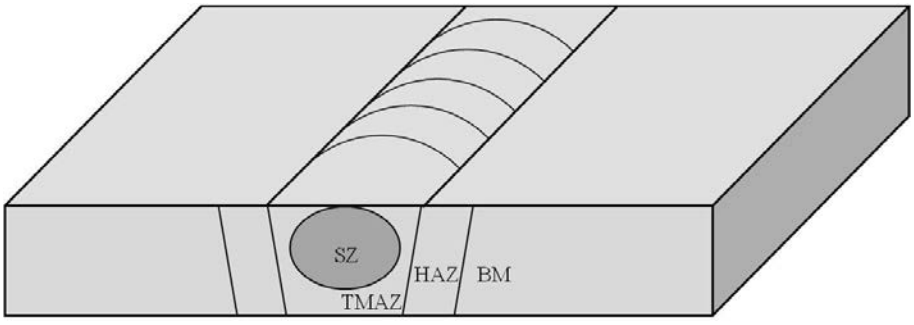

Fig. 2-10. Schematic illustration of the cross section after FSW (after [68]). SZ = stir zone; TMAZ = thermomechanically affected zone; HAZ = heat-affected zone; BM = base material.

The division of zones may change for some individual studies but the illustration in Fig. 2-10 is the most frequently reported with a recognized terminology for the zones. SZ is the stir zone

where fully stirring of the microstructure has occurred. TMAZ is the thermo-mechanically affected zone. One may suggest that the SZ is also a TMAZ but the general terminology in FSW acknowledges both zones where TMAZ is less mechanically affected than the SZ, which is fully stirred. HAZ is the heat-affected zone, and BM refers to the base material.

The cross section of the microstructure after FSSW is deviating from FSW because of the pin hole in the middle of the weld, created after retraction of the tool. Therefore, the SZ is not having the same size and shape in FSSW as it has in FSW. Still a TMAZ and a HAZ have formed in the regions around the pin hole, but the shapes and the widths of the zones differ. The identification of zones in the weld after FSSW is ambiguous in the literature but several studies have suggested an identification of zones, which counts for the particular materials used in the various studies. In Fig. 2-11 a cross section of dual-phase steel joined by FSSW is shown.

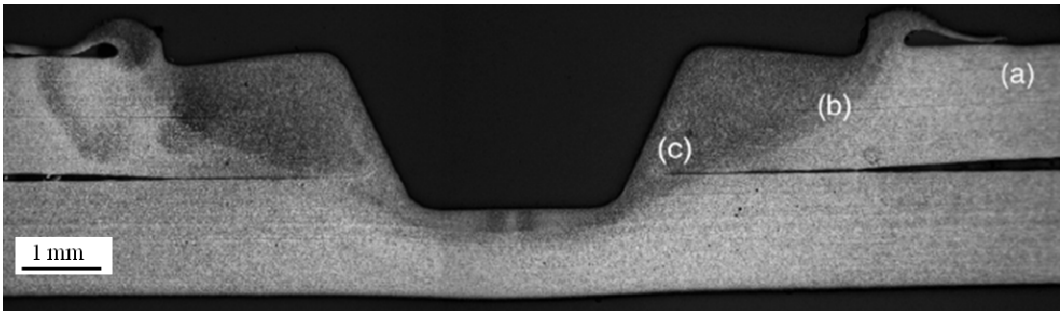

Fig. 2-11. Cross section of FSSW dual-phase steel from [40].

From the cross section image it is seen that the microstructure is divided into three zones. The zones are identified as BM (a), HAZ (b) and TMAZ (c). The characterization of the zones is not followed by a more detailed investigation of the microstructure. Consequently, it is not known, which changes have occurred in the microstructure during welding.

Fig. 2-12 shows a cross section of TRIP steel joined by FSSW.

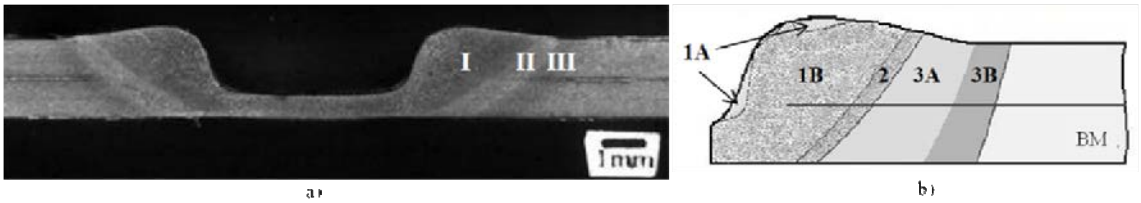

Fig. 2-12. Cross section of FSSW TRIP steel (a) and illustration with zone division (b) [43].

The division of zones in Fig. 2-12 is more detailed than in Fig. 2-11. Zone 1 is described as the SZ, which contains the subzones 1A and 1B due to inhomogeneities in the microstructure. Zone

2 is the TMAZ and zone 3 is the HAZ, which also contains two subzones; 3A and 3B. The two HAZs are found to be caused by a temperature above Ac_1 (3A) and below Ac_1 (3B). The study focused on the influence of the weld parameters onto the width and distribution of the zones rather than providing a deep metallurgical evaluation of the microstructure in the zones.

2.2.6 Peak temperature

The peak temperature during FSSW of steels is expected to be achieved in the interface between the tool and the workpiece. It is very difficult to measure the peak temperature in this position due to geometrical restrictions. Insertion of a thermocouple close to the pin is impossible because the microstructure is stirred and the thermocouple will break. Furthermore, when inserting a thermocouple in the workpiece, a small air gap will be formed between the workpiece and thermocouple, and the temperature is changed near the thermocouple. Another method to measure the peak temperature is by thermal imaging but this method is also combined with restrictions because the peak temperature is obtained in a very local region, which can be difficult to locate. The same restrictions are present in FSW but it is a field where more studies are conducted and therefore a wider range of papers are published on the subject. A list of studies on FSW where the temperature has been measured by different methods and in different locations is given in Table 2-3. Also some studies where the estimation of the temperature is based on microstructure evolution are included. All collected studies are from joining of steels, mostly low alloy steels, in order to enable the comparability with the TRIP steel investigated in the present study.

Table 2-3. Peak temperature during FSW of steel as reported in various literature studies.

Steel type	Measurement type	Location	Temperature	Ref.
Mild steel	Thermo couple	Close to SZ	1000°C	[62]
Low C steel, high C-steel	Estimation	SZ	Ac1-Ac3	[69][42]
High C-steel	Estimation	SZ	900°C	[70]
Stainless steel	Thermo couple	SZ	1200°C	[71]
Low C-steel	Thermo couple	Near shoulder	650°C	[72]
12% Cr steel	Thermal imaging	Near tool	1090 °C	[54]
Low C-steel, C-steel	Thermo couple	Bottom surface	650°	[73]
Low C-steel	Thermo couple	Bottom surface	600-900°C	[57]
Duplex SS	Estimation	-	1327°C	[74]

The temperature is obviously dependent on the welded material, welding parameters, tool material and tool geometry but it can be seen that the maximum temperature achieved is in the range of 1000-1200°C. It is reasonable to suggest that a similar peak temperature range can be reached during FSSW of steel.

Some of the studies from Table 2-3 have reported that welding in the intercritical region is better than in the austenite region, which can be achieved by lowering the rotational speed to 500 rpm and below [57][69][42]. Moreover, it has been reported that a very low carbon steel was successfully joined with FSW in the ferritic regime, which is accomplished because the carbon is very low and the rotational speed is kept low [48][73]. However, these recommendations are based on findings for FSW and not FSSW, and it is easier to decrease the rotational speed in FSW than in FSSW. Therefore, the recommendations on lowering temperature and rotational speed are not fully applicable in FSSW but it should be kept in mind when investigating optimal weld parameters for FSSW of TRIP steel.

2.2.7 Microstructure evolution

The changes occurring in the microstructure are indeed depending on the peak temperature reached in the weld. As described above, the peak temperature will most likely exceed 1000°C, depending on the weld parameters when joining low alloyed steels with FSSW. Furthermore, the microstructure evolution is strongly dependent on the initial microstructure and composition of the alloy, particularly the carbon content. In the literature, only a few studies are published on FSSW of steel and therefore some results on FSW will be included in following. The microstructure evolution occurring in linear FSW might for some studies be the same in FSSW but as described earlier, the weld parameters differ significantly due to the different weld geometry. Therefore, the knowledge obtained on microstructure evolution during FSW of steel cannot be completely transferred to FSSW but some of the principles are comparable.

In [40] martensitic steel and dual-phase steel were joined with FSSW. A cross section of the welded dual-phase steel was shown in Fig. 2-11, with three zones indicated; TMAZ, HAZ and BM. The identification of zones is similar for the two steels investigated in the study, and the peak temperatures and formed phases in the welded zones are also found to be similar for the two steels. The TMAZ was found to reach a peak temperature in the austenitic region, thereby leading to martensite/bainite upon cooling. The HAZ was found to be heated up to the intercritical range to form a mixture of austenite and ferrite, and upon cooling austenite will transform to martensite/bainite. No further discussion of the transformations is performed in the study.

In [75] a martensitic steel was joined with FSW. The microstructure in SZ was found to be fully martensitic due to a peak temperature in the austenitic region. Further analysis has revealed a smaller prior austenite grain size in the SZ. The grain refinement in the SZ is described to have formed during dynamic recrystallization. Two HAZs are identified in [75]: One HAZ in the intercritical region, where austenite and ferrite coexist, leading to a microstructure containing ferrite-pearlite after cooling. The other HAZ was exposed to temperatures below Ac_1 leading to tempered martensite.

High carbon steel was joined with FSW in [70]. The initial microstructure of the steel was having a fully pearlitic microstructure. The weld was divided up in three main zones; SZ, HAZ and BM, and SZ is further divided into two sub-zones, SZ-A and SZ-B. Both SZs contain a martensitic microstructure with some retained austenite grains. The retention of austenite is caused by the high amount of carbon in the alloy, which lowers the M_s temperature locally. In the outer subzone of SZ, SZ-B, there is also a content of cementite particles, which are described to have remained from the BM. In the whole SZ the temperature is concluded to have been in the pure austenite region but in SZ-B slightly lower than SZ-A.

In [73] ultra low-carbon steel with an initial microstructure being fully ferritic is welded with FSW. The microstructure in the SZ is fully ferritic but with a refined grain size and the grain refinement is explained to be caused by recovery of ferrite. The temperature range obtained in the SZ is not mentioned.

It is clear from the above described studies that the evolution of the microstructure during FSW and FSSW is strongly controlled by the initial microstructure. In most of the studies, the temperature distribution in the various zones is easily estimated from the microstructure observations but a fully understanding of the occurred phase transformations is generally not obtained. It is the aim of the present study to contribute to this understanding.

As a support to understand the possible phase transformations, the basic theory behind the effect of temperature and deformation will be treated in the Chapter 5 - Effect of deformation and heat on TRIP steel.

2.3 Effect of temperature and deformation on TRIP steel

FSSW is a thermomechanical process influencing the microstructure by a combined effect of increased temperature and deformation. The thermomechanical impact on the microstructure during FSSW of TRIP steel is not investigated deeply in literature but many studies have investigated the impact of the factors individually. Furthermore, the combined effect of temperature and deformation has been investigated to some extent but mostly in the field of thermomechanical processing of steels. In the following chapter an overview of literature findings on the individual effects of temperature and deformation is given, and also the thermomechanical influence during processing of steels is included. This should serve as a good starting point for the understanding of the effect of FSSW.

2.3.1 Temperature

The effect of temperature on microstructure has to be subdivided in effects associated with the temperature ranges below Ac_1, between Ac_1 and Ac_3, and finally above Ac_3.

Below Ac_1

When TRIP steel is subjected to temperatures below Ac_1, the effect on the microstructure is comparable with the intermediate aging step during processing of TRIP steels. It is anticipated that the aging will continue if TRIP steel is heated up to the aging temperature again. During intermediate aging bainite is formed which is accompanied by carbon enrichment in the neighboring austenite. The effect of aging time and temperature on the microstructure evolution in TRIP steels is widely investigated in the literature. When increasing the aging time, more bainite is formed and the carbon content in austenite is concurrently increased [7][21][76]. Fig. 2-13 shows the evolution of microstructure and carbon content in austenite as a function of the aging time.

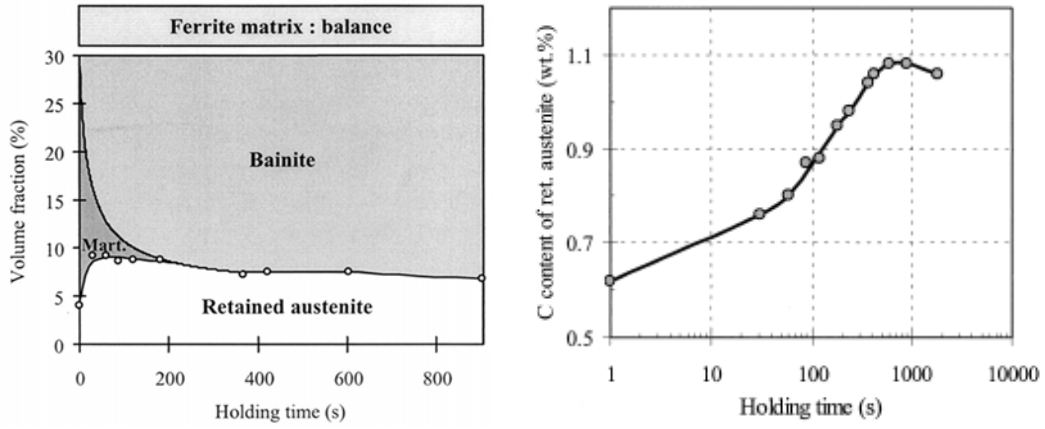

a) b)

Fig. 2-13. Evolution of the microstructure in TRIP steel (a) and carbon content in austenite (b), as a function of the aging time at 375°C [7].

It is clear from the two figures that bainite formation is increased by increasing the aging time, and the carbon content in austenite is also increased leading to more stable austenite grains. Furthermore, it is observed that at very short aging times (0-200 sec) martensite is formed because austenite is not sufficiently stabilized by carbon for short aging times. If the aging temperature is increased to 430 °C compared to 370°C, the same phases are found, but the transformation kinetics are faster and the amount of austenite is lower after shorter times [21][76].

After a long aging time and/or high aging temperature, the bainite formation will be fully proceeded and only ferrite and bainite-austenite will be present in the microstructure. Since bainite in TRIP steels is a combined structure of bainitic ferrite and austenite, it means that there is still austenite left, but it is only the highly stabilized austenite located as lamellae in between bainitic ferrite. As a result, the TRIP effect will disappear. It is also possible that cementite is precipitated in the carbon-rich austenite if aging is continued.

The intermediate aging applied for TRIP steels is in the range of 370 °C and 450 °C and does not cover the whole range below Ac_1. If TRIP steel is subjected to temperatures above the bainite formation temperature (but still below Ac_1), other phases than bainite will be formed, which can be seen from the TTT-diagram in Fig. 2-14.

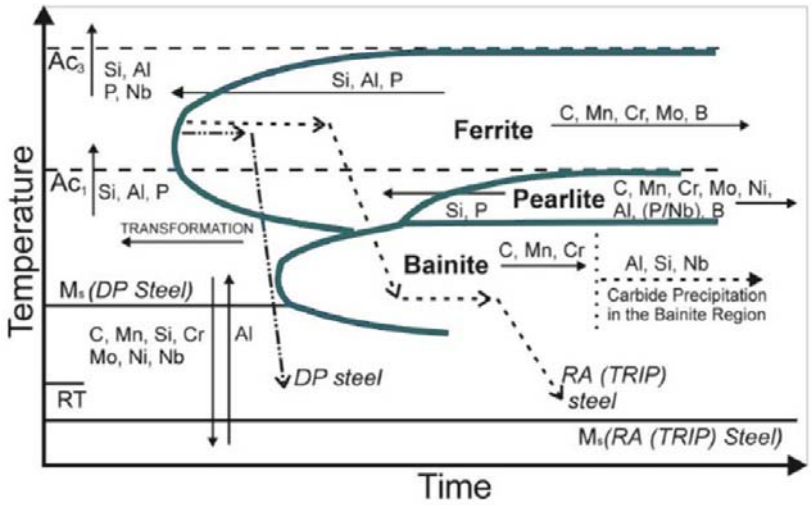

Fig. 2-14. TTT diagram of TRIP steel [77].

According to the TTT diagram a temperature in between bainite aging and Ac_1 will result in the transformation of austenite into ferrite, and at certain temperatures, also pearlite. If there is some martensite present in the TRIP steel in the initial condition, it will be tempered when the steel is subjected to temperatures below Ac_1 [1]. A tempering treatment of martensite will result in redistribution of carbon and possibly precipitation of fine carbides.

The lower limit for the temperature to influence the microstructure is not fully determined. The changes occurring at low temperatures are very small, and may not be detectable by conventional characterization methods. In one study TRIP steel has been heated up to 200°C for 2 hours and there were no detectable changes in the microstructure [21]. In another study the steel was heated to 260°C for 2.5 hours without changing the microstructure [78]. Both of the studies are using the low temperature heat treatment with the aim of making martensite visible on the polished microstructure after etching. The motivation for this method is that martensite is

tempered at this temperature and the morphology of the martensite grains are changed into a lamellar appearance. The conclusion from both studies is that martensite is tempered, but besides this effect, there are no other detectable changes in the microstructure upon exposing TRIP steel to 200-260°C.

Between Ac_1 and Ac_3

If TRIP steel is heated up to temperatures between Ac_1 and Ac_3, where austenite and ferrite is in equilibrium, parts of the steel will transform into austenite, and upon cooling be transformed into martensite or other phases depending on the cooling rate and local carbon content. A heat treatment in the intercritical region is comparable with heat treatment processes used to produce dual-phase steels. Dual-phase steels have a microstructure of ferrite and martensite, and they are produced by a heat treatment in the intercritical region, followed by quenching. Therefore, TRIP steel is expected to react similarly if exposed to temperatures in this region with regard to the cooling rate.

Above Ac_3

At temperatures above Ac_3, austenite is the only stable phase, and therefore it is expected that TRIP steel will be fully austenitized at this temperature. The degree of austenitization depends on time and temperature. Upon cooling, a range of phases can be formed from austenite, such as bainite or martensite, and it is controlled by the cooling rate.

The non-uniform carbon content in the TRIP steel microstructure will cause preferred regions for austenite formation at elevated temperatures. This is also the case for other alloying elements. The non-uniform preferred sites for austenite formation will also be present when exposed to temperatures between Ac_1 and Ac_3.

2.3.2 Deformation

When TRIP steel is subjected to an externally applied load the austenite transforms into martensite. This can occur by elastic straining of austenite, which is defined as stress-induced transformation, or it can be initiated after yielding of austenite, which is defined as strain-induced transformation [15]. During strain-induced transformation several mechanisms operate concurrently: Plastic yielding, stress partitioning among the micro-constituents and austenite-to-martensite transformation [15]. Plastic yielding in TRIP steel is a complex phenomenon due to the presence of the various micro-constituents, which have different yield strengths caused by the different crystal lattices and different compositions, most notably different carbon contents. It is well-known that ferrite as the softest phase will yield at relatively low applied stress

[15][79]. Stress partitioning occurs among the various micro-constituents as well as among the austenite grains, which, as a consequence of varying carbon contents, can vary in yield strength. It is commonly found that the austenite-to-martensite transformation occurs upon yielding of austenite. Austenite stability is recognized to have a particular influence on the deformation behavior of TRIP steel, and is affected by composition [15][79][78][80][81][82], grain size [15][78][80][83], grain shape [15] [78][84], location in microstructure [15][78][81][82], stress state [15], and the presence of precipitates [85].

The two most important factors for the austenite stability appear to be the carbon-content and the grain size [15][80]. The carbon content of the retained austenite grains is highly affected by the growth of bainite during processing, since the bainite formation occurs under the transfer of excess carbon from the bainitic ferrite to the adjacent retained austenite grains. A promoted bainite formation will lead to small and carbon-rich austenite grains sandwiched in-between lamellae of bainitic ferrite. A higher carbon content will lead to more stable austenite grains; if the carbon content exceeds about 1.8 wt% an incomplete transformation to martensite follows and consequently retained austenite does not contribute to the ductility of TRIP steel upon deformation [78][86]. Small austenite grains are not necessarily equivalent with a high average content of carbon in austenite, because also the rolling treatment and the concentrations of other alloying elements have an influence on the austenite grain size.

The volume fraction of austenite as a function of applied strain can be used as a quantitative measure to compare different literature findings. A collection of literature data is provided in Fig. 2-15.

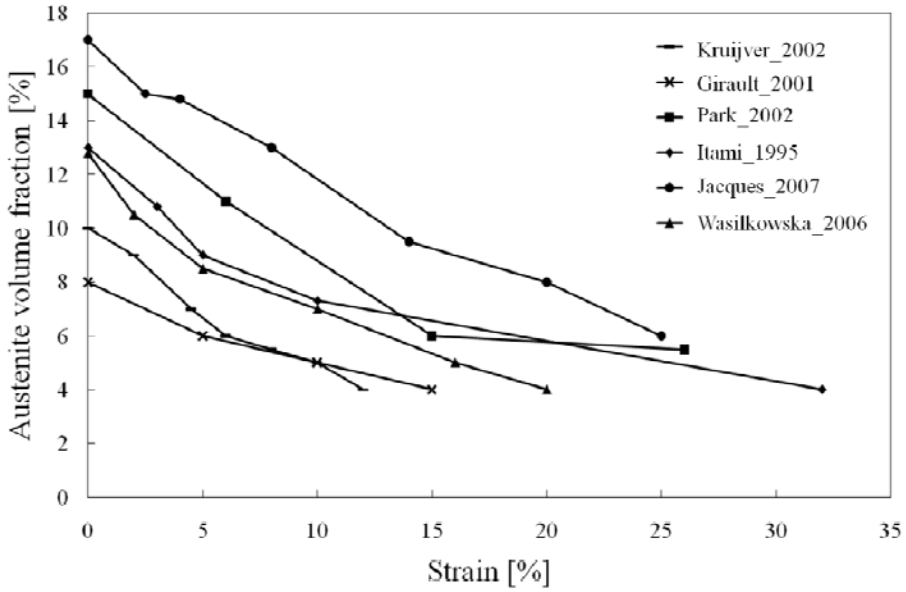

Fig. 2-15. The volume fraction of austenite in TRIP steel as a function of strain level [87][7][88][89][23][90].

It is observed that the initial austenite volume fraction differs significantly in the various studies, and ranges from 8 to 17 vol%. It follows that the rate of reduction of the austenite content (i.e. the slope) during straining is similar for all curves, even though the initial austenite fraction varies by a factor 2. Therefore, it can be concluded that the development of the austenite fraction upon deformation is strongly dependent on the initial value and it must be verified which factors are the most significant for the initial austenite fraction. In the literature, it is generally stated that three main factors are responsible for the initial austenite fraction are: composition, heat treatment and analysis technique; and the factors will be discussed below. Table 2-4 lists information on the TRIP steels investigated in the studies presented in Fig. 2-15.

Table 2-4. Information on the TRIP steels used in the studies from Fig. 2-15.

Ref.	C (wt%)	Main elements (wt%)	Annealing	Bainite holding	Analysis method
[87]	0.17	1.8Al-1.5Mn-0.3Si	900°C - 10 min	400°C - 2 min	XRD
[7]	0.11	1.5Al -1.6Mn-0.1Si	>750°C - 4 min	375-450°C	XRD
[88]	0.16	1.8Si-1.5Mn	-	-	EBSD
[89]	0.14	1.9Si-1.7Mn	830°C - 1 min	400°C - 8 min	XRD
[23]	0.29	1.4Si-1.4Mn	760°C - 6 min	410°C - 6 min	XRD, Mössbauer
[90]	0.20	1.5Si-1.5Mn	800°C - 1min	400°C	EBSD, Magnetometry

The effect of composition on the initial austenite volume fraction can be subdivided into the effect of carbon content and the effect of steel grade. TRIP steels can be subdivided in Si-Mn and Al-Mn-Si grades, where the latter has been developed to reduce the Si content in order to create better surface properties for galvanizing [17]. The difference in carbon content in the various steels listed in Table 2-4 is observed not to have significant influence on the initial austenite volume fraction but there seems to be a correlation between steel grade and austenite volume fraction. As seen from Fig. 2-15 and Table 2-4 there is a lower initial austenite volume fraction in the Al-Mn-Si steels as compared to the Si-Mn steels. Earlier, it was found that substituting Si by Al leads to an increase of the austenite volume fraction [17]. These conclusions from the literature are seemingly very contradictory, which indicates that the steel grade is not the major factor to control the initial austenite volume fraction.

The heat treatment procedures employed for the steels used in the studies appear to have a significant influence on the initial austenite volume fraction. Higher annealing temperatures and durations, and higher bainite holding temperatures and durations are associated with a lower amount of austenite in the initial condition. This is not surprising since more ferrite and bainitic ferrite will be formed by increasing the temperature and duration of the heat treatment, and consequently the austenite volume fraction will decrease.

Various analysis methods were applied to measure the austenite volume fraction in the various studies in Table 2-4 but no significant correlation was observed between the analysis technique and the austenite volume fraction. In the literature there have also be some attempts to find a systematic correlation between the analysis method and the volume fraction of austenite, and

additionally, also to find the best analysis method. The conclusion from literature is that the various analysis methods give different retained austenite volume fractions but no systematic difference appears to exist [81]. Not even between bulk and surface analysis methods a difference was identified, despite the fact that the preparation techniques used for surface analyses may affect the amount of retained austenite and hence, affect the result. Therefore, it can be concluded that the difference in initial austenite fraction of the studies in Fig. 2-15 does not arise from the use of different analysis methods, but it must be strongly related to the heat treatment procedure, as discussed above.

Furthermore and most importantly, the literature studies in Fig. 2-15 all show the same slope, which indicates that the austenite transformation rate is of comparable magnitude, irrespective of composition, heat treatment, and analysis technique.

Apart from the evolution of the volume fraction of austenite with the applied strain it is important to investigate general microstructural aspects of the steels in order to understand the austenite stability. The stability of retained austenite in TRIP steel during deformation has been widely investigated in the literature. Primarily such stability investigations were performed ex-situ, i.e. after loading and unloading in a device outside the instrument of investigation [15][90][91]. A few studies were devoted to investigating the stability of retained austenite in-situ with Electron Backscatter Diffraction (EBSD), however the results were inconclusive since they were obtained in a period where the technique was still under development [88].

2.3.3 Simultaneous effect of temperature and deformation

The combined effect of temperature and deformation on the microstructure of TRIP steel can be found in the field of thermomechanical processing of steels. Thermomechanical processing is used to produce fine grained steels in order to increase the strength without deteriorating the elongation and toughness and without the use of expensive alloying elements [1][92][93]. It is a field of extensive research to produce fine grained steels. The literature on thermomechanical processing of low alloyed steels can provide useful information on the combined effect of temperature and deformation on the microstructure in TRIP steels, as the one occurring during friction stir welding. Thermomechanical processing is performed in a temperature range where the initial microstructure in many cases is fully destroyed. Consequently, the comparability between TRIP steel and other low alloyed steels is good, despite the different phase composition in the initial microstructure.

Several transformations can occur during thermomechanical processing of low alloyed steels. In the following chapter it is the intention to present and describe some of the most frequently occurring transformations. Since FSSW is a combined effect of temperature and deformation, only dynamic processes are relevant. Therefore, the expected processes to occur are:

- Dynamic recovery of ferrite
- Continuous dynamic recrystallization of ferrite
- Strain-induced transformation of ferrite
- Dynamic recrystallization of austenite

Dynamic recovery (DRV) of ferrite

When a material is plastically deformed, dislocations are formed, which is associated with a higher internal energy in the microstructure. During dynamic recovery (DRV), dislocations will rearrange and annihilate into subgrain boundaries, thereby leading to lower energy configurations [94]. DRV is normally only associated with formation of low angle grain boundaries [94][95] but at pronounced recovery stage or local variations in dislocation density will enable migration of the subgrain boundaries and creating of high angle boundaries [92][96][97]. At higher strains and in the intercritical temperature range, DRV shifts to become continuous dynamic recrystallization of ferrite, which will be described below [95][98][99][94][100][101]. DRV can also take place at temperatures below Ac_1

The degree of recovery depends mainly on temperature and strain but also the strain rate is significant for the mechanism. At high strain rate the degree of recovery is lowered since there is less time available for dislocation annihilation and rearrangement in order to generate sub-grain boundaries [102]. DRV occurs faster in the vicinity of grain boundaries, and as a result the recovery becomes more pronounced in small grains [96].

Continuous dynamic recrystallization (CDRX) of ferrite

Recrystallization occurs in highly deformed microstructures by the nucleation and growth of new grains. The nucleation and growth can occur generally in two ways. It can occur by heterogeneously in the microstructure, where nucleation takes place on preferred nucleation sites such as precipitates and high angle grain boundaries. This process is accompanied by conventional nucleation and growth processes, and it is described as discontinuous [97]. Alternatively, the process can occur homogeneous throughout the microstructure with a gradual development of the microstructure during straining with no identifiable nucleation and growth stages, and this process is described as continuous. Accordingly, the formation of high-angle grain boundaries occurs by progressive rotation of subgrains [97]. When low carbon steels are deformed in the intercritical region, it is widely accepted that ferrite undergoes a continuous dynamic recrystallization (CDRX) [103][99][95][62][98][104][92][97]. In CDRX of ferrite, the subgrain boundaries developed by DRV will absorb the dislocations developed at higher strain with the result of gradually increasing misorientation angles, and thereby the formation of HAGBs. Therefore, by CDRX the nucleation and growth of new grains are not identifiable but the formation of new grains surrounded by HAGBs occur primarily by an extension of the DRV

process [95][99]. DRV and CDRX are generally considered as one same process; CDRX and no distinction between the two processes is possible. Only at low strains, where DRV occurs alone, the presence of only LAGBs indicates that only DRV takes place.

The CDRX is according to the literature only expected to occur in the intercritical region, whereas at high strain in the ferrite regime, it is the conventional DRX, which will take place; i.e. discontinuous DRX [95].

Strain-induced transformation (SIT) of ferrite

When ferrite is nucleated from austenite at a temperature in the austenite region during heavy deformation, formation of nucleation of ferrite can occur by the so-called strain-induced transformation (SIT) of ferrite [92][105][106][107]. Ferrite is nucleated intragranularly in the austenite grains, which results in a characteristic morphology of equiaxed grains aligned in rafts with a grain size of 1-3 μm [106][107][108][109][110][92][111][107]. The morphology depends on the strain level; at low strains the ferrite grains impinge on only the neighboring grain creating planar arrays whereas at higher strains the impingement is three-dimensional and the fine ferrite grains attain a more massive morphology and a larger volume fraction [111][112][113][106][107][108]. The morphology of SIT of ferrite as a function of strain and temperature is illustrated in Fig. 2-16.

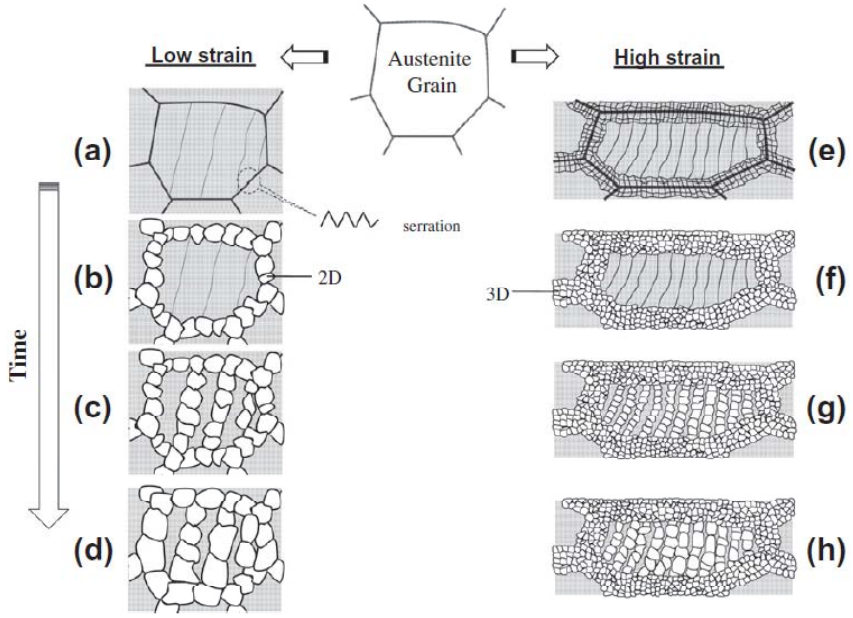

Fig. 2-16. Schematic illustration of SIT of ferrite [111]. 2D and 3D represent two- and three-dimensional impingements, respectively.

The temperature for strain-induced ferrite transformation is a field of some disagreement. Most commonly SIT is described to occur between Ar_3 and Ae_3 [92][111][107][106], but elsewhere it is indicated that SIT occurs just above Ae_3 [114]. If the cooling from higher temperatures to the transformation temperature is fast, fine ferrite grains can nucleate just below Ar_3 [106]. Nevertheless, the exact transformation temperature is not easy to predict because the equilibrium temperature becomes shifted when deformation is applied. Also the prior austenite grain size will affect the transformation temperatures [107].

The grain boundary character in ferrite formed by SIT varies and can contain both low angle and high angle boundaries but mostly HAGBs are developed [103][102][106][115][116]. Cooling rate, strain level and strain rate are parameters, which influence the grain boundary misorientation angles. When the microstructure is quenched immediately after deformation there is a high proportion of low misorientation angles. Following a 10 second isothermal hold, only few low angle boundaries remains [106]. When strain rate is high, there is a lower amount of low angle grain boundaries compared to a low strain rate [102].

Comparison of ferrite formed by CDRX and SIT

Ferrite grains developed from CDRX and SIT have particular characteristics, which were described in above, and these characteristics can be used for separation of the grains by morphological analysis. The characteristics of the two transformation types are summarized in Table 2-5.

Table 2-5. Overview of the characteristics of ferrite grains formed by SIT and CDRX.

Mechanism	SIT	CDRX
Temperature	Ar_3-Ae_3, or just above Ae_3.	Ferrite region and intercritical region.
Strain	High strain.	Low strain: only DRV; high strain CDRX.
Morphology	Equiaxed grains formed intragranularly in austenite. Low strain; arrays. High strain; more massive but still arrays. Band width refined at high strain. Mainly separated by HAGBs.	DRV contains mainly LAGBs within deformed ferrite grains. After CDRX both LAGSs and HAGBs appear and the morphology depends on the strain and temperature.
Size	1-3 µm.	Varying.

Another way to distinguish between the ferrite grains developed by the two processes is to consider the texture. The ferrite texture depends on the transformation and possible ferrite textures will be described in the end of this section since also recrystallization of austenite will be included in the review (Table 2-6).

Dynamic recrystallization of austenite

Dynamic recrystallization of austenite occurs by a similar mechanism as the conventional DRX of ferrite, as described in above. When deformed at high temperature, new grains are nucleated on high-angle grain boundaries pre-existing in the microstructure before deformation. The temperature range for the recrystallization of austenite is the austenitic region, above Ac_3 [104][117][105].

Upon cooling the recrystallized austenite will transform into ferrite or other phases, and the transformation occurs identical as for the unrecrystallized austenite except for the rate by which the transformation occurs. Unrecrystallized austenite will transform at a faster rate than recrystallized austenite which is caused by mainly two effects: First, unrecrystallized austenite has a higher energy state and is less stable, and second, the defects act as nucleation sites and thereby promote the nucleation upon cooling [102].

The microstructure formed from recrystallized austenite can be very fine grained ferrite and from this microstructure it is easily investigated if the prior austenite has been recrystallized [102][104][105]. If martensite or bainite is formed, it is not possible by immediate investigation to verify whether the austenite has been recrystallized before cooling or not, and the prior austenite grains must be used to verify the occurrence of recrystallization. The prior austenite grains can be determined by assuming special orientation relationships such as Kurdjumov-Sachs between the prior austenite grains and martensite [1]. Alternatively, the texture will delineate if recrystallization of prior austenite grains has occurred, and it will be described in the end of the section.

Texture of ferrite formed from various thermomechanical processes

The texture of the formed ferrite is dependent on the transformation mechanism, by ferrite has developed. The possible textures of ferrite are listed in Table 2-6.

Table 2-6. Literature summary of the various types of ferrite texture [118][119][120][121][122][116][115].

Origin of the ferrite grains	Texture
Ferrite exposed to shear (DRV)	D1: $\{11\bar{2}\}<111>$, D2: $\{\bar{1}\bar{1}2\}<111>$, E: $\{110\}<1\bar{1}1>$, -E: $\{\bar{1}\bar{1}0\}<\bar{1}1\bar{1}>$, J: $\{110\}<1\bar{1}2>$, -J: $\{\bar{1}\bar{1}0\}<\bar{1}12>$, F. $\{110\}<001>$
Recrystallized ferrite (DRX)	Random texture
Ferrite from un- recrystallized γ (SIT)	$\{113\}–\{112\}<110>$ *(from {112}<111> austenite texture)* $\{332\}<113>$ *(from {110}<112> austenite texture)*
Ferrite from recrystallized γ	$\{001\}<110>$ *(from {100}<001> austenite texture)*

3 Experimental Methods

3.1 TRIP steel

The investigated steel is TRIP690 supplied by ThyssenKrupp Steel AG. The chemical composition is specified in Table 3-1.

Table 3-1. Chemical composition of TRIP690 steel. All contents are maximum values.

Element	C	Al	Mn	S	Si	P	B	Cr+Mo	Nb+Ti	Fe
Wt.%	0.24	1.60	2.0	0.01	0.30	0.04	0.005	0.60	0.20	Bal.

The as-delivered condition of the steel is cold-rolled, with a thickness of 1.2 mm, giving a tensile strength og at least 690 MPa, at an elongation of 23%. The surface is covered with an electrodeposited 140-µm-thick Zn coating.

For the 1st generation welds the size of the sheets to be welded is 100 mm x 40 mm. For the 2nd generation welds, the sheets were 100 mm x 20 mm. Prior to welding the sheets were washed and degreased in ethanol.

3.2 Welding

Friction Stir Spot Welding (FSSW) was performed at the laboratory facilities of MegaStir Technologies in Provo, Utah, US. The welding facility is a rebuild Kearney & Trecker milling machine that allows a rotational speed from 15 to 1500 rpm.

The sheets were welded in a 30 mm overlap configuration (see Fig. 3-1 for the joint configuration).

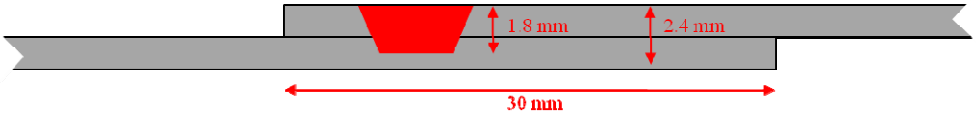

Fig. 3-1. Illustration of the joint configuration in the present study. The length of the tool pin is 1.8 mm, and the thickness of the two sheets is 2.4 mm.

Tool and tool holder were developed and manufactured by MegaStir Technologies in Provo, Utah, US. The tool is made of polycrystalline boron nitride (PCBN), with a simple geometry with three flat sides and no threads (Fig. 3-2 and Fig. 3-3).

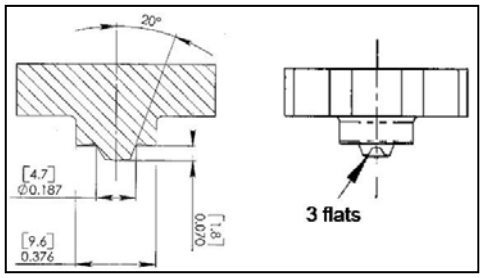

Fig. 3-2. Sketch of tool dimensions.

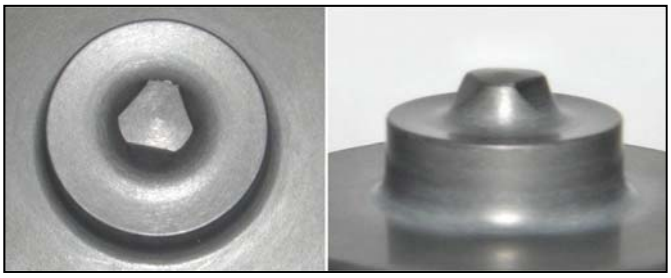

Fig. 3-3. Images of the PCBN tool.

The length of the tool is adjusted so that it penetrates half way through the lower sheet, which is recommendable for FSSW, which was illustrated in Fig. 3-1. The tool holder includes a water cooling system and an Argon inlet around the tool.

Welding was performed with variation of the following parameters:

- Rotational speed
- Dwell time

Three different rotational speeds were investigated; 500, 1000, and 1500 rpm, and the dwell time was varied from 0.5 to 4 seconds. The plunge-in velocity of the tool into the work piece was 0.04 mm/s for all welds. Welding was performed in two batches with the outcome of 1st and 2nd generation welds. Table 3-2 gives an overview of the welding parameters applied.

Table 3-2. Weld parameters in the two generations of welds.

1st generation			
Rotation speed	Dwell time	Plunge rate	Name
500 rpm	1 sec	0.04 mm/s	500-1
1000 rpm	1 sec	0.04 mm/s	1000-1
1500 rpm	0.5 sec	0.04 mm/s	1500-0.5
1500 rpm	1 sec	0.04 mm/s	1500-1
2nd generation			
Rotation speed	Dwell time	Plunge rate	Name
1000 rpm	1 sec	0.04 mm/s	1000-1-2nd
1000 rpm	2 sec	0.04 mm/s	1000-2-2nd
1500 rpm	1 sec	0.04 mm/s	1500-1-2nd
1500 rpm	2 sec	0.04 mm/s	1500-2-2nd
1500 rpm	4 sec	0.04 mm/s	1500-4-2nd

During welding the tool-workpiece interface and the surface of the upper sheet were observed to reach a red-orange color. This observed color indicates the temperature, which at least was reached during welding, because this part cools fastest; the peak temperature underneath the tool is likely to have been higher. For low alloyed steel the temperature corresponding to the color is shown in Fig. 3-4, from which it is concluded that the temperature was at least 900°C.

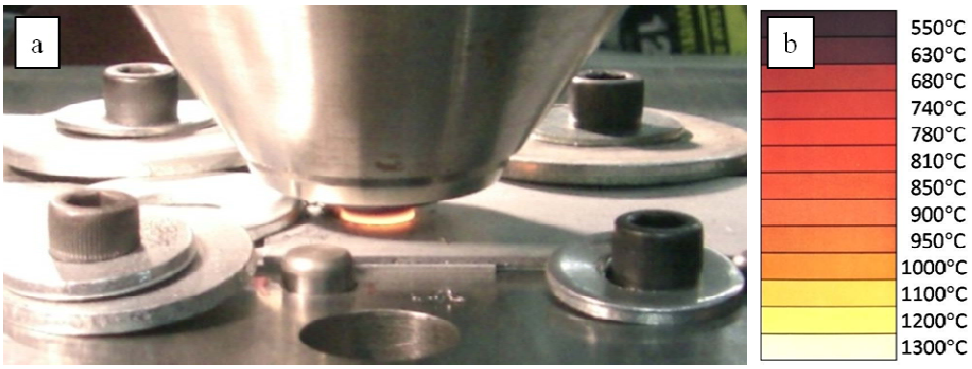

Fig. 3-4. Picture of the orange-red color obtained during welding in the present study (a) and a color scheme predicting the temperature of low alloyed steels based on the color (b) [123].

This is a very rough estimation, but the only indication of level of the temperature reached during welding, because thermocouples positioned at the surface will interfere with the rotating tool.

3.3 Metallography

3.3.1 Preparation for metallography

Sample preparation for metallographic and microstructure investigation was performed according to the procedures provided in Table 3-3.

Table 3-3. Overview of steps performed in sample preparation for metallography. RLM is reflected light microscopy; SEM, EBSD, TEM and XRD have their usual meaning.

Preparation step	RLM	SEM	EBSD	TEM	XRD	Hardness
Mounting	X	X			X	X
Grinding #220	X	X	X	X	X	X
Grinding #500	X	X	X	X	X	X
Grinding #1000	X	X	X	X	X	X
Grinding #4000	X	X		X	X	X
Polishing 3 µm	X	X			X	X
Polishing 1 µm	X	X			X	X
Polishing OP-S			X			
Electropolishing			X			
Etching	X	X			X	X
Carbon coating		X				
Ion milling				X		

Samples were vacuum mounted in epoxy. For polishing and grinding a Struers RotoForce-4® was applied. All accessories and consumables were supplied by Struers.

To avoid transformation of retained austenite into martensite upon deformation during mechanical grinding and polishing, special care must be taken. An approach to avoid transformation is to decrease the force applied during grinding and polishing, and concurrently increase the time for grinding and polishing. For these samples a force of 10 kN was used, and grinding and polishing were applied for durations of 5-10 minutes, depending on the outcome. For polishing with 3 µm diamond paste green lubricant was used; for polishing with 1 µm diamond paste blue lubricant was used.

Electropolishing was performed on two different setups: A Struers Polectrol® electropolishing instrument and a self-built setup consisting of aluminum foil as cathode and the sample as anode, both submerged in the electrolyte and connected to a power source. Struers A-2 was used as electrolyte in both setups, and it is important to use fresh electrolyte for each sample. The voltage was applied in the range of 12-16 V for 15-40 seconds. The temperature during electropolishing was varied between 5 and 25 °C. The optimum conditions for electropolishing were obtained at 10°C for a voltage of 12 V and polishing for 30 seconds.

Samples for XRD should preferably not be etched but it was difficult position the beam correctly without having the appearance of the welded zones. It is assumed that etching will not have an

influence on the results because the diffracted volume is so large that the affected surface will not contribute significantly to the diffraction.

The microscope used for ion milling was a dual-beam Quanta 200 3D microscope with a tungsten filament, employing Ga ions for milling. The samples prepared by ion milling contained a fully martensitic microstructure already before ion milling. If applied to TRIP steel BM, austenite will transform during ion milling [124].

The samples for investigation with SEM were etched in Nital 2% for 2-3 seconds. For RLM, various etchant are possible.

For RLM a number of relevant etchants are listed in Table 3-4. Not all etchants were applied, but it will be discussed in Chapter 4 - TRIP steel base material.

Table 3-4. Recipes of the relevant etchants for RLM investigation of multiphase low alloyed steels.

Method	Recipe	Outcome from etching	Ref.
Modified LePera	Part 1: 4% picral, 2-3 drops HCl. Part 2: 10% SMB. 15-20 sec in Part 1 and 5-8 sec in Part 2.	Ferrite: beige, Bainite: bluish brown, Austenite: white, Martensite: straw colored	[125][126]
SMB*	10 % SMB. Etch for 15-20 sec. under stirring.	Ferrite: untouched, Austenite: clear, Martensite: brown/dark, Bainite: unknown.	[126]
Nital	2-3 sec in Nital 2%.	Grain boundaries appear, and distinction of martensite and ferrite is achieved. Also prior-austenite grain boundaries appear.	[125][127]
Nital + SMB*	See [128]	Ferrite: off-white, bainite + martensite: dark, austenite: white	[126][128]
LePera	Part 1: 4% picral, Part 2: 1% SMB. Part 1 and 2 is mixed 1:1, etch for 6-8 sec.	Ferrite: yellow/blue, bainite: brown, austenite + martensite: white.	[4][126][129]
LePera + Nital	LePera (see above), followed by 2-3 sec in 2% Nital.	Martensite: blue-violet, bainite: blue green, ferrite: light brown, austenite: white.	[130]
Vilella's	See [127][128]	Characterization of ferrite-carbide structures. Also determination of prior-austenite grain size.	[127][128]
Marshall's	See [125]	Grain boundaries appear.	[125][127]
Beraha	See [131]	Bainite: brown, martensite: blue	[131]

*Sodium metabisulphate (SMB)

Sodium meta-bisulphate (SMB) is an aqueous solution, and the solution must be freshly prepared before use. It is important to stir thoroughly during etching with SMB. To ensure enough stirring during etching the whole sample was immersed into the SMB solution and the sample was moved while the solution was stirred.

3.3.2 Reflective light microscopy

Reflective light microscopy (RLM) was performed on a Neophot 30 with achromatic lenses. The microscope was equipped with a Leica DFC 425C digital camera. For magnifications of more than 800 x, oil-immersion objectives were applied.

3.3.3 Scanning electron microscopy

Scanning electron microscopy (SEM) was performed with a JEOL JSM-5900 equipped with a LaB_6 filament applying secondary electron imaging (SEI) and backscattered electron imaging (BEI) as well as energy dispersive spectroscopy (EDS, Oxford Instruments) for quantitative chemical analysis. The acceleration voltage during imaging was 10-15 kV with a spot size of 30-40. During EDS measurements, the acceleration voltage was increased to 20 kV to include all important elements in the analysis.

3.3.4 Electron backscatter diffraction

Microscope setup

Electron backscatter diffraction (EBSD) was performed using a Helios EBS3 Nanolab dual-beam scanning electron microscope with FEG filament, with an EDAX/TSL EBSD system. Some EBSD measurements (mainly Sample 1500-1) were performed using a JEOL JSM7000F with a field emission gun equipped with an EBSD system from TexSEM Laboratories (TSL).

The acceleration voltage during EBSD data collection was 12-15 kV, beam current 2.5-5.5 nA, the working distance 8 mm (15 mm for JEOL JSM7000F) and the step size 20-60 nm. The size of the measured EBSD maps varied but the maps obtained in Sample 1500-1 were systematically kept constant at 25 x 40 µm. The maps were measured along a line in the same location as XRD (Fig. 3-8) and hardness measurements (Fig. 3-9), but on a separate sample prepared for EBSD investigation.

TSL OIM software functions

The TSL OIM software contains several automated functions for characterization of EBSD maps. Some of the most used functions in the present study are shortly described here.

The image quality (IQ) describes the quality of an electron backscatter diffraction pattern. The IQ is affected by imperfections in the crystal lattice, such as grain boundaries, high dislocation density, precipitates and lattice strain. Also the surface conditions, as surface roughness and surface contamination, have an influence on the IQ. Therefore, it is important to consider the possibility of preparation artifacts on analyzing the IQ of an EBSD map.

The confidence index (CI) is a parameter that indicates the reliability of the indexed diffraction pattern. For a given diffraction pattern several possible solutions may satisfy the diffraction bands detected by the image analysis routines. The software ranks the solutions using a voting scheme. The confidence index is based on the voting scheme and is given as $CI = (V_1 - V_2)/V_{IDEAL}$, where V_1 and V_2 are the number of votes for the first and second solutions and V_{IDEAL} is the total possible number of votes from the detected bands. The confidence index ranges from 0 to 1. A diffraction that could not be indexed is assigned CI = -1.

Grain Average IQ (GAIQ) calculates the average IQ of the entire grain. Each point is shaded according to the average image quality for the grain to which it belongs.

The *Grain Shape Aspect Ratio (GSAR)* is a measure of the elongation of a grain. The method assigns a shade to a point in accordance with the aspect ratio of the grain to which the point belongs. The aspect ratio is defined as the ratio of the minor axis to the major axis of the ellipse that (approximately) fits the grain.

Kernel Average Misorientation (KAM) is the misorientation between a point in the center of a pre-determined kernel, and the points in the perimeter of the kernel. The misorientation value is the average of all misorientations. Alternatively, KAM can be calculated between the center point and all points in the kernel.

Grain Average Misorientation (GAM) calculates the misorientation between neighboring points in a grain. The average misorientation is determined for a grain, and assigned to each point within the grain.

Legends

When EBSD maps are presented in figures, legends are used to describe the contents of the EBSD; examples are given in Fig. 3-5.

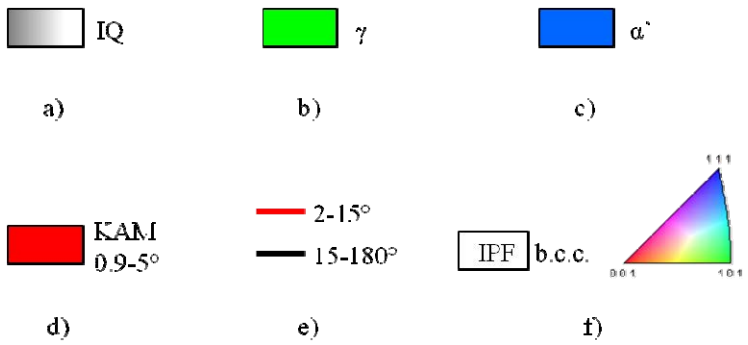

Fig. 3-5. Examples of legends used for presentation of EBSD maps.

IQ (a) maps are always generated in grayscale in the present study. Black is lowest IQ value, and white is highest. Phases are identified automatically by the software, and the f.c.c. phase is always represented in green (b), and interpreted as γ. Martensite, α', is mainly represented in blue (c) and the identification method will be described in the text. Mostly GAIQ will be used to identify α'. KAM (d) is used in the present study for the investigation of various phenomena in the microstructure. The angular range colored is always given, such as it is illustrated in Fig. 3-5. If nothing else is stated, a kernel of 200 nm is used, and always only with reference to the perimeter of the kernel. These parameters were found by analyzing TRIP steel base material, as given in Fig. 4-10. Grain boundaries (e) are represented as lines with different colors, and the misorientation range of the lines will be illustrated in the legend for each figure. When Inverse pole figure (IPF) coloring (f) is applied, only a box with the text "IFP" (similar as in Fig. 3-5 f) is given in the legend. The colored triangle, which represents the colors of IPF coloring will not be included in the figures, since all identified phases in the present study are cubic, and therefore refers to the same color coding.

Identifications of other phases or phenomena in the microstructures will be color coded individually and described in detail in the legend of the figure in concern.

Cleaning of EBSD datasets

Incorrect or failed identification of EBSD data points cannot be avoided and a clean-up procedure is applied to reduce and remove these points. The EBSD datasets are cleaned by a sequence of several steps, which will be described in the following.

In the first step, the CI value in all grains is increased to fit the highest CI in that grain (CI Standardization). A grain is defined as having a minimum grain size of 120 nm, surrounded by misorientation angles of more than 2°. The second cleanup procedure is called Grain Dilation. The Grain Dilation method changes the points that do not belong to a grain, either because they are excluded as a consequence of the grain definition (minimum 120 nm and 2° misorientation angle) or because their CI is below 0.1. Several parameters can be changed after the Grain Dilation cleanup such as the phase, IQ, orientation and CI, and it is changed to fit the most

dominating neighbor (i.e. with most neighboring points) or the neighbor with highest CI. Grain Dilation is an iterative process, which was only applied once in the datasets. Points that remain un-indexed or uncleaned, are finally removed by selecting only grains with CI larger than 0.1. This last step is mainly applied for quantitative analysis, whereas for morphological analysis the low CI grains are (mostly) included.

A misorientation angle of 2° is selected as a criterion, because subgrains are present in the microstructure. For the chosen threshold value, subgrains are considered a grain in the cleaning steps. On applying the Grain Dilation method, the orientation of the subgrains is changed to fit a neighbor with higher CI, whenever the subgrain size is below the defined size of a grain.

The minimum grain size of 120 nm was selected after a thorough analysis of several EBSD maps. In the present study, various types of microstructures were investigated, including base material, welded samples, heat treated samples, and samples after tensile testing. A universal minimum value applicable for all samples is needed. The size of the austenite grains is the most critical parameter for the cleaning procedure. The smallest austenite grains were observed in the base material and in the thermomechanically affected zone of welds (Fig. 3-6 and Fig. 3-7). Therefore, these microstructures were used to assess the threshold value for the minimum grain size in the cleaning procedure. Fig. 3-6 shows the effect of the threshold value on the result after cleaning.

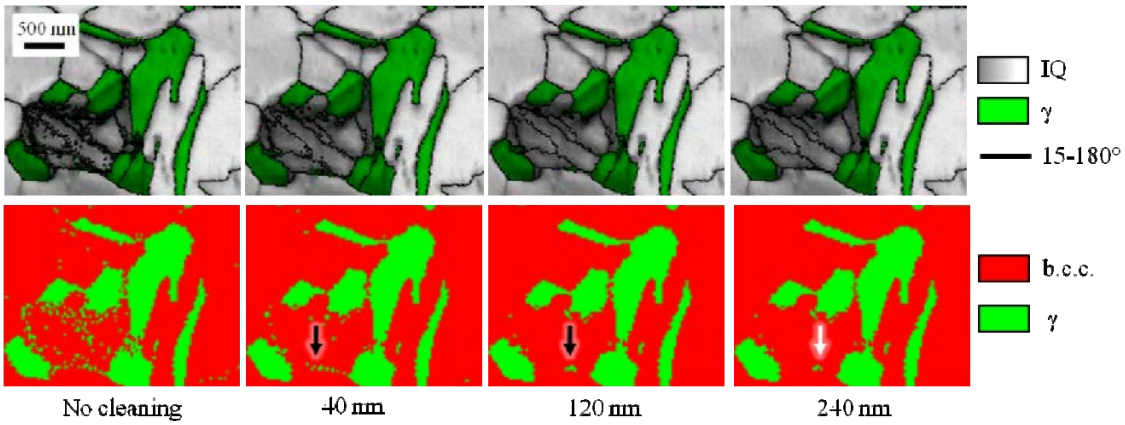

Fig. 3-6. Cleaning of EBSD map from base material, with different threshold values for defining the minimum grain size (given in the figure). Top row: IQ maps including f.c.c. phase; bottom row: phase map.

Before cleaning many scattered f.c.c. points are observed, which are not removed for a 40 nm threshold. This can be seen in the phase map (bottom row of Fig. 3-6), but it can also be seen from the IQ maps (top row of Fig. 3-6). The scattered points observed at grain boundaries arise because diffraction occurs from both neighboring grains and it complicates the identification and more wrongly identified points will appear near grain boundaries. It is observed that for a

threshold of 120 nm, the scattered f.c.c. points appear to be reduced properly (black arrows). For a threshold of 240 nm the small f.c.c. grain (white arrow) are reduced further in size, which is most likely not correct, and it is an indication that a threshold value of 240 nm may cause unwanted removal of austenite grains. The conclusion is that a threshold value of 120 nm is a suitable value for the minimum grain size on cleaning the base material EBSD datasets.

Fig. 3-7 shown a similar analysis as above, in order to find a suitable threshold value for the minimum grain size in the thermo-mechanically affected zone (TMAZ).

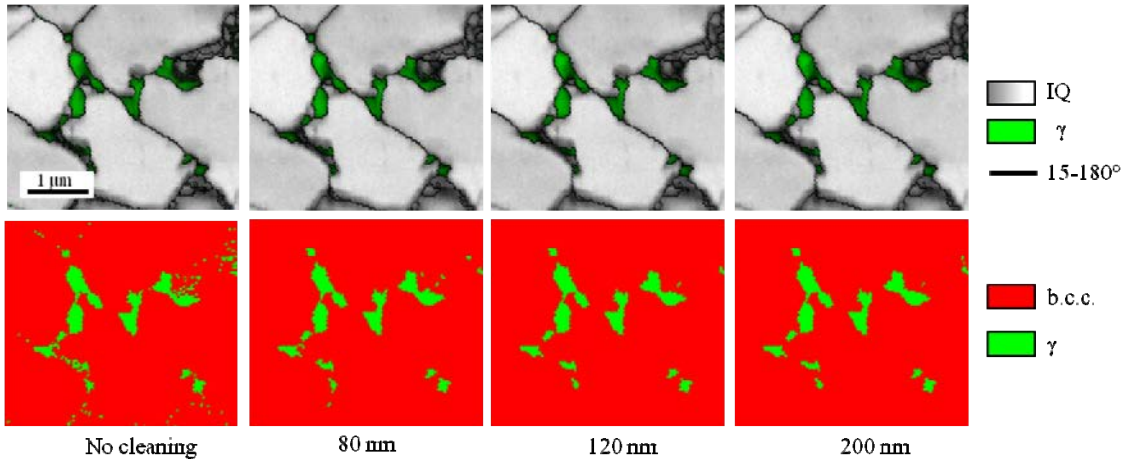

Fig. 3-7. Cleaning of EBSD map from TMAZ, with different threshold values for defining the minimum grain size. Top row: IQ maps including f.c.c. phase; bottom row: phase map.

The austenite grains in the figure are among the smallest grains observed in this study. As seen from the cleanup levels, none of the selected values causes complete removal of these grains. The threshold value of 120 nm is observed to remove many of the scattered points, but still without removing the important grains. No significant difference was observed after increasing the threshold value from 120 nm to 200 nm, wherefore a threshold value of 120 nm was chosen. This agrees with the findings for the threshold value for the base material (Fig. 3-6).

Construction of combined color EBSD maps

The TSL OIM software cannot color the microstructure with several methods simultaneously, because only one color coding can be used at the same time. By creating a partition, two color codes can be used simultaneously, but not more than two. Color codes cannot be confined to only one phase, when it is desired to display the entire map at the same time. Therefore, in the present study, a technique was developed to superimpose several maps on top of each other. This was done with simple image editing software, such as Adobe Photoshop, Paint Shop Pro and

Microsoft Powerpoint. The color coded maps were constructed and only contained the color coding, so that the remaining part of the map can be removed. Several color coded maps can be constructed and combined by superimposing them onto each other by the image editing software.

3.3.5 Transmission electron microscopy

Transmission electron microscopy was performed with a JEOL 3000F TEM with a field emission gun. The electron voltage was 300 kV. For electron diffraction the camera length was 800 mm, as calibrated on a [200] oriented Au standard to 74810 pixels. Selected area diffraction (SAD) and convergent beam electron diffraction (CBED) were employed. SAD produces well defined diffraction spots, but the electron beam interacts with a relatively large volume of the sample. For this reason SAD is primarily used for dark field imaging. In CBED diffraction the interaction volume is small and well-defined and discs appear in the diffraction pattern. The technique is useful for microdiffraction and for phase identification.

3.3.6 X-ray diffraction

X-ray diffraction (XRD) line profile analysis was performed on Bruker AXS D8 Discover equipped with Cr-K_α radiation (wavelength 2.28962 Å). XRD investigations were done with µ-XRD collimators to obtain a narrow X-ray beam for a local measurement. The XRD setup is equipped with a CCD camera to enable precise adjustment of height and position of the X-ray beam. The size of the µ-XRD collimator was chosen separately for each measurement.
Sample 1500-1 was investigated in several regions affected by welding. A cross sectional view of the sample with indication of the locations, where µ-XRD was carried out, is given in Fig. 3-8.

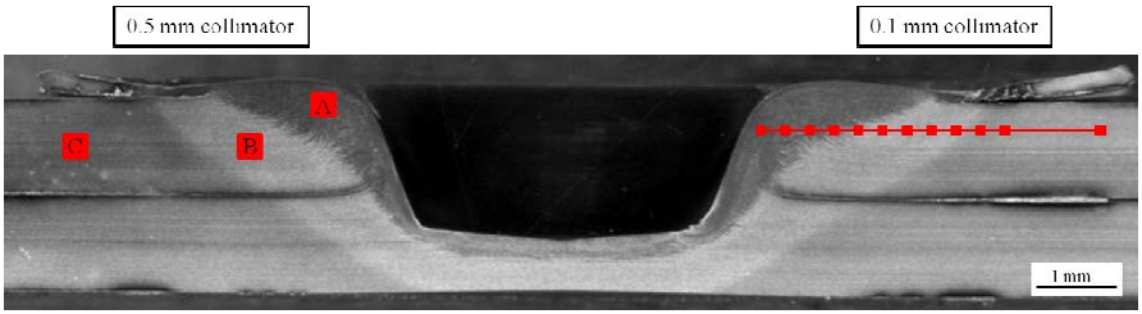

Fig. 3-8. Cross sectional view of Sample 1500-1 with indication of location for µ-XRD. The size of the µ-XRD collimators is indicated above the image.

The size of the collimator gives the width of the collimator opening and is comparable to the actual size of the beam projected on the sample since the beam is parallel. To enable correct positioning of the X-ray beam, etching of the microstructure was necessary, which was also mentioned above. Slit systems, step size, scan range, counting time and size of the µ-XRD collimator are given Table 3-5.

Table 3-5. Instrumental arrangement during the three XRD measurements.

Collimator	Points	Scan range	Step size	Counting time	Slit system
0.5 mm	3	58-87°, 99-134.9°	0.03	65 sec/step	0.6/soller/0.6
0.1 mm	12	65.5-71.6°	0.05	75 sec/step	1 mm/soller/1 mm

A b.c.c. iron standard were prepared from b.c.c. powder (<10 µm particle size), which is dissolved in ethanol and placed on carbon tape. This standard was measured for each of the µ-XRD measurements in order to be able to correct for defocusing and other X-ray related artifacts. After evaporation of the ethanol, a fine layer of the adhering powder remained on the carbon tape.

The EVA program was used for determination of phases using the JCPDS database. The following JCPDS card numbers are applied for identification of the phases: γ – 31-0619, α – 06-0696, α' – 44-1291. Topas was used for fitting of the peaks and determine peak position and line broadening.

Calculation of volume fraction of ferrite and austenite

The volume fraction of austenite in a low alloy steel can be calculated from the XRD pattern, after specifications described in the ASTM standard E 975 – 03. The standard assumes near random crystallographic orientation of ferrite and austenite phases, and the volume fraction of austenite should be above 1% [132].

The calculation can be based on one austenite peak and one ferrite peak, but preferably more peaks are included in the analysis to take the possible influence of preferred orientations into account. The volume fraction of austenite is calculated from the following formula:

$$V_\gamma = \frac{\sum_i \left(\frac{I_\gamma}{R_\gamma}\right)_i}{\sum_j \left(\frac{I_\alpha}{R_\alpha}\right)_j + \sum_i \left(\frac{I_\gamma}{R_\gamma}\right)_i} \qquad \text{Eq. (1)}$$

where summation is taken over all austenite peaks i and all ferrite peaks j. The parameter, R, depends on the interplanar spacing (*hkl*), Bragg angle (θ), crystal structure, and the composition of the phase under consideration. R-values are calculated for measurements using Cr K_α radiation and are given in Table 3-6.

Table 3-6. Calculated values of R-parameter after ASTM 975-03 [132].

Ferrite *hkl*	R	Austenite *hkl*	R
110	101.5	111	75.24
200	20.73	200	34.78
211	190.8	220	47.88

Calculation of carbon content in austenite

The carbon content of unstrained austenite can be calculated from XRD patterns after the following equation [89][7]:

$$a\ (\text{Å}) = 3.578 + 0.033\ C_\gamma\ (wt\%) \qquad \text{Eq. (2)}$$

where a is the lattice parameter of austenite, and C_γ the carbon content in wt%.

The carbon content in the remaining ferrite phase can be calculated very simply from the volume fractions of the phases. However, it is only valid for a pure austenite-ferrite microstructure, where no martensite or other phases are present. The carbon content of ferrite is:

$$C_\alpha\ (wt\%) = \frac{1 - (V_\gamma \cdot C_\gamma)}{V_\alpha} \qquad \text{Eq. (3)}$$

where C_α is the carbon content in ferrite.

3.3.7 Hardness measurements

Microhardness measurements were performed with a Future-Tech FM 700 microhardness tester equipeed with a Vickers indenter, applying a load of 100 g. Hardness was measured along lines parallel to the sheet surface, at a distance of 200-300 µm from the surface of the upper sheet (Fig. 3-9).

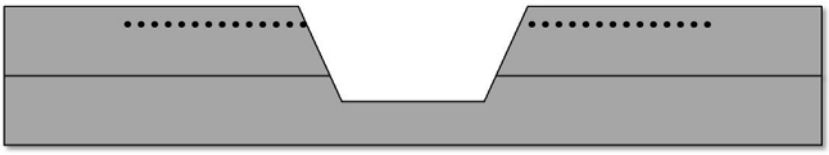

Fig. 3-9. Schematic representation of the weld with dashed lines illustrating the location of the hardness profiles.

To enable direct comparison of the microstructure characterization and the location in the weld, hardness indentations were also made after etching, as a tool for navigation. These hardness indentations served only for comparing between hardness and microstructure; the values themselves are not important. Samples for EBSD analysis were more complicated to mark with hardness indentations, because during electropolishing the edge of the pin hole rounds off and is therefore difficult to identify. As a consequence, the distance of the indentations to the pin hole was difficult to measure.

When hardness measurements are performed on areas in the microstructure, the value is averaged over 5 measurements.

3.4 Mechanical testing

3.4.1 Lap shear tensile test

Lap shear tensile tests were applied to determine the shear tension strength of the welds. The geometry of the tensile specimens are shown in the illustration in Fig. 3-10.

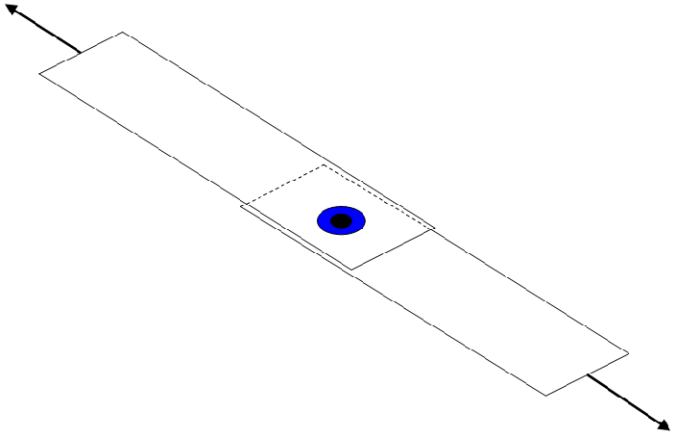

Fig. 3-10. Geometry of the lap shear tensile specimens. Thanks to Nils Elmegaard-Fessel for providing the illustration.

Lap-shear testing of the 1st generation welds was performed on a servo-hydraulic MST 810 tensile testing machine with a 100 kN load cell. For the 2nd generation welds the tensile tests were performed on an Instron 5500R with a load capacity of 100kN. During tensile testing on the Instron, the strain was measured using an extensometer. No slippage was observed during testing.

Since plastic deformation in the steel is strain-rate sensitive, the strain rate was the same for all tensile tests within a generation of welds. Therefore, samples are directly comparable within a generation, but not across.

The strength of the weld in steel sheets for the automotive industry has to meet the requirements specified by The American Welding Society [36], which is dependent on the sheet thickness and the type of mechanical testing.

3.4.2 In-situ tensile test

Samples for the in-situ tensile test were cut with a Cu arc wire. The geometry and dimensions of the tensile testing specimens for in-situ investigation are given in Fig. 3-11.

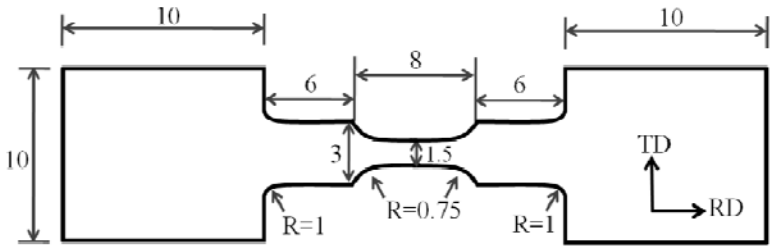

Fig. 3-11. Geometry of the tensile specimens used for in situ tensile testing. All lengths are given in mm.

The tensile tests were performed on a specially designed tensile stage (Ernest F. Fullam, Inc.) that allows in-situ EBSD investigation in a scanning electron microscope. Four EBSD measurements were performed, one at zero strain, one at elastic strain level (close to the yield point), and two measurements at the plastic strain levels ε=2.6 and 7.9. The EBSD measurements were performed after unloading, and the maps were measured on the same area of the sample after straining at the four strain levels. The observation plane of the sample was normal direction (ND) and the tensile direction was parallel to the rolling direction in the microstructure, as indicated in Fig. 3-11. The scanning electron microscope used was a JEOL JSM7000F, with a field emission gun, equipped with an EBSD system from TexSEM Laboratories (TSL). EBSD maps were measured within an area of 15 x 30 µm at a step size of 60 nm. The distance from the electron beam to the sample was 20 mm, which was slightly larger than the optimum working distance (15 mm), due to restrictions caused by the tensile stage.

Tensile specimens were mechanically polished and additionally electropolished, with a similar procedure as for conventional EBSD analysis.

3.5 Heat treatments

Simulated welding cycles were applied to TRIP690 sheets in a Gleeble 1500 thermal-mechanical simulator.

The thermal cycles involved heating to four temperatures: 500, 700, 780, and 850°C, which for the present steel are below Ac_1 (500/700°C) or within the intercritical region between Ac_1 and Ac_3. (780/850°C). The time for the heat treatments was 5 and 10 seconds, which corresponds to

the time necessary for heating to the chosen temperature. Thus, the heating rate was different for the 5 and 10 seconds heat treatment. As an example, for the 5 seconds heat treatment at 500°C, the heating rate is 100°C/s. The specimens were cooled with air cooling. All parameters are collected in Table 3-7

Table 3-7. Overview of heat treatments.

Name	Temperature	Heating time
HT-500-5	500°C	5 sec
HT-500-10	500°C	10 sec
HT-700-5	700°C	5 sec
HT-700-10	700°C	10 sec
HT-780-5	780°C	5 sec
HT-780-10	780°C	10 sec
HT-850-5	850°C	5 sec
HT-850-10	850°C	10 sec

The dimensions of the specimens used for the heat treatments were 100 mm x 20 mm with the original sheet thickness of 1.2 mm. The Zn layer was not removed before heat treatment, because it is expected to evaporate at the high temperatures, without influencing the experiments.

3.6 Dilatometry

Transformation temperatures of the present steel are determined by dilatometry experiments. Samples for dilatometry are produced from the 1.2 mm TRIP690 sheets. The sheets were ground to a sheet thickness of approximately 0.5 mm and bend to a pipe of Ø5 mm with a length of 20 mm. Dilatometry experiments were performed on a Netzsch DIL 402 CD dilatometer. The heating cycle was performed in the range: 25°C to 1100°C, in a reducing 9% H_2-Ar atmosphere. Three heating and cooling rates were applied: 1°C/min, 5°C/min, and 20°C/min.

Stresses are expected to arise under preparation of the pipe. Therefore, all dilatometry experiments were conducted twice on the same sample, and the second experiment will represent a stress-released sample.

4 TRIP steel base material

4.1 Determination of transformation temperatures

4.1.1 Calculation of transition temperatures

The transition temperatures were calculated with empirical relations based on the composition of the steel. The collection of equations provided in [1] can be used to calculate the two transformation temperatures; Ac_1 and Ac_3, from the contents of alloying elements. Each formula applies for a particular steel type, and includes only the most important alloying elements in the experimental study, wherein the formula was epirically derived. The steel types and included elements for the various equations are collected in Table 4-1. Furthermore, the calculated transformation temperatures for the steel used in the present study are listed in the table.

Table 4-1. The steel types and elements included in formulas [1], which are used to calculate Ac_1 and Ac_3.

Type of steel	Elements included	Ac_1 [°C]	Ac_3 [°C]
0.08-1.4 % C steel	Mn, Si, Cr	723	907
0.3-0.6% C low-alloy steel	Mn, Si, Cr	723	853
0.25-0.45% C low-alloy steel	C, Mn, Si, Cr, Mo	755	929
0.1-0.55% C low-alloy steel	C, Mn, Si, Cr, Mo	751	880
0.07-0.22% C low-alloy steel [133]	C, Al, Mn, Si, Cr, Mo, Nb	748	939

For the present steel type, the elements are all specified by the manufacturer as a maximum amount (Table 3-1). Therefore, the actual contents may be smaller than used in the equations. The contents of alloying elements can be determined experimentally but this was not done in the present study. Therefore, deviations from the calculated temperatures may occur. The wt% of Cr and Mo are given as a combined amount of 0.3 wt%. In the calculations, the elements were included as 0.15 wt% each. The same was done for Nb and Ti, which are also specified as a combined amount.

The only equation, which includes the influence of Al on the transition temperature, is the 0.07-0.22% C low-alloyed steel. The steel used in the present study contains 2.0 wt% therefore this equation is considered to give the most reliable prediction. As a result, the predicted transformation temperatures for TRIP690 are:

Ac_1 = 748°C

Ac_3 = 939°C

The equilibrium temperatures, Ae_1 and Ae_3 were estimated with Thermocalc (TCFE6.1 steel database) from the composition of the present steel, as:

Ae_1 = 720.4°C

Ae_3 = 998.2°C

Generally, it would be expected that the Ac_1 and Ac_3 temperatures are higher than the Ae_1 and Ae_3 temperatures, respectively. This appears only to be fulfilled for Ac_1 as compared to Ae_1.

4.1.2 Dilatometry

The dilatometry experiments were carried out twice for each heating/cooling rate, to investigate the effect of residual stresses, which develop during preparation of the samples. As both runs yielded similar curves it was concluded that the residual stresses have a marginal effect on the transformation temperatures.. Therefore, only the curves from the first runs are presented in Fig. 4-1.

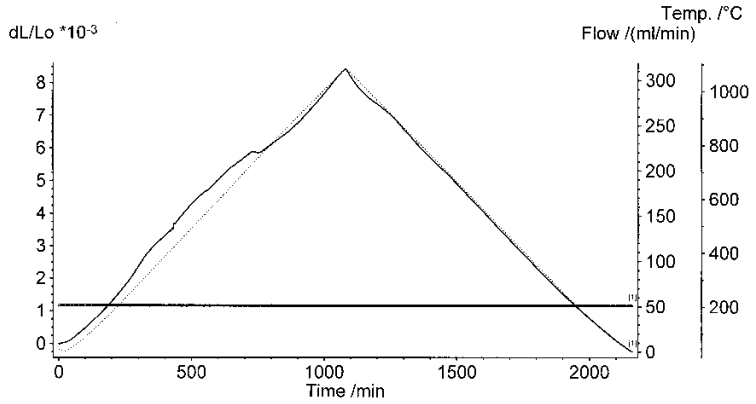

a)

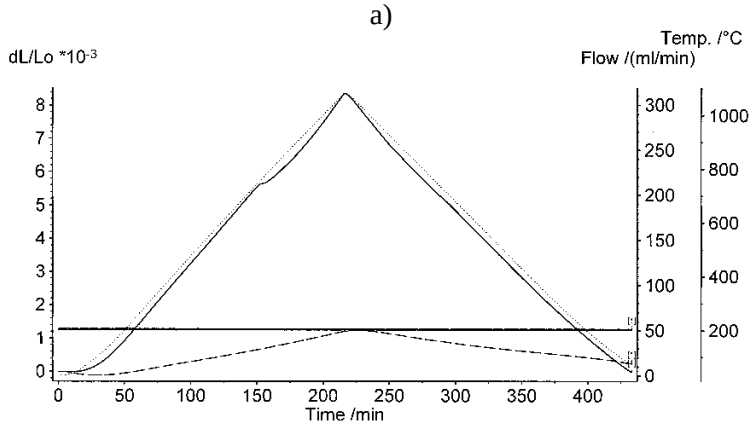

b)

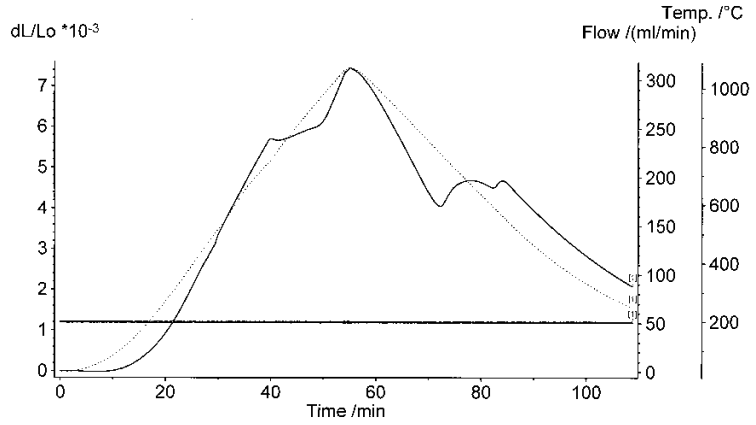

c)

Fig. 4-1. Dilatometry curves obtained at three different heating and cooling rates;
a) 1°C/min, b) 5°C/min, 20°C/min. Only the 20°C/min curve is useful.

No significant deflections are observed in the curves obtained with a heating and cooling rate of 1°C/min and 5°C/min. Hence, the curves are not useful for determination of the transformation temperatures. The curve based on heating/cooling rate of 20°C/min is useful, and the following transformation temperatures were found:

Ac_1 = 760°C

Ac_3 = 980°C

Ar_1 = 560°C.

Ar_3 could not be determined.

A fair agreement between the calculated and the experimentally determined transformation temperatures, Ac_1 and Ac_3, is observed. Therefore, the experimentally determined temperatures are used in the present work.

4.2 Directions in the TRIP steel microstructure

As TRIP steel is produced as rolled sheet, the appearance of the microstructure depends on the rolling direction. The reference system used for rolled products contains the three directions of the microstructure in the sheet; the rolling direction (RD), the transverse direction (TD) and the normal direction (ND). The TRIP steel used in the present study was characterized from all three directions; Fig. 4-2 shows SEM micrographs and EBSD maps of the three views.

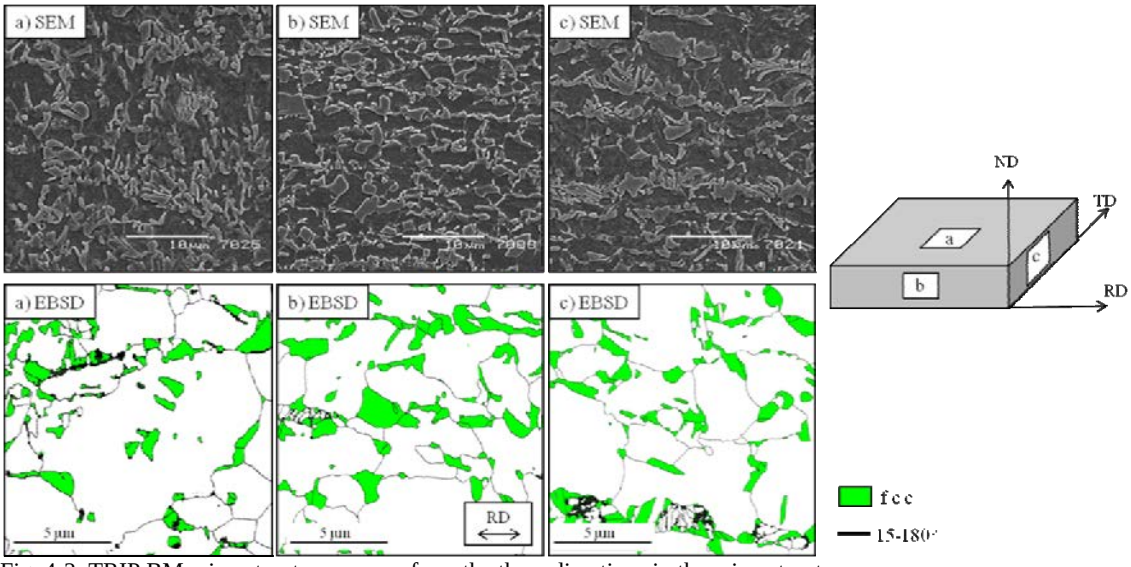

Fig. 4-2. TRIP BM microstructure as seen from the three directions in the microstructure.

Although the same micro-constituents are identified in all three views, their appearance in the microstructure is very different. An obvious directionality is observed in b) and c) in contrast with a). The direction in b), where RD is aligned horizontally, is the direction, from which all the

base material characterizations in the present study are performed. Also the characterizations of the welded samples in the following chapters are performed from the direction, where RD is horizontally aligned.

4.3 Characterization of the micro-constituents in TRIP steel

4.3.1 RLM

In Experimental Methods (Table 3-4) a list of the etching methods was given, which are considered useful for RLM characterization of low alloyed steels with multiphase microstructures. The suitability of the etching methods for the TRIP steel used in the present study is evaluated in the following. TRIP steel contains ferrite, austenite, bainite and martensite, and some of the methods are not able to distinguish between all four micro-constituents. Therefore, Vilella's, Marshall's and Beraha etching methods can be excluded. The remaining etching methods are applied for the characterization of the base material (BM) of TRIP steel. An overview of all etching methods mentioned in Table X is seen in Table 4-2, with comments on the suitability for the present study.

Table 4-2. Overview of the etching methods useful for multiphase low alloyed steels. The recipes and expected outcome of each technique are given in Experimental Methods. References are included there.

Method	Comments	Successful
Modified LePera	Tried and shown in the following	Yes
SMB	Tried and shown in the following	No
Nital	Tried and shown in the following	No
Nital + SMB	Tried and commented in the following	No
LePera	Tried and commented in the following	No
LePera + Nital	Tried and commented in the following	No
Vilella's	Considered useless for TRIP steel	N/A
Marshall's	Considered useless for TRIP steel	N/A
Beraha	Considered useless for TRIP steel	N/A

N/A: Not analyzed

As described above, three methods were considered unsuitable for TRIP steel before applying them in practice. The remaining methods were applied on the microstructure of TRIP steel in the present study, and their capability of separating all four micro-constituents was investigated.

Three methods were applied without success; these results are not presented here but just commented. Firstly, the double etching technique with LePera followed by Nital was not sufficient to distinguish between all four micro-constituents, because the microstructure appeared only etched by Nital and not by the combination of both techniques. Secondly, etching

with LePera did not allow austenite to be distinguished from martensite, because both appeared white in the microscope image. Finally, neither the double etching technique with Nital followed by SMB was successful, because bainite and martensite could not be distinguished.

RLM micrographs of TRIP steel microstructure etched with SMB and Nital are given in Fig. 4-3.

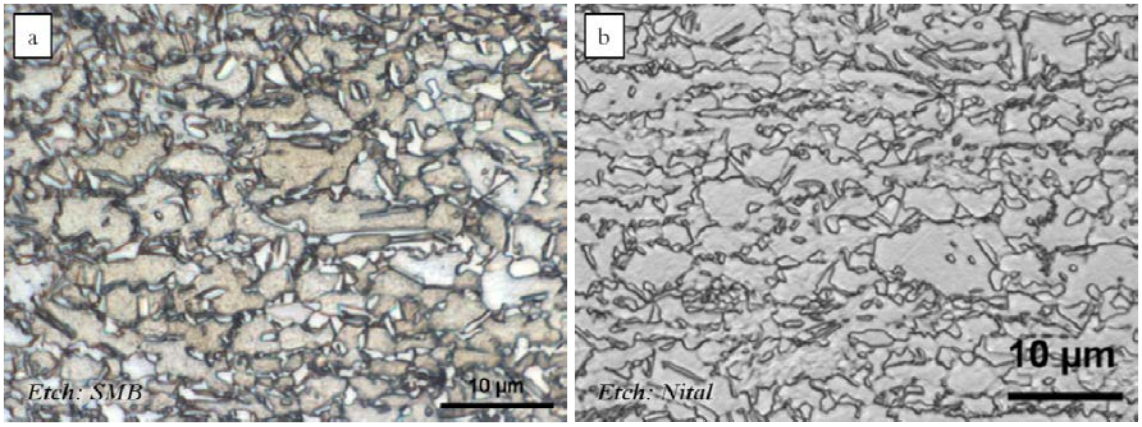

Fig. 4-3. RLM micrographs of TRIP BM etched with SMB (a) and Nital 2% (b).

The SMB etched microstructure attains various shades of brown with no correlation to the micro-constituents. Hence, the method is useless for the present microstructure analysis. The microstructure etched with Nital (Fig. 4-3 b) does not differentiate among the micro-constituents and only shows grain/phase boundaries.

The microstructure investigation by RLM after different etching methods reveals that only the modified LePera etching allows the separation of all four micro-constituents in the base material of TRIP steel.

Compared with the conventional LePera etching, the modified LePera etching improved the result, because martensite attains another color than retained austenite. Accordingly, it was possible to separate all four micro-constituents. Fig. 4-4 shows an example of the TRIP steel microstructure as observed by RLM after etching with the Modified LePera etching method.

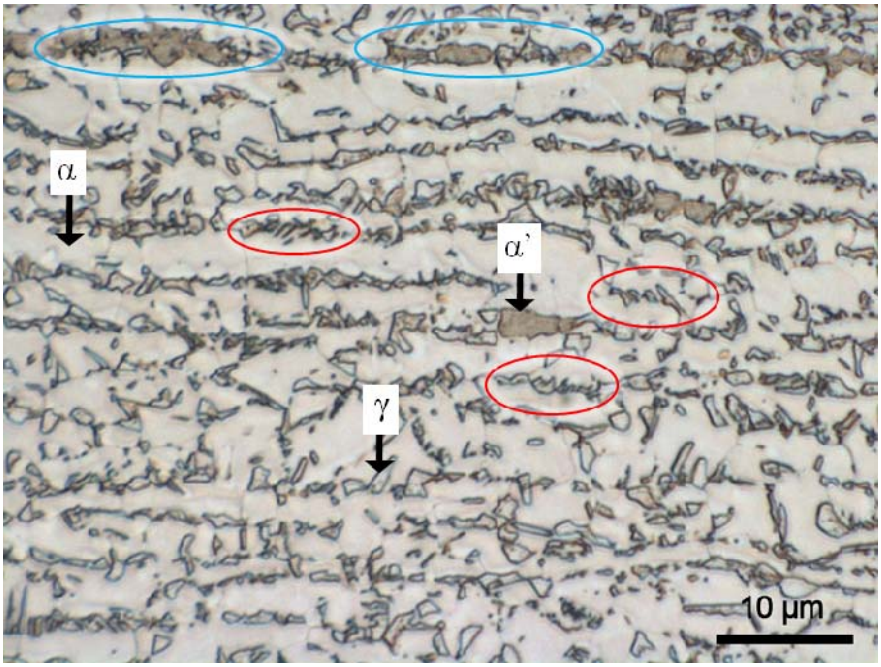

Fig. 4-4. RLM micrograph of TRIP steel BM microstructure etched with Modified LePera.. Bainite consisting of bainitic ferrite and retained austenite are marked with red ellipses. Bands of martensite are marked with blue ellipses.

According to the inventor of the Modified LePera technique [126] the four micro-constituents should attain the following colors: ferrite - beige, bainite - bluish brown, retained austenite - white, martensite - straw-color. In the micrograph in Fig. 4-4 it is seen that the major part of the microstructure is ferrite and it has attained a beige color as expected. Retained austenite was supposed to attain a white color; but no white grains were found in the microstructure. However, some small grains in the microstructure have attained a slightly brighter color than ferrite and that these regions indeed correspond to retained austenite (see section 4.3.3).

Bainite was expected to attain a bluish brown color, but no blue grains were observed in Fig. 4-4. In TRIP steels bainite is a combined structure of lamellae of retained austenite and bainitic ferrite and this lamellar morphology of bainite is identified in the microstructure in Fig. 4-4 (red ellipses). It is very likely that these regions are bainite, so that the bright elongated grains are austenite, and in-between the austenite grains bainitic ferrite is located. EBSD will be used to verify this.

The brown grains are most likely martensite (α'), as it was expected to attain "straw-color" according to the inventor of the etching technique [126]. In the top of the RLM image in Fig. 4-4 some large bands of martensite are marked with blue ellipses. The voluminous presence of martensite does not correspond to the findings with EBSD, where retained austenite was found with this morphology (see below). This indicates that the preparation method applied before RLM characterization, which involves mechanical grinding and polishing, induces austenite-to-martensite transformation. Therefore, quantification of the martensite amount in the BM microstructure should only be done from EBSD results.

A significant drawback of the color tint etching techniques, such as the Modified LePera technique, is the variation of the colors from one treatment to another. The colors may change due to small variations in alloy composition, orientation of the grains, presence of stresses etc. and it depends also on the quality of the etching solution (aging occurs). Several etching times were applied for the two etching steps in the Modified LePera etching to determine the optimum etching procedure.

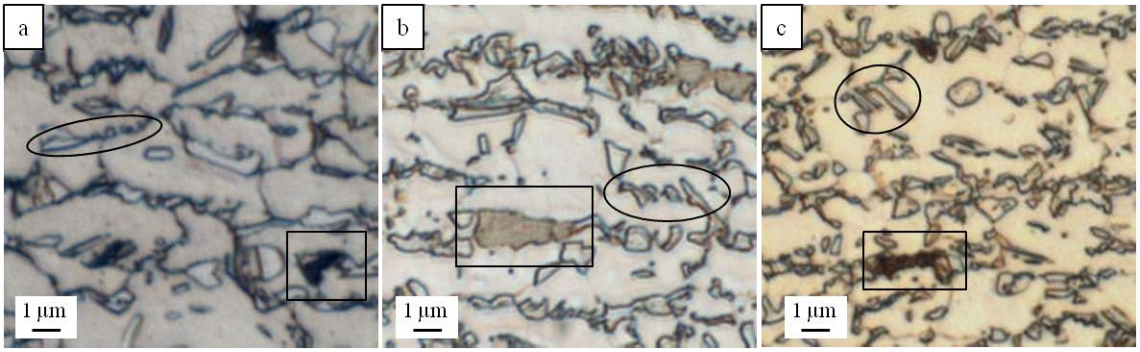

Fig. 4-5. TRIP steel microstructure after different etching times with Modified LePera [126]. Etching is done with Part 1 and 2, respectively, for the following periods; a) 16 and 6 seconds, b) 18 and 7 seconds, c) 18 and 8 seconds. Bainite is marked with ellipses and martensite is marked with boxes. Note that micrograph in b) is a magnified section from Fig. 4-4.

As seen from the micrographs, the etching result depends on the applied etching time. All micrographs attain completely different contrasts and nuances despite of the very small variation in etching times. In a), the small bright grains have attained a brighter color than in b) and c), which confirms that they are retained austenite grains as suggested above. Bainite appears similar in the three micrographs because it is mainly identified due to its morphology. On the contrary, martensite attains different colors in the three micrographs ranging from straw-colored (b) to black (a).

The results clearly indicate that color tint etching is very sensitive to small variations and it is recommended that the Modified LePera etching method is applied several times to optimize the etching result so that the right colors are attained, and to improve the reliability of the colors.

4.3.2 SEM

In Fig. 4-6 the microstructure of TRIP steel BM is shown after Nital etching, as observed with SEM.

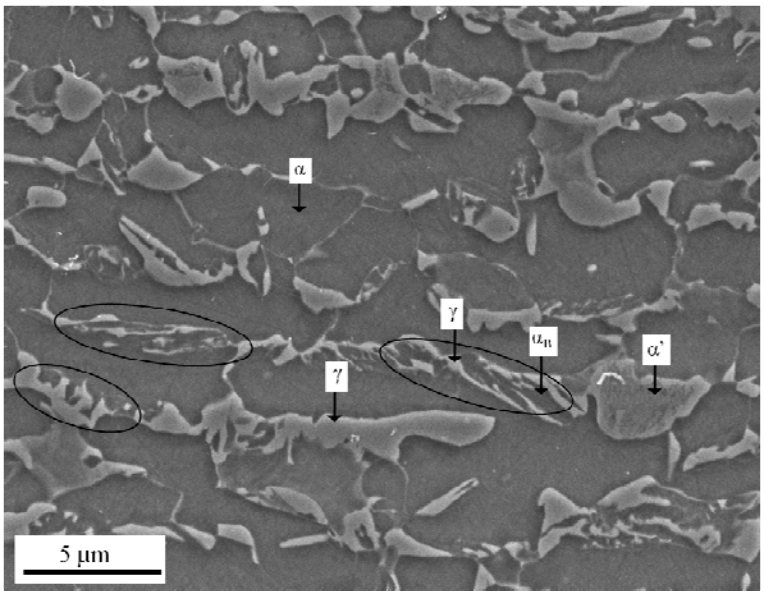

Fig. 4-6. SEM micrograph of the TRIP steel microstructure etched with Nital.

Ferrite is present as the large etched grains with a comparable morphology as the beige grains in the RLM micrograph in Fig. 4-4. The resolution of the SEM image is much better than the RLM image, hence, small details are much better resolved. Bainite is clearly seen as the regions with lamellar structure consisting of bainitic ferrite (α_B) and retained austenite (γ) (marked with ellipses in Fig. 4-6). Retained austenite is observed as un-etched grains with a smooth appearance. Martensite is identified because it has a rough appearance (α'). Only the rough appearance of martensite allows the separation between martensite and retained austenite in a SEM image. A procedure suggested to separate martensite and retained austenite, is to perform an annealing treatment (200-260°C) prior to SEM investigation, which would reveal temper the martensite reveals its rough structure [21][78]. However, in this case, the martensite already had such appearance without annealing.

Still, it is not completely confirmed that the small grains comprise retained austenite, as indicated in the RLM and SEM analysis. EBSD is the only method which can actually proof this.

It should be mentioned that the sample was prepared by mechanical grinding and polishing for the SEM characterization in a similar way as it was for RLM characterization. It was observed in the RLM micrograph in Fig. 4-4 that the amount of martensite had increased due to deformation-induced austenite-to-martensite transformation as a result of the preparation technique. The preparation technique is similar for SEM analysis, and it can therefore be expected that transformation has also occurred in the samples investigated with SEM. Therefore, the martensite observed in Fig. 4-6 was not necessarily present in the microstructure before preparation. Only the electropolishing applied before EBSD is mild enough to retain the unstable austenite in the microstructure.

4.3.3 EBSD

The EBSD characterization of TRIP steel also requires an investigation of the preparation method in order to identify the most suitable technique. Two main methods were applied; OP-S polishing and electropolishing. The volume fraction of retained austenite is easily determined from the EBSD data and it was found that after OP-S polishing and electropolishing the area fraction of f.c.c. was 8.3% and 15.3%, respectively. This result clearly indicates that a significant amount of retained austenite transforms during OP-S polishing. The vol% of austenite was measured to be 16 vol% from the XRD analysis, which will be shown later in the chapter. Since XRD diffracts in the volume, the effect of the preparation method is reduced, and the preparation is considered almost negligible for the austenite vol% determined with XRD. From comparing the vol% of austenite determined with XRD and the amount determined with EBSD, it is concluded that electropolishing does not cause a significant transformation of austenite. All EBSD characterizations performed in the present study will be performed on samples prepared by electropolishing.

Two types of electropolishing were applied; one with a commercial setup from Struers A/S, and another simple setup with a beaker and a power source. Both setups gave successful results without major differences. This indicates that the simple setup with a beaker and a power source is enough to fulfill the electropolishing of TRIP steel for EBSD. It is, however, important to ensure stirring of the electrolyte during electropolishing. The variation of the temperature gave an optimum result at about 10°C. The optimum voltage and time for electropolishing was found to be 16 V and 30-35 sec, respectively. These parameters differ from one alloy to another, and therefore, it was optimized for the present alloy before EBSD characterization.

In Fig. 4-7 an IQ and phase map including only austenite (green) of TRIP steel BM is shown. The b.c.c. phase is not colored, but is identified in all other points besides the green.

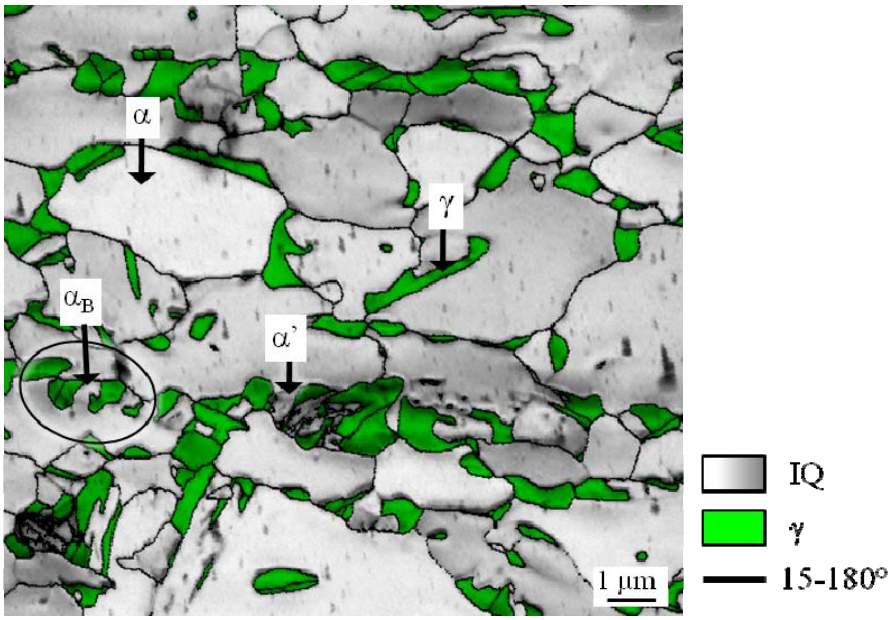

Fig. 4-7. EBSD map of TRIP steel BM. The ellipse indicates bainite.

From the EBSD map it is confirmed that the small grains are retained austenite. In the EBSD map bainite is also observed (marked with an ellipse) as regions consisting of “lamellar” bainitic ferrite and retained austenite. This observation is based on the morphology of the region, which was also done with RLM and SEM; EBSD confirms the presence of austenite in the lamellar structure.

Martensite is identified in Fig. 4-7 as grains with lower IQ, but also some lamellae of retained austenite are observed around the martensite grain. The reason for the low IQ in martensite is the distorted lattice and dislocation content of martensite, which causes poor diffraction conditions.

Bainitic ferrite has another characteristic property, which can be used for its identification. The processing method of TRIP steel is divided into two heat cycles: First, the formation of ferrite at an intercritical temperature, followed by holding at a lower temperature, where bainitic ferrite grows. The growth of ferrite and bainitic ferrite occurs from the same austenite grains, but there is a slight change in the growth mechanism, which will result in a minor orientation gradient from ferrite to bainitic ferrite [8]. This orientation gradient can be measured by EBSD and used for the distinction between ferrite and bainitic ferrite. Fig. 4-8 shows a magnified section of bainite from Fig. 4-7.

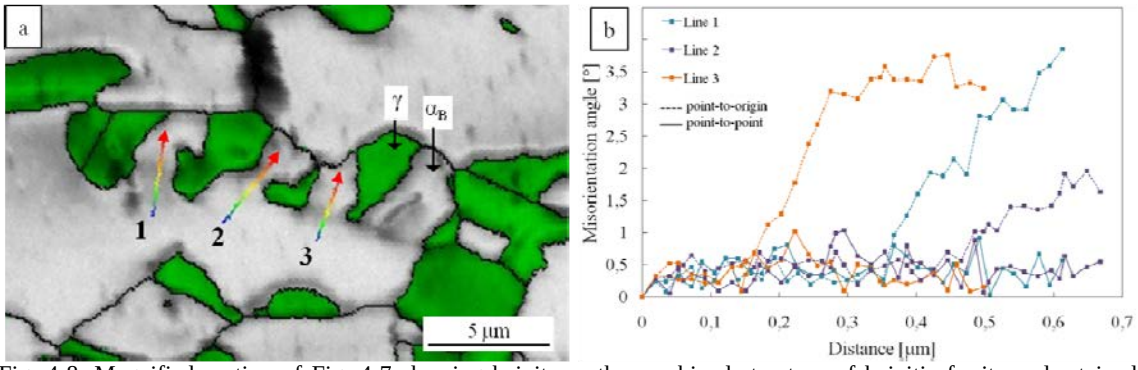

Fig. 4-8. Magnified section of Fig. 4-7 showing bainite as the combined structure of bainitic ferrite and retained austenite (a). Three misorientation lines are drawn in a) and their misorientation curves are shown in b).

For an investigation of a possible orientation gradient between ferrite and bainitic ferrite three point-to-origin lines were considered (lines given in Fig. 4-8). Clearly, there exists an orientation gradient between ferrite and bainitic ferrite (Fig. 4-8 b). This observation is consistent with the presence of bainitic ferrite in between the retained austenite lamellae.

Kernel Average Misorientation (KAM) is an EBSD function, which earlier has been described as a method to identify bainite in TRIP steel [134]. KAM determines local orientation gradients between a point and its surrounding points, in a kernel of a predetermined size. Thus, KAM can be used to identify the orientation gradient, which is present between bainitic ferrite and ferrite in TRIP steel. In Fig. 4-9 an EBSD map is shown that includes IQ and f.c.c. (green), and the red regions indicate b.c.c. points with a KAM value in the range 0.7-5° in a kernel of 100 nm.

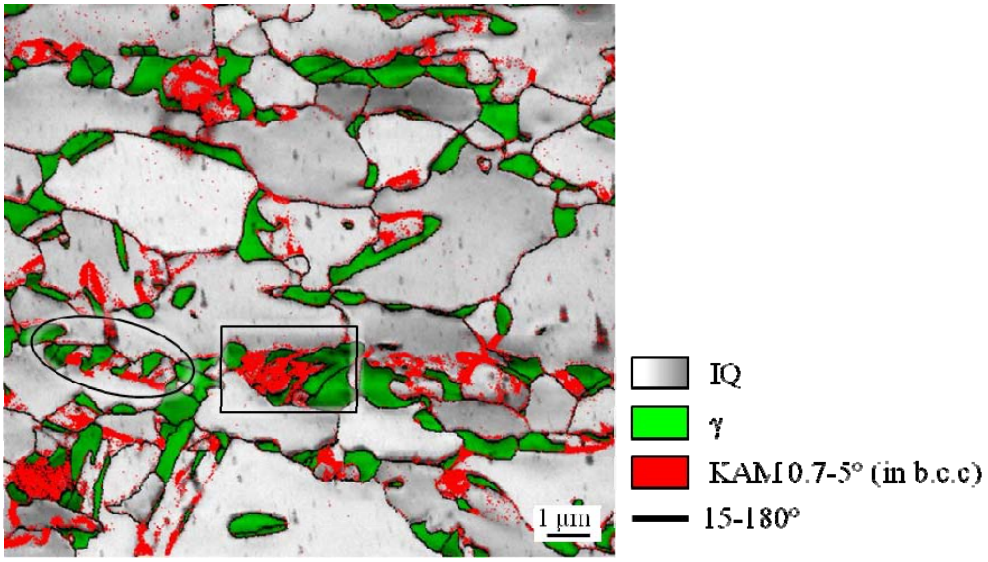

Fig. 4-9. EBSD map of TRIP steel microstructure, where the KAM function is used to identify bainitic ferrite. The ellipse marks bainite, whereas the box indicates martensite.

As seen from the map, bainitic ferrite (marked with an ellipse) is colored red indicating that the KAM value is 0.7-5°. This is in good agreement with the misorientation analysis in Fig. 4-8, which showed that the orientation of the grain changes between ferrite and bainitic ferrite. Another observation from the map is that martensite (marked with a box) is also colored red. If KAM was the only method to identify bainitic ferrite, martensite would have been wrongly identified as bainitic ferrite. Therefore, it is very important to check grain boundaries, IQ and orientation gradients before concluding, which grains are bainitic ferrite. In conclusion, the KAM function is a good method to identify bainitic ferrite, but since martensite is showing the same behavior in KAM analysis, other methods must be included to verify the result.

Before performing a separation of bainitic ferrite and martensite, first a thorough analysis and assessment of suitable threshold values for the KAM range and the size of the KAM kernel is necessary. The parameters to adjust in the KAM function include the size of the kernel, the misorientation range and a choice between calculation in only the perimeter of the kernel, or the entire kernel. The calculation of only the perimeter is preferred because including all points in the kernel implies a relatively long time for data processing, and it was found that including only the perimeter was sufficient for an identification of bainitic ferrite. In Fig. 4-10 the size of the kernel and the misorientation range are systematically changed.

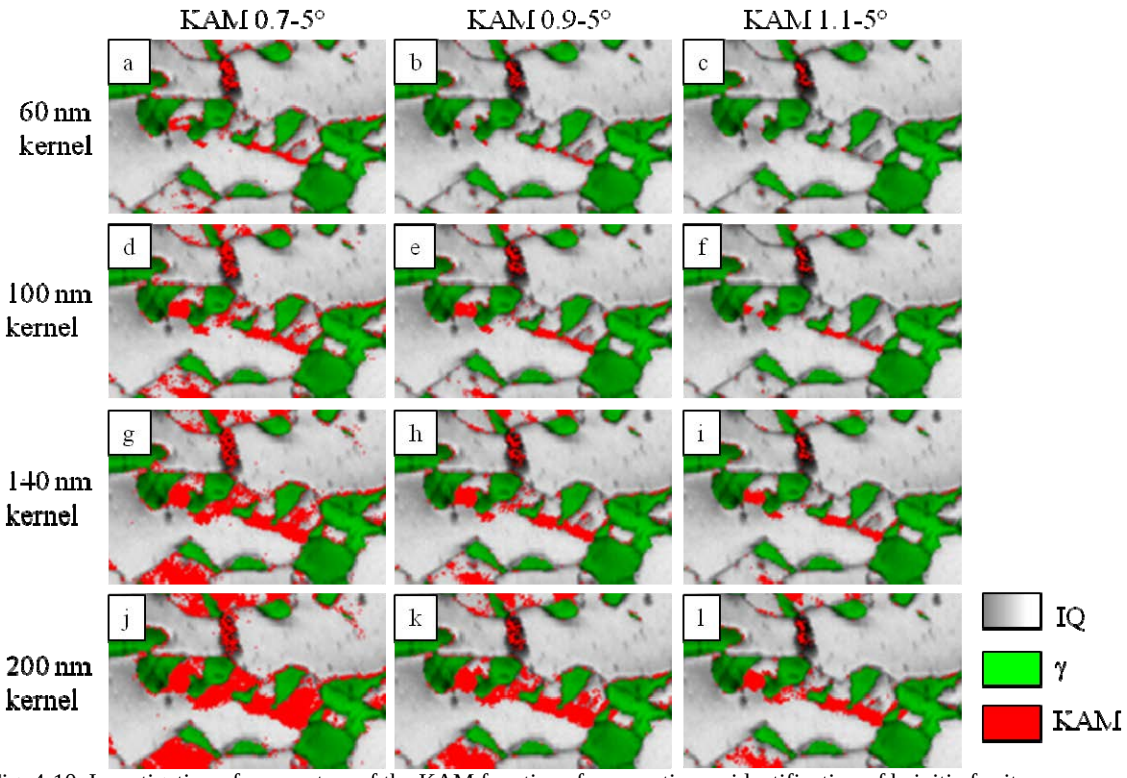

Fig. 4-10. Investigation of parameters of the KAM functions for an optimum identification of bainitic ferrite.

It is observed that the variation of the two parameters kernel size and misorientation range, leads to different coverage of the bainitic ferrite, and that an optimum for the combination of the two parameters has to be found. From the parameter study in Fig. 4-10 it is concluded that h, i, and l are acceptable solutions for the identification of bainitic ferrite with KAM. There are not too many scattered points in the matrix, and as much bainitic ferrite as possible is identified. Common for all solutions is that none of them fulfills a complete cover of the entire bainitic ferrite grain because only the transition between ferrite and bainitic ferrite is identified with KAM. Therefore, quantification of bainitic ferrite is not possible with this method, but it serves only as an indication of the location of bainitic ferrite.

It should be mentioned that the methods recommended in the literature for the identification of bainite by applying IQ [135] or the combination of IQ and CI [136] were applied in the present study. However, none of the methods was found successful; the results are therefore not presented here.

Martensite has some characteristic features that differ significantly from bainitic ferrite, which can be used for an unambiguous separation of the two phases. The IQ in the martensite grains is lower, which was easily seen in Fig. 4-7. In bainitic ferrite the IQ is almost identical to the neighboring ferrite. Another characteristic of martensite is the presence of many low angle misorientations. Lath martensite in steel has a well-known structure consisting of packets, blocks, sub-blocks and laths [137]. Sub-block boundaries are known to be low angle boundaries (LAGBs), and so are the lath boundaries, albeit with smaller misorientation angles [137]. The low IQ and presence of LAGBs in martensite can be used to identify the martensite grains in EBSD. Two functions are useful for the identification of martensite. The Grain Average Misorientation (GAM) function calculates the misorientation between neighboring points in a grain. The average misorientation value is calculated for the whole grain and assigned to all points within the grain. Another function capable of identifying martensite is by the Grain Average Image Quality (GAIQ), by which the average IQ of the grain is considered.

In Fig. 4-11 a magnified section of the EBSD map from Fig. 4-7 is shown, which contains both martensite and bainite regions. In the figure four maps are included, which are constructed by different methods, as described in the following.

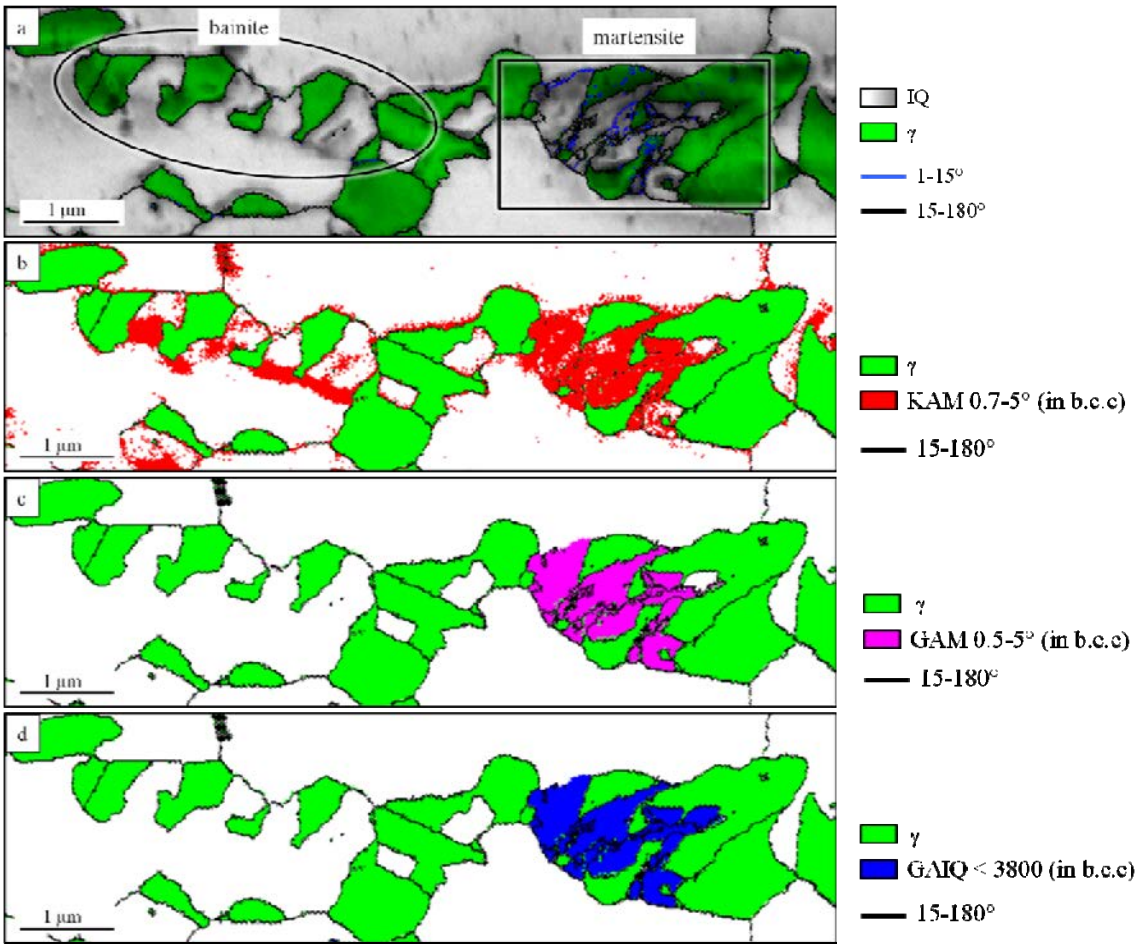

Fig. 4-11. Magnified section of EBSD map in Fig. 4-7 constructed with different methods for separation of martensite and bainite. See the text above and below for details about the methods.

Fig. 4-11 a) indicates with an ellipse and a box locations of bainite and martensite, respectively. In b) the KAM function is applied, which was also used in Fig. 4-9 to identify bainitic ferrite, but it is seen that also martensite is identified with KAM. In c) and d) the GAM and GAIQ functions, respectively, are applied in the b.c.c. phase. It is clear from the maps including GAM and GAIQ that only martensite is colored, and it points out the difference between bainite and martensite, which is not clear from the KAM map in b). A thorough investigation of the GAM and GAIQ maps (not shown here) revealed that both methods are equally useful for the identification of martensite in TRIP BM. Applying GAM for separation of ferrite and martensite in the heat treated and welded TRIP steel microstructures was far from successful, while GAIQ was concluded to be highly suitable for this purpose. Therefore, it is recommended to use GAIQ for the identification of martensite, because it allows for a comparison with the heat treated and welded TRIP steel microstructure. The drawback of GAIQ is the poor repeatability, because IQ depends on the surface preparation. Accordingly, the GAIQ has to be adjusted for each map, so it identifies martensite properly.

Based on the above findings it can be concluded that no single functions in EBSD can be used to quantify all micro-constituents in TRIP steel and determine their volume fraction. Firstly, because bainite is a combined structure of bainitic ferrite and retained austenite, and it is not possible to distinguish between austenite grains in bainite or otherwise. Secondly, bainitic ferrite cannot be quantified, because the KAM method only identifies the transition region between ferrite and bainitic ferrite. The content of martensite can be quantified from the b.c.c. fraction, by the GAIQ method, but it presumes that the surface is well prepared because IQ depends on the surface quality.

4.3.4 Comparison of RLM, SEM and EBSD

From the presented results, it can be concluded that EBSD is the method, which most reliably identifies the micro-constituents in the TRIP steel microstructure. EBSD is relatively time consuming and provides poor statistics as compared to the two other methods (RLM and SEM), and therefore, a combination of the three methods is preferred. Fig. 4-12 shows the TRIP steel microstructure as seen with RLM, SEM, and EBSD.

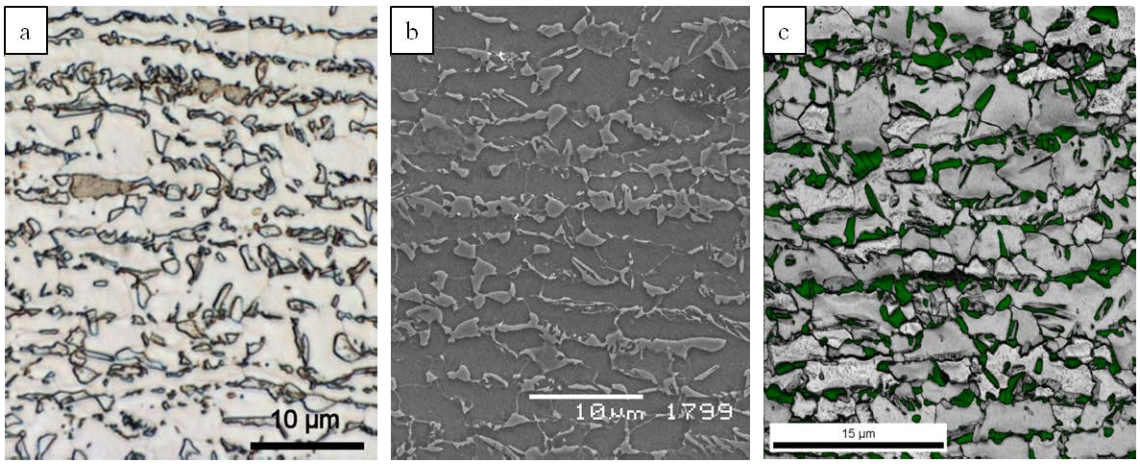

Fig. 4-12. TRIP steel BM microstructure as seen with RLM (a), SEM (b) and EBSD (c). The magnification is similar in the three micrographs.

The features in the microstructure are comparable in all three images. RLM is the fastest characterization method and it is possible to include a large area of the microstructure compared to the other methods. However, the result of the etching is affected by numerous parameters (see above) and the result must be verified by SEM or EBSD, preferable a combination of the two. A detailed comparison of the three micrographs is shown in Fig. 4-13.

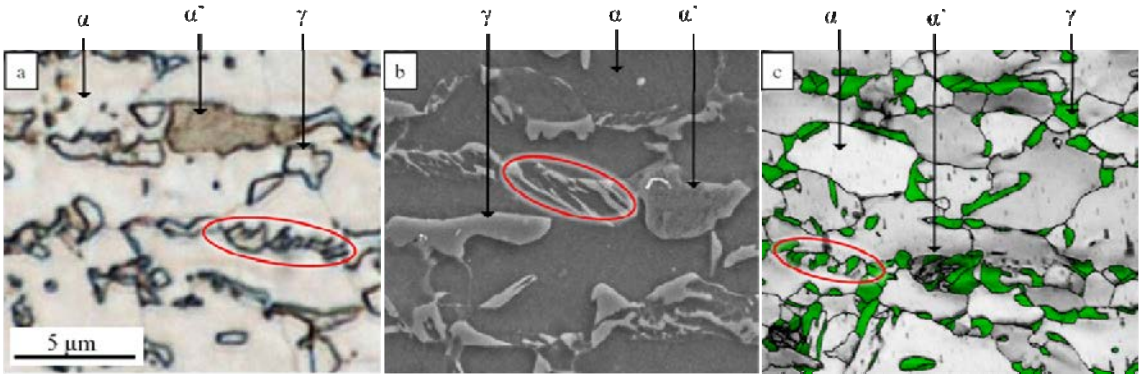

Fig. 4-13. Magnified section if TRIP steel microstructure as seen with RLM (a), SEM (b) and EBSD (c). Ferrite, martensite, and austenite are marked with arrows, and bainite is identified with red ellipses. The magnification of the three micrographs is similar.

All four micro-constituents are indicated in the micrographs in Fig. 4-13 and it is easy to see the similarity of the microstructures. Bainitic ferrite (red ellipses) is identified as the lamellar structure of bainitic ferrite and retained austenite, and the identical morphology of bainite is readily recognized in all three images. Martensite can also be identified in all three micrographs, but the confirmation of martensite is most reliable from the EBSD analysis since the colors in the RLM image can be misleading, and the lamellar structure as observed in SEM is not always visible. Austenite is very difficult to identify with RLM because the contrast difference between austenite and ferrite is rather small. Therefore, the EBSD analysis is necessary for the safe identification of austenite. The identification of austenite as the lamellar grains in bainite, as observed with EBSD, confirms the identification of bainite from the RLM and SEM images. All together, only the complementary use of RLM, SEM, and EBSD allows reliable identification of all micro-constituents in TRIP steel. Knowledge of characteristics of the micro-constituents will ease the separation.

4.4 Determination of the volume fraction of retained austenite

The volume fractions of austenite and ferrite were calculated from X-ray diffractograms measured from the base material. The calculation is based on the integrated intensity, and it assumes a random crystallographic orientation in the sample, which is probably not fulfilled with this sample, as the base material has a rolling history. According to the calculation standard, it is optional how many peaks are included in the analysis. Generally, the more peaks are included in the calculation, the more representative the calculated phase composition becomes, because in this way the presence of crystallographic texture is considered. The volume fraction was

calculated for two situations; either taking only two peaks (the high intensity peaks) into account or considering four peaks. The calculated volume fractions of austenite are listed in Table 4-3.

Table 4-3. Determination of the austenite volume fraction from XRD and EBSD.

Method	Peaks included	Vol% austenite
XRD	$(111)_\gamma + (110)_\alpha$	16
XRD	$(111)_\gamma + (200)_\gamma + (110)_\alpha + (200)_\alpha$	20
EBSD	-	15.3

The two XRD results differ by about 25 %. As a consequence of strong texture, the $(200)_\gamma$ and $(200)_\alpha$ peaks are very weak, which hinders accurate peak profile fitting. Since it can be expected that a Kurdjumov-Sachs orientation relation occurs between austenite and ferrite [1], a preferred presence of $(111)_\gamma$ will lead to a preferred presence of $(110)_\alpha$. Then, an estimate of the austenite content based on the two parallel lattice planes of the orientation relation is expected to be more accurate, than that based on a combination of strong and weak reflections. Therefore, it is concluded that the calculation based on only two peaks is the most reliable result for the present sample.

The result from the EBSD analysis agrees well with the volume fraction calculated from two peaks in the XRD results, i.e. 15-16 vol%.

4.5 Determination of carbon content in austenite and ferrite

In the XRD diffractograms, the $(110)_\alpha$ and $(111)_\gamma$ peaks were observed to be shifted towards lower diffraction angles compared with the theoretical peak positions for pure iron. In general, a shift of the peaks corresponds to changes in the spacing of lattice planes (d-value) due to alloying elements or macrostresses, but also alignment errors of the instrument would affect the peak position. In the XRD diffractogram the alignment of the instrument was not found to be the cause of peak shift, since the $(110)_\alpha$ peak of the Fe (b.c.c.) standard agrees with the database value (will be shown in Section 7.10), which indicates that the alignment is good in the investigated 2θ-range and also inaccurate sample displacement can be excluded. Therefore, the peak shift has to be caused by the material itself, i.e. the presence of alloying elements or macrostresses, or a combination hereof. The present TRIP steel contains alloying elements, which will certainly influence the lattice parameter of the phases, and in particular interstitially dissolved carbon contributes to an increase of the lattice parameter. About the additional contribution by macrostresses can only be speculated, because the magnitude and distribution of macrostresses including possible depth gradients cannot be estimated straightforwardly. Dedicated stress analysis by XRD would enable a determination of the state of stresses, but this requires extensive diffraction analysis (by tilting the sample during measurement) to include

other planes than only those parallel with the sample surface, and it was not performed in the present study.

From the d-spacing according to the 2θ-shift the carbon content of the two main phases, austenite and ferrite, was estimated. This does not take the contribution of stresses into account and, therefore, only serve as an indication of the influence of carbon onto the peak shifts. The carbon content was calculated to be 1.259 wt% in austenite, and 0.138 wt% in ferrite, based on the °2θ shifts of the $(110)_{\alpha}$ and $(111)_{\gamma}$ peaks. The calculations were also applied on the other, low intensity peaks, and comparable results were obtained. Using the above determined vol% of the two phases in the steel (16 vol% austenite), the total carbon content of the alloy will correspondingly be 0.317 wt%, which is slightly higher than the specified carbon content in the steel (0.24 wt%). Although the effect of macrostresses is not considered in this estimation (as mentioned above), the result indicates the significant effect of carbon on the measured peak shifts.

5 Effect of deformation and heat on TRIP steel

5.1 In situ tensile test of TRIP steel

Four EBSD maps obtained on the same area during the in-situ tensile test are shown in Fig. 5-1.

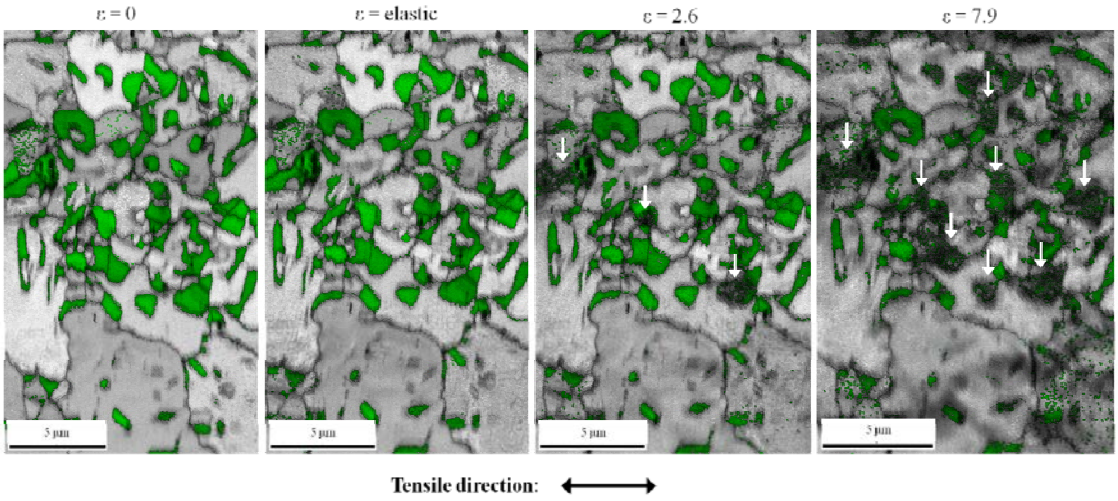

Fig. 5-1. EBSD maps after exposure to four strain levels and unloading. In the IQ maps, additionally, the f.c.c. phase is green, and HAGBs are marked as black lines. The tensile direction is horizontal as indicated by the arrow below the maps. Transformed austenite is marked by white arrows.

After elastic straining, no transformation of austenite is observed in the EBSD map. It is confirmed by the volume fraction of austenite, which is not changed significantly after elastic straining. However, a change in IQ is observed due to elastic straining. The average IQ of the

overall EBSD map is 4700 before straining and 4000 after elastic straining. The average IQ of an EBSD map can only be compared for maps being measured on the same area of a sample measured with the same diffraction conditions, which was the case for these two measurements. The average IQ is lowered equally in the f.c.c. and b.c.c. phases, indicating that poorer diffraction conditions apply for both phases.

As strain is increased to the plastic strain levels 2.6 and 7.9, the austenite grains transform into martensite, which is indicated by white arrows in Fig. 5-1. The transformed austenite grains are identified as low IQ regions with erroneous indexing due to low CI. No b.c.t. crystal structure was found for martensite, which is related to the low carbon content in the TRIP steel, resulting in a crystal lattice of martensite close to cubic, and the identification of martensite cannot be based on the crystal structure. Nevertheless, martensite contains internal stresses leading to poor diffraction conditions, which induces low IQ and low CI. Furthermore, volume expansions associated with the austenite-to-martensite transformation will contribute to the low IQ of the transformed austenite grains because martensite will protrude from the polished surface. Therefore, transformed austenite appears as low IQ regions, which are erroneously indexed and contain uncorrelated pixels of b.c.c. and f.c.c., including HAGBs.

The volume expansions associated with slip planes protruding from the surface as a result of plastic deformation is assumed to be less significant for the image quality than the actual transformation, because the image quality of the ferrite grains is apparently less affected than austenite at high strain.

5.1.1 Development of the austenite volume fraction upon straining

The volume fraction of austenite is determined by the TSL OIM Analysis software at the various strain levels. The austenite vol% as a function of strain level is shown in Fig. 5-2 and compared with two studies from the literature having the most comparable initial austenite vol% [88][23]. Furthermore, an extra point of the initial austenite vol% is included in Fig. 5-2, which represents the austenite vol% determined over a large area of the studied sample before straining, after specifications from [138].

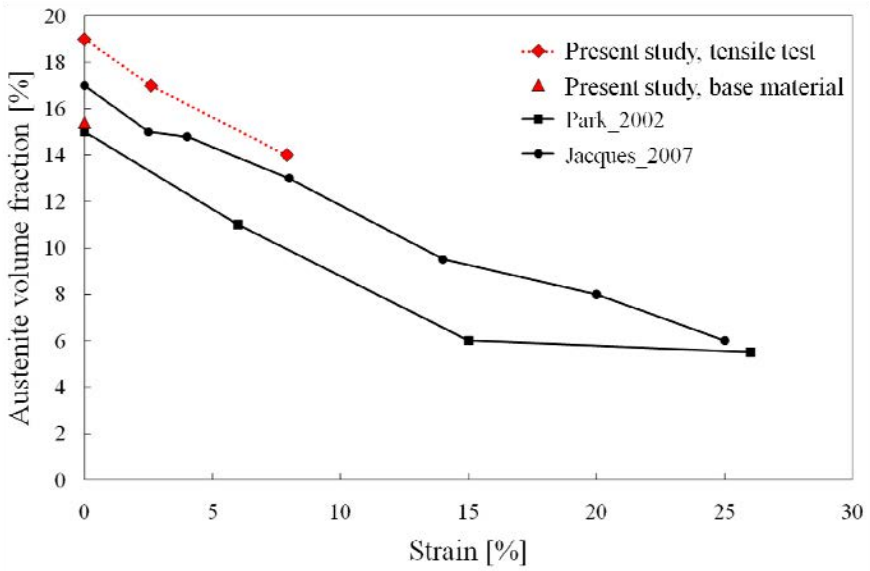

Fig. 5-2. The volume fraction of austenite as a function of the strain level for the present study, in comparison with two selected studies from the literature [88][23]. In the graph is also included a point measured from a larger area of the base material.

It is seen that the three curves are comparable, both in terms of initial austenite fraction and the slope of the curves. Even though the curves show similar characteristics, the three steels represented in Fig. 5-2 are not comparable regarding any of the factors suggested to be significant for the initial austenite content (as described in Chapter 2 - Background); composition, heat treatment, and analysis technique. It is also observed in Fig. 5-2 that the initial austenite fraction is slightly higher in the tensile test area than in the base material. Since the aim of the present study is to investigate the austenite grains, the in situ EBSD measurement area was selected based on its higher fraction of austenite. The base material measurement is a statistically reliable measure for the austenite vol% in the alloy and it confirms the comparability of the present study with the two studies from the literature in Fig. 5-2.

Thermodynamic calculations were conducted with Thermo-Calc (TCFE6.1 steel database) to calculate the driving force for the transformation of austenite-to-ferrite with the aim of estimating the stability of austenite in unstrained condition as compared to martensite in the various TRIP steel grades presented in Fig. 2-15 and Fig. 5-2. The driving force calculations are only based on the chemical composition. It was found that the driving force for austenite-to-ferrite differs by less than 5% for all alloys presented in Fig. 2-15. For the two steel grades with the most diverging compositions, Al-Mn-Si and Si-Mn steel, the driving force was found to be 5796 J/mole and 5503 J/mole for the Al-Mn-Si steel and Si-Mn steel, respectively. The small difference in driving force indicates that the influence of composition on the stability of austenite is small for the various alloys, and it confirms that the initial austenite volume fraction and development upon straining is not significantly controlled by the composition.

5.1.2 Effect of grain size on transformation

To investigate the effect of austenite grain size on the stability against deformation, the austenite grains are color coded according to their size (area), and the EBSD maps from the three strain levels are shown in Fig. 5-3 together with a diagram summarizing the fraction of each grain size. The elastically strained condition is identical to the non-strained condition and is therefore not presented.

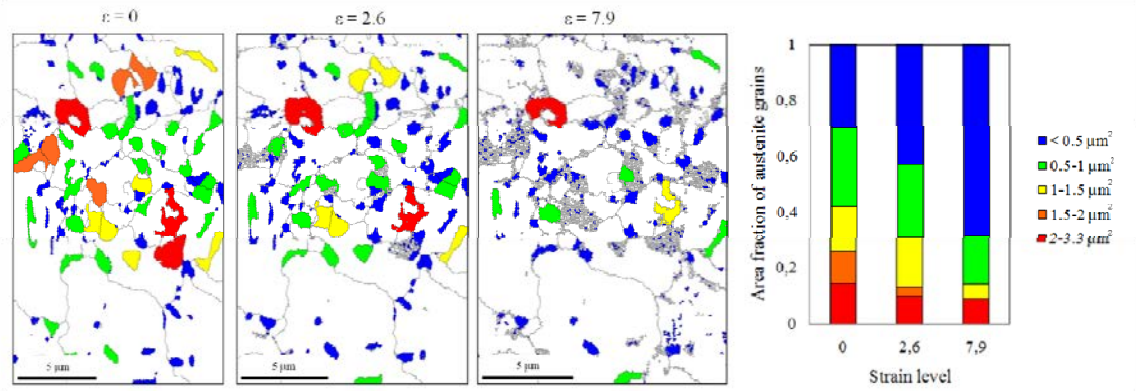

Fig. 5-3. EBSD maps showing the grain size (area) of austenite at the three strain levels, and a diagram showing the fraction of each grain size interval at each strain level. EBSD maps contain grain size in colors and HAGBs as black lines.

It follows from the EBSD maps that primarily the large grains disappear as strain is increased. At the highest strain, ε=7.9, the fraction of small grains (blue color) is larger than 0.60, and, within the investigated area, only one large grain (red color) has remained untransformed. It is observed that some grains are reduced in size as a result of gradual transformation and hence contribute to the fraction of grains with a smaller area, at high strain. The calculation of grain size fractions does not take the shrinking of grains into account, and therefore the volume fraction of small grains at highest strain is a combination of small grains remained from unstrained condition, and also grains which have shrunk. This uncertainty also applies for other measurement techniques applied in the literature, albeit that only EBSD can identify the gradual transformation. Nevertheless, it is clear from the present data that small grains are more stable than large grains, as follows from Fig. 5-3: the blue grains identified before straining, have not (gradually or completely) transformed during deformation (blue color).

The effect of grain size on the stability of austenite grains is often reported in the literature [15][78][80][83][86][23]. The grain size is closely connected to the carbon content such that small grains generally contain a higher carbon content. Particularly, austenite grains present as fine plates in between bainitic ferrite have a relatively high amount of carbon, and are therefore very stable. These grains are so stable that they often will not transform into martensite upon

straining and consequently do not contribute to the TRIP effect [78][86]. The effect of bainitic ferrite on the stability of austenite grains is described further in Section 5.1.5.

The EBSD technique cannot be used to verify or confirm whether there is a correlation between carbon content and grain size but the outstanding advantage of the present EBSD analysis is the observation of the gradually transforming grains. The gradual transformation of austenite grains was identified because of the direct investigation of the microstructure during the in situ tensile test. When austenite grains transform gradually they shrink and become considered as small grains at higher strain levels, and thereby contribute to the fraction of small grains. The studies presented in the literature are mostly investigating the development of grain size by bulk measurements, which, at best, indicate the microstructure without direct visualization. As a result, the shrinkage of grains is not identified in the quantitative grain size analyses.

5.1.3 Effect of location of austenite grains on transformation

It is of interest to investigate whether a correlation exists between the location of the austenite grains in the microstructure and their stability against strain-induced transformation. To this end distinction is made between austenite grains embedded in ferrite grains (at the exposed surface), austenite grains bound by two ferrite grains, and austenite grains bound by more than two ferrite grains. After applying the highest strain level (ε=7.9), three types of transformation state occur; no transformation, gradual transformation, and total transformation. Fig. 5-4 shows a graph presenting the number fraction of the various locations of austenite grains for each transformation state.

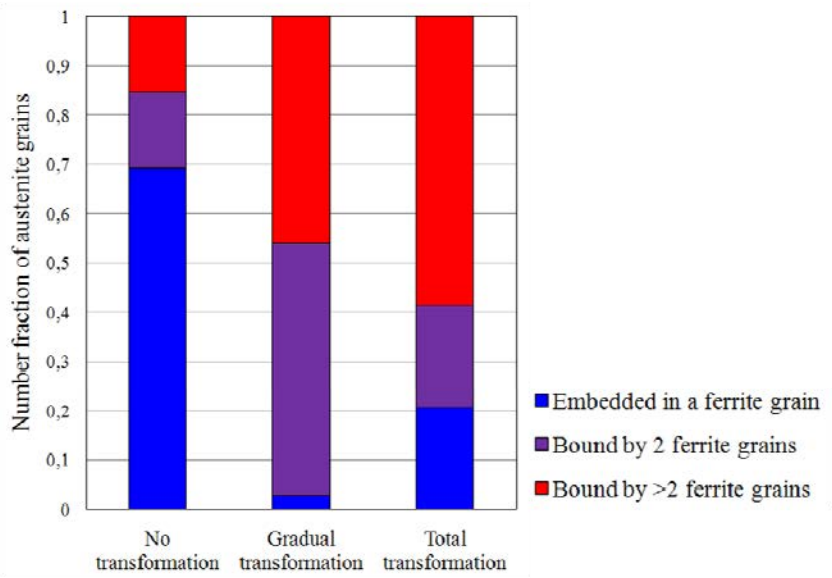

Fig. 5-4. Graph showing the austenite transformation state at ε=7.9 with respect to the location in the ferrite matrix.

Clearly, most of the austenite grains embedded in ferrite grains remain untransformed after straining and most of the austenite grains bound by two or more ferrite grains are (gradually) transformed after straining. These results strongly suggest that the austenite grains embedded in a ferrite grain are more stable than the grains located at grain boundaries.

According to the thermal history of TRIP steels, all austenite grains are connected to ferrite grain boundaries in unstrained condition. Therefore, strictly speaking the analysis including austenite embedded in ferrite grains does not make sense, and it is impossible to verify how these embedded austenite grains are connected to the ferrite grains, because this is not occurring in the plane of investigation. Hence, embedded austenite grains should be conceived as grains more remote from a ferrite grain boundary in the plane of investigation. Nevertheless, a trend is observed that austenite grains adjacent to ferrite grain boundaries transform more easily than austenite grains more remote from a ferrite grain boundary, at the exposed surface.

Considering only the two main phases in the TRIP steel microstructure: ferrite and austenite, the mechanical behavior during deformation will attain a two-component deformation behavior. Austenite has the highest yield strength due to the higher carbon content and ferrite will deform plastically in the initial part of straining, where austenite is only elastically loaded. The plastic deformation of ferrite grains adjacent to austenite grains induces additional forces on austenite by shear due to the differently oriented ferrite grains [139]. As a result, if austenite is surrounded by several ferrite grains, the shear stresses imposed onto the austenite grain will attain a more complicated stress state and the austenite grain will be more strongly affected and more prone to deformation. The shear stresses are highest at the austenite-ferrite grain boundaries, and, consequently, the austenite-to-martensite transformation will more easily initiate at grain boundaries.

In Fig. 5-4 it was found that austenite grains surrounded by two or more ferrite grains transform more easily than grains embedded in one ferrite grain. Furthermore, it is indicated that the strain-induced austenite-to-martensite transformation initiates at locations where austenite is bound by (at least) two different ferrite orientations. The effect of the neighboring ferrite grains depends of the critical resolved shear stress in the differently oriented grains, and this requires further investigations.

5.1.4 Gradual transformation of austenite grains

The observation of partially transformed grains leads to a more detailed investigation of the transformation behavior. For illustration of the two transformation modes, sections of the EBSD maps in Fig. 5-1 are magnified in Fig. 5-5 and Fig. 5-6.

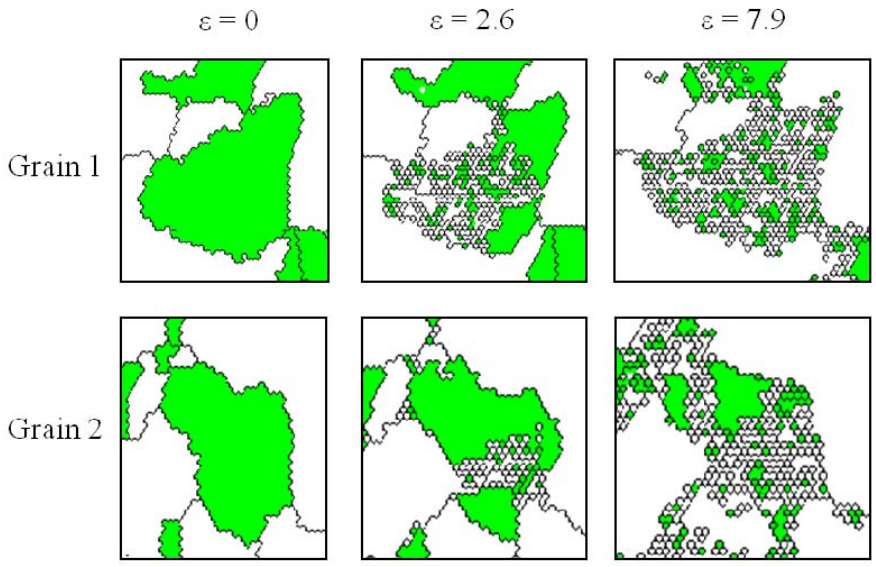

Fig. 5-5. Two selected grains illustrating gradual transformation of austenite. Maps contain the f.c.c. phase (marked green) and HAGBs as black lines.

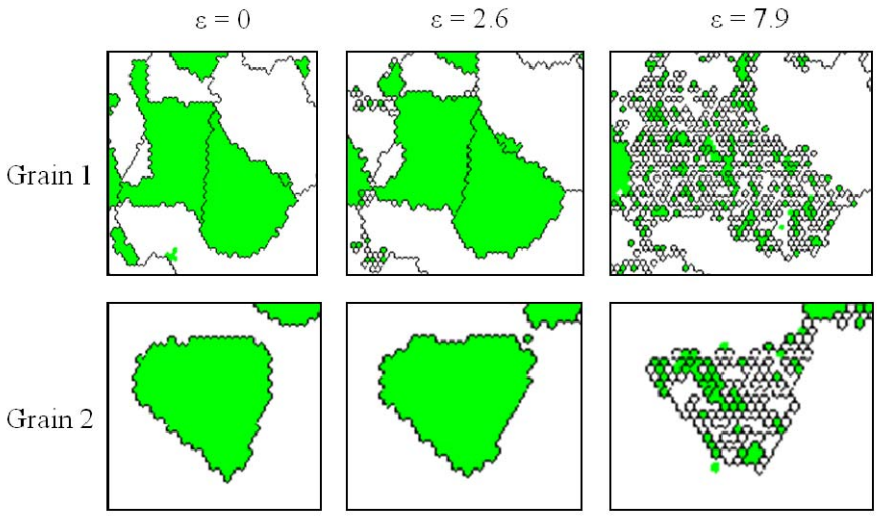

Fig. 5-6. Two selected grains illustrating total transformation of austenite. Maps contain the f.c.c. phase (marked green) and HAGBs as black lines.

A stepwise transformation is not expected, since the austenite-to-martensite transformation is a displacive transformation mechanism and therefore intuitively expected to occur in one step. However, the results from clearly indicate that for some grains the austenite-to-martensite transformation occurs gradually. The confirmation of gradually transforming grains also explains the presence of partially transformed grains in Fig. 5-3 in the grain size analysis.

There is a tendency that partial transformation occurs at low strain (ε = 2.6) whereas the total transformation does not begin before high strain is applied (ε = 7.9). It should also be noted that the observed one-step transformation may be gradual in-between the analyzed strain levels, but this cannot be verified from the present EBSD maps.

Some studies in the literature also report a gradual transformation of austenite to martensite during cooling. In one study, TRIP steel was investigated with TEM after straining and it was observed that some austenite grains were only partially transformed [78]. Other studies report a gradual transformation of austenite, as detected with synchrotron X-ray diffraction experiments, and thus without direct microstructure evidence [86][140][141]. A gradual transformation of austenite-to-martensite is, therefore, not completely unexpected. In the present study the direct visualization of individual grains strongly proofs the occurrence of gradual transformation of austenite to martensite during straining.

It is still not fully understood why the transformation occurs gradually, but the most probable explanation is related to the carbon content of the austenite grain. The carbon content can vary significantly within one austenite grain and, as a result, the M_s temperature varies [91]. Therefore, one part of an austenite grain with a higher M_s temperature transforms easier than the other part leaving the remaining part of the grain un-transformed. If the M_s is very low for the

remaining part of the grain, transformation can only proceed at significantly higher strain, or it will remain untransformed. There are also two other effects, which may contribute to the gradual transformation. Firstly, when austenite grains initiate the transformation to martensite, the stress states in martensite and its surroundings are changed and can counteract the progress of the transformation. Secondly, the presence of martensite in the microstructure before deformation can affect the transformation to become gradual. It is common that TRIP steels contain some martensite in the non-deformed microstructure if some austenite grains have not been sufficiently enriched with carbon after aging at the bainite holding temperature. Martensite has a higher yield strength than austenite [82][23], and the difference in yield strength will cause stress partitioning among the two phases when TRIP steel is exposed to deformation. During deformation, martensite will locally shield austenite from plastic deformation and austenite will become less affected by the deformation and the transformation is reduced. In the present study, thermally formed martensite was not present in the initial microstructure, and, therefore, this effect cannot be the cause for the gradual transformation.

5.1.5 Effect of bainitic ferrite on transformation

The location of bainitic ferrite near austenite grains is also expected to play a role for the stability of austenite. The presence of bainitic ferrite in the microstructure before straining is compared to the transformation state of austenite grains after straining to highest strain level (ε = 7.9) in Fig. 5-7.

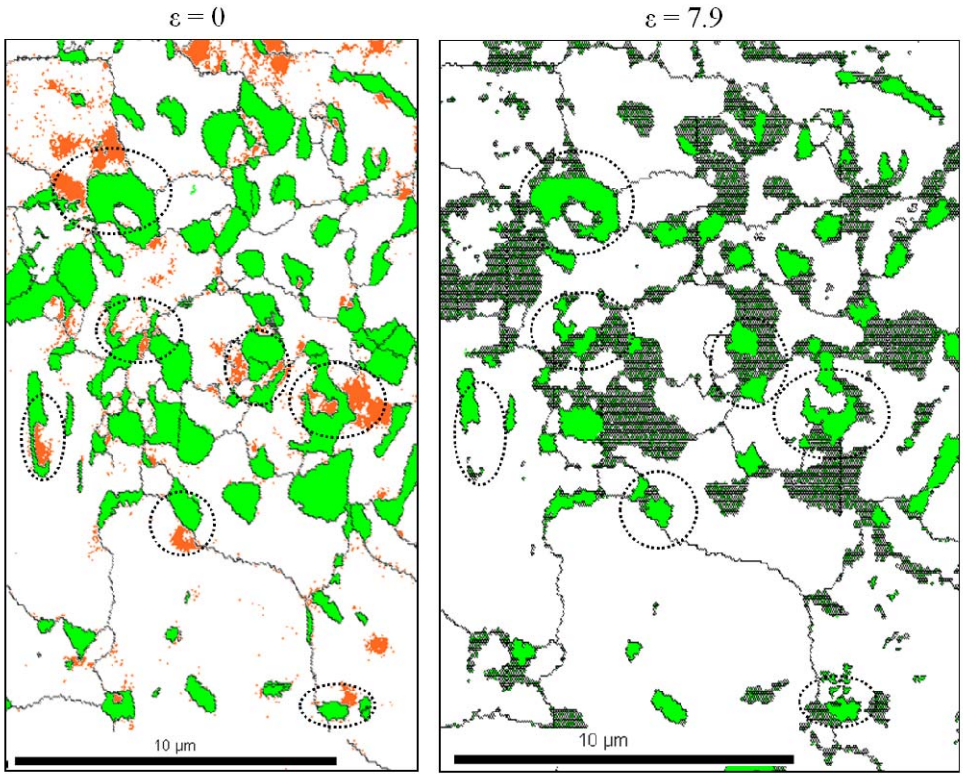

Fig. 5-7. The influence of bainitic ferrite on the austenite stability as seen from non-strained condition (ε=0) and highest strain level (ε=7.9). The EBSD map at ε=0 contains f.c.c. (green), bainitic ferrite (orange), and HAGBs (black lines). The EBSD map at ε=7.9 contains f.c.c. (green) and HAGBs (black lines). Bainitic ferrite is identified with KAM in the range 1.5-5°, in a kernel of 300 nm.

Generally, the austenite grains surrounded by bainitic ferrite at ε = 0 are retained untransformed at ε = 7.9, which is indicated by ellipses in Fig. 5-7. Based on this observation, it can be concluded that the presence of bainitic ferrite in the vicinity of austenite has a significant influence on the stability of austenite against transformation. There may be several reasons for a higher stability of austenite near bainitic ferrite. The most probable reason is that a more progressed bainite transformation will increase the carbon content of the adjacent austenite grains and, hence, provide higher stability of the austenite grains [8]. Furthermore, the formation of bainitic ferrite instead of ferrite adjacent to austenite will affect the stresses acting onto the neighboring austenite.

It is observed from Fig. 5-7 that the morphology of austenite and bainitic ferrite does not attain the characteristic plate shape, as is generally seen in TRIP steels. This is related to the sample section, and in the present study the plane of view is the normal direction and normally the characteristic plate morphology of bainitic ferrite and austenite is observed when the rolling direction is the plane of view (see Fig. 4-2).

It is clear from Fig. 5-7 that the presence of bainitic ferrite adjacent to austenite grains is reducing the austenite transformation during the tensile experiment. It is well-known that bainitic ferrite will influence the austenite stability significantly, which can occur chemically as well as mechanically [79][78][86][8]. The chemical effect of bainitic ferrite is caused by carbon redistribution into the austenite grains, when bainitic ferrite is formed, thereby leading to higher carbon content and higher stability of the austenite grains adjacent to bainitic ferrite [86]. The mechanical effect of bainitic ferrite originates from the change in stress state in the volume around austenite as a consequence of the development of bainitic ferrite. These stresses suppress the martensitic transformation of the neighboring austenite grains due to geometrical restrictions [78][8].

Although the effect of bainitic ferrite on austenite stability are well-known, it has never previously been confirmed by direct investigations of TRIP steel microstructure during deformation in the way that it has been in the present study. It is not possible to verify whether the effect is predominantly chemical or mechanical, but since the investigation is performed on a free surface, the hydrostatic effect of bainitic ferrite is expected to be reduced, and it can be presumed that the effect is mainly chemical.

5.1.6 After fracture

The in situ investigation was described until a strain level of 7.9% was reached. The tensile testing was continued until fracture occurred. After fracture, the sample was re-polished and EBSD investigation was carried out in a region close to the fracture. Fig. 5-8 shows IQ maps of TRIP steel before straining and after fracture, respectively.

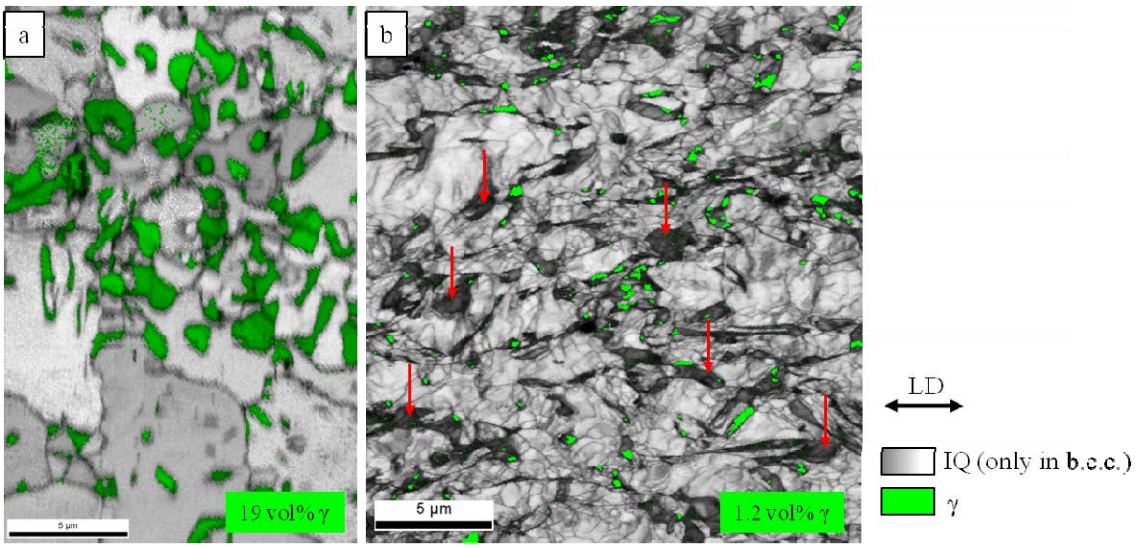

Fig. 5-8. IQ maps of TRIP steel before the tensile test (a) and after straining until fracture (b). Note that the two maps are not measured in the same area.

The low IQ grains observed after fracture (red arrows) are the strain-induced martensite grains, which have formed from the austenite grains. It is observed that 1.2 % austenite (green) has retained in the microstructure after straining. The retained austenite grains are observed in more detail in Fig. 5-9.

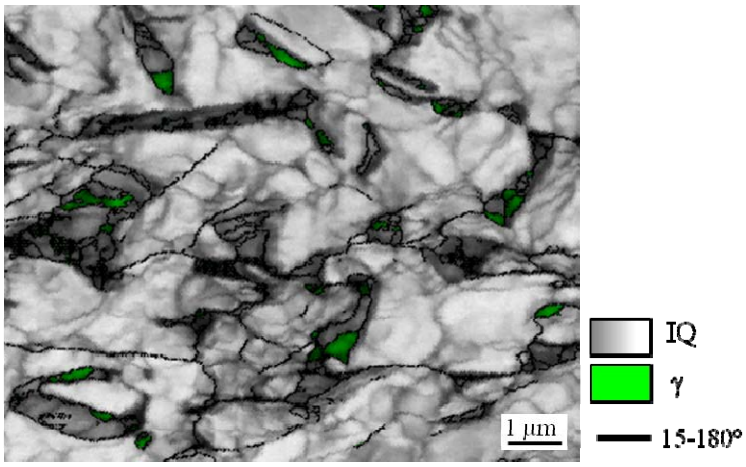

Fig. 5-9. Magnified section of Fig. 5-8 (including also HAGBs) showing the microstructure after fracture.

It is observed that austenite grains have retained primarily in the circumference of the martensite grains, which are seen as the low IQ grains. It is also observed from the micrograph that the

ferrite matrix is heavily deformed, which is evident from the blurry IQ coloring in the ferrite grains. The appearance of the IQ inside of ferrite grains appear as grain boundaries, in Fig. 5-10 the presence of grain boundaries is investigated.

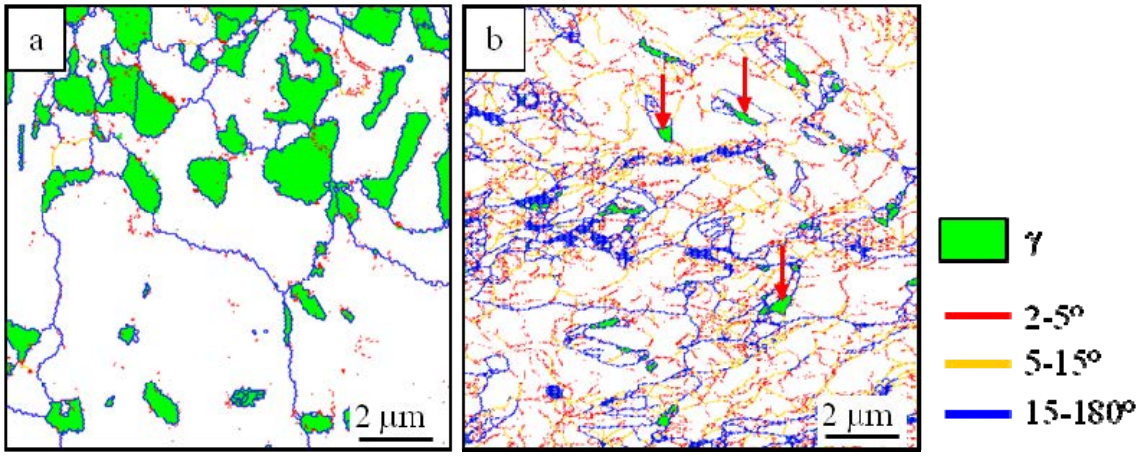

Fig. 5-10. Grain boundary maps of TRIP steel before straining (a) and after fracture (b).

Before straining, the ferrite matrix (white) has only few LAGBs (red and yellow lines) and these are mainly located near HAGBs (blue lines). After fracture, there is a considerable amount of LAGBs in the microstructure, particularly 2-5° LAGBs. The LAGBs are bound by HAGBs and their number decreases towards the middle of the ferrite grains. This is an indication that the dislocation density is more concentrated near HAGBs, and becomes more spread out in the center of the ferrite grain. It is observed in the fractured sample that several retained austenite grains (red arrows) are located in areas with few LAGBs, which might indicate that there is a connection between the transformation of austenite and the areas of the ferrite grains, which contain less LAGBs.

5.1.7 Suitability of EBSD measurements

Austenite grains are mechanically stabilized in the bulk microstructure of TRIP steel but when the steel is polished for microstructure characterization, the austenite grains become freely exposed to the surface and this results in a different transformation behavior. In the present study it is acknowledged that the effect of the free surface will affect the results but since the development of the austenite volume fraction upon straining is comparable with literature findings, it is assumed that the effect of the free surface did not influence the results notably.

A further disadvantage of investigating the microstructure from a polished surface is that the microstructure is represented in two dimensions without taking the three-dimensional microstructure into consideration. Accordingly, results on grain size and location of grain boundaries may not be representative for the bulk material. Three-dimensional investigation of TRIP steel involving serial sectioning with ion milling is not an option since austenite would transform into martensite during ion milling [124].

Finally, the in situ experiment was restricted to a relative small area of the sample, because a compromise between high resolution map and time of the investigation must be found. The EBSD measurement over a large area of the sample previous to the in situ investigation has shown that the fraction of austenite in the sample was comparable with literature.

5.1.8 Conclusion

The ability of austenite to resist its deformation-induced transformation to martensite depends on its composition, size and location of in the microstructure. The present study allows to conclude that size and location of austenite grains play a significant role in the retention of austenite during deformation. Austenite grains are more stable for a smaller grain size, for fewer neighboring ferrite grains and for the presence of neighboring bainitic ferrite.

Although the present findings of austenite stability in relation to the grain size are consistent with previous investigations applying global techniques as XRD, they show for the first time clear evidence for a gradual transformation of austenite grains.

It is evident that EBSD is a powerful technique to understand the localized microstructure behavior such as the gradual transformation of austenite to martensite.

5.2 Heat treatment of TRIP steel

As outlined in Section 3.5, samples of TRIP steel base material were heat treated at various temperatures to simulate the thermal cycle during welding. The heat treatments were applied for 5 and 10 seconds. The samples heat treated for 5 seconds contained a large amount of un-indexed points in the EBSD measurements. As a consequence, only the EBSD maps from the 10 seconds treatments are presented here.

5.2.1 Quantitative analyses

Martensite can be identified with EBSD using the GAIQ function (cf. Section 4.3.3). A threshold value is selected so that martensite grains became separated from the ferrite grains, i.e. martensite has a lower IQ than ferrite. In the heat treated samples, the indexing was poorer than in the base material, particularly in the intercritically heat treated samples, where non-indexed points were observed. Martensite is in this chapter identified not only by the GAIQ method, but also as the non-indexed points. The non-indexed points arise because diffraction conditions were too poor to index the Kikuchi pattern. It is acceptable to consider the non-indexed points as martensite, because martensite generally has poorly defined Kikuchi patterns as a consequence of the distorted lattice and dislocation content causing lattice strain (gradients) in martensite. In the EBSD measurement of TRIP base material and welded TRIP steel no non-indexed points were observed, and all martensite grains were indexed, albeit with lower IQ than ferrite. A possible reason for the occurrence of the non-indexed points in the heat treated samples could be a deliberate reduction of the camera resolution (i.e. binning was increased) during data acquisition to shorten the data collection time. Another explanation could be that the stress state in martensite formed during heat treatment is different from that in the base material. As was found in the Section 4.3.3, the amount of bainitic ferrite cannot be quantified with EBSD alone. This is because the KAM function only identifies the transition between ferrite and bainitic ferrite, and not the whole bainitic ferrite grain is included. Nevertheless, KAM is a very useful to locate the bainitic ferrite grains in the microstructure. The characterization of bainitic ferrite will be done in the next section concerning the heat treatments below Ac_1. The quantification of the amounts of ferrite, austenite and martensite is given in Fig. 5-11.

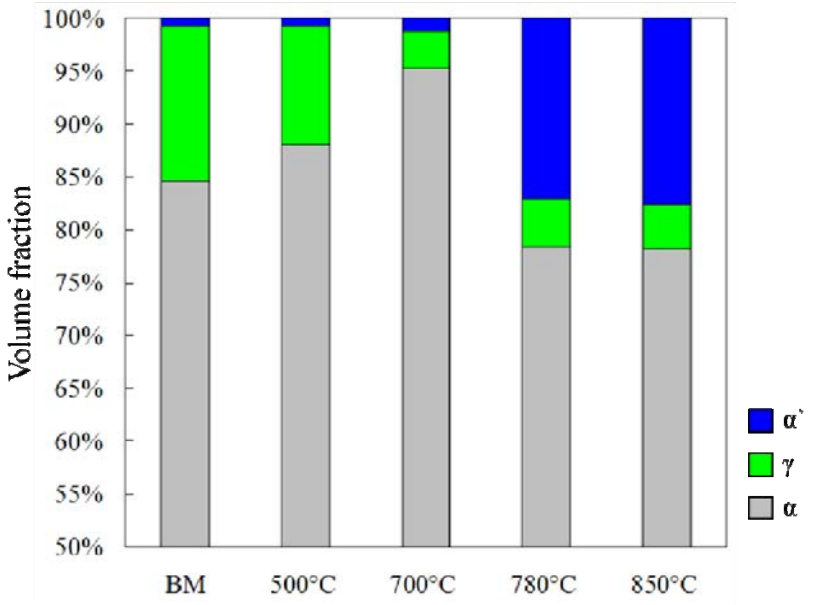

Fig. 5-11. Quantitative analysis of ferrite, austenite and martensite in the heat treated samples, in comparison with the BM. Note that the vertical axis has its beginning at 50% for a magnification of the minority phases.

The amounts of the phases will be discussed in comparison with EBSD maps of the microstructure in the sections 5.2.2 and 5.2.3. The quantitative analysis is performed on the full EBSD maps obtained in the heat treated samples, whereas the microstructure maps presented in the following are only sections of the full maps.

The results of the hardness measurements in the heat treated samples are given in Table 5-1.

Table 5-1. Hardness of BM and heat treated samples.

	BM	500°C	700°C	780°C	850°C
HV0.1	198	204	197	235	239
St dev.	4.3	6.1	6.6	5.0	11.1

5.2.2 Samples heat treated below Ac_1

IQ maps with colored martensite and austenite regions are shown in Fig. 5-12, in comparison with BM.

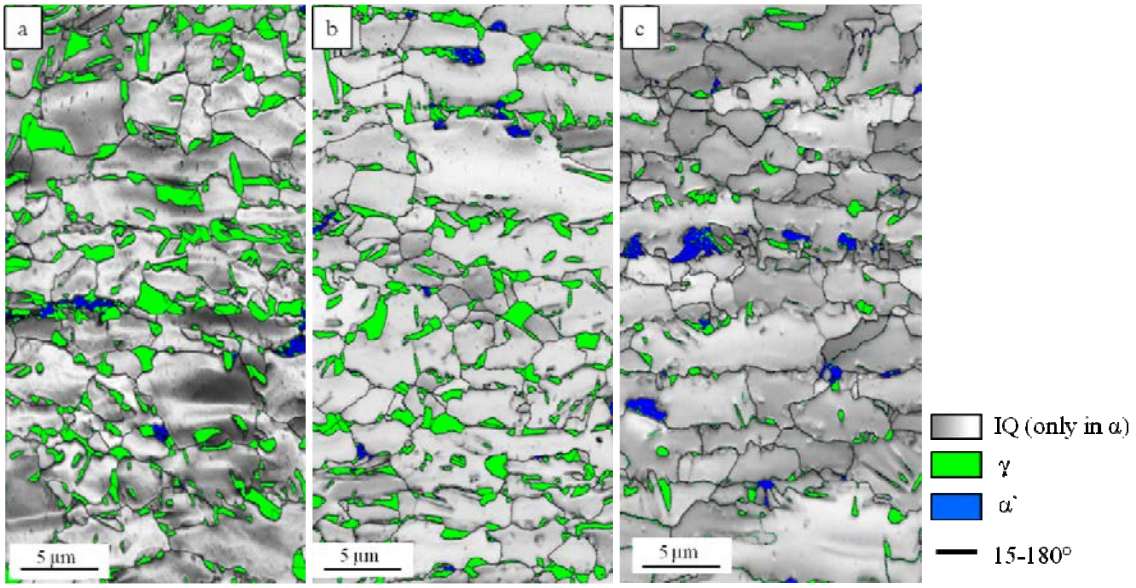

Fig. 5-12. IQ and phase maps of (a) BM and samples heat treated at (b) 500°C and (c) 700°C.

From the EBSD maps in Fig. 5-12 it is clearly seen that the amount of martensite is almost unchanged after heat treating at 500°C and 700°C in comparison with BM, which is consistent with the quantitative analysis in Fig. 5-11. In all three samples there are only few martensite grains. The unchanged martensite content after heat treatment below Ac_1 confirms that no extra martensite is formed at this temperature range. Perhaps martensite is tempered at both temperatures but this cannot be concluded on the basis of EBSD maps only.

The vol% of γ has decreased in both the 500°C and the 700°C sample (cf. Fig. 5-11 and Fig. 5-12), which is consistent with the expected transformation at these temperatures. The question is, which transformation products form at these two temperatures below Ac_1. On tempering TRIP steel at temperatures below Ac_1, the transformation product of austenite depends on the temperature and the composition. At lower temperatures, i.e. <450°C, bainite is expected as for the second heat treatment applied during processing of TRIP steel [7]. At 600-700°C the most likely transformation products are ferrite and/or pearlite (cf. Fig. 2-14). Further analysis of the EBSD maps is necessary to verify this. In Fig. 5-13 bainitic ferrite is also identified in the phase maps from Fig. 5-12, and also a quantification of the four micro-constituents is included.

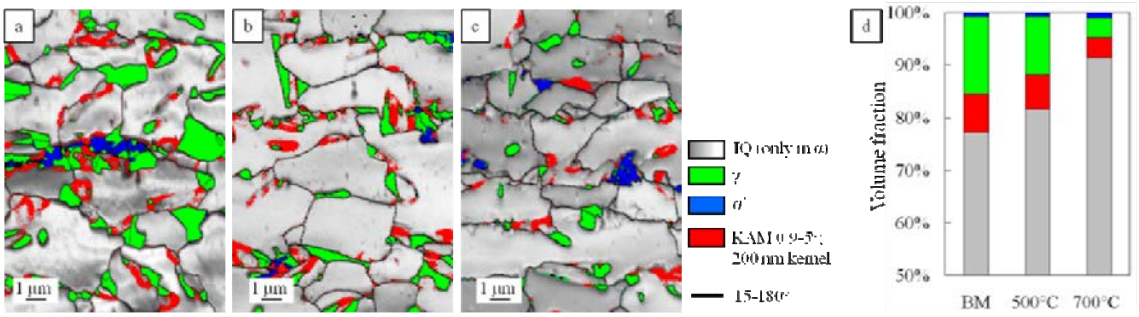

Fig. 5-13. Sections of phase maps from Fig. 5-11 including also bainitic ferrite in (a) BM and heat treated samples at (b) 500°C and (c) 700°C. Also a quantification is shown in the graph in (d). Bainitic ferrite is identified with the KAM function in the range of 0.9-5°, in a kernel of 200 nm.

It is known from the characterization of BM that martensite is also indexed with the KAM function. Therefore, martensite was indexed and removed from the maps before applying the KAM procedure to highlight bainitic ferrite.

It is observed in Fig. 5-13 that the vol% of α_B is slightly decreased at 500°C compared to the BM, albeit not significantly. This indicates that austenite is not continuing its transformation into bainite at 500°C. The α_B at 500°C was already present in the BM. In this respect it should be pointed out that the amount of α_B indexed by the KAM function is only indicative since it only highlights the transition between α and α_B. Nevertheless, from the microstructures in Fig. 5-13 (a,b) it is evident that there is no continuation of the bainite formation in the 500°C sample.

In the 700°C sample the vol% of α_B is further reduced compared to the 500°C sample (cf. Fig. 5-13). Also the γ vol% is significantly lower in the 700°C sample compared to 500°C. Based on these findings it is concluded that more austenite has transformed in the 700°C sample, but not into bainite.

Since the quantification of α_B is associated with uncertainty, the shape of the austenite grains can also be used as an indication of the presence of bainite. The growth of bainitic ferrite is associated with a change of the shape of the austenite grains, so that they become more elongated. Grain shape aspect ratio (GSAR) is a useful tool to evaluate the shape change of austenite grains. GSAR calculations were performed on the austenite grains in the EBSD maps from BM, 500°C and 700°C. Unfortunately, the results of the analysis were inconclusive, as no significant changes were observed between the maps. That is consistent with the above findings of no continued bainite formation in 500°C and 700°C samples.

Since it was found that no bainite formation occurs in the two heat treated samples below Ac_1, the transformation product is most likely ferrite and/or pearlite. The heat treatment time is very short, so if carbides have developed, they will be very small. Therefore it is most likely that ferrite has formed, possibly accompanied by carbide precipitation from those austenite grains

with relatively high carbon content. The presence of carbides was neither verified with EBSD analysis nor could SEM analysis indicate if carbides had formed.

The hardness in the samples heat treated below Ac_1 was found to be almost identical to that of the BM (Table 5-1). It indicates that the change in γ vol% observed in the two samples has not affected the hardness in the microstructure, and is consistent with no increase in the martensite content.

To sum up on the above findings for the two heat treated samples; it was found that a similar transformation behavior occurs at 500°C and 700°C. No bainite formation takes place, but, instead, austenite is transformed into other b.c.c. transformation products, most likely ferrite. For a continued bainite transformation, apparently the temperature has to be lower than 500°C. The difference between the 500°C and 700°C maps is the kinetics of austenite transformation, which is fastest at 700°C. The martensite content remains unchanged after both heat treatments.

5.2.3 Samples heat treated between Ac_1 and Ac_3

In Fig. 5-14 IQ and phase maps of the samples heat treated at 780°C and 850°C are compared with the BM.

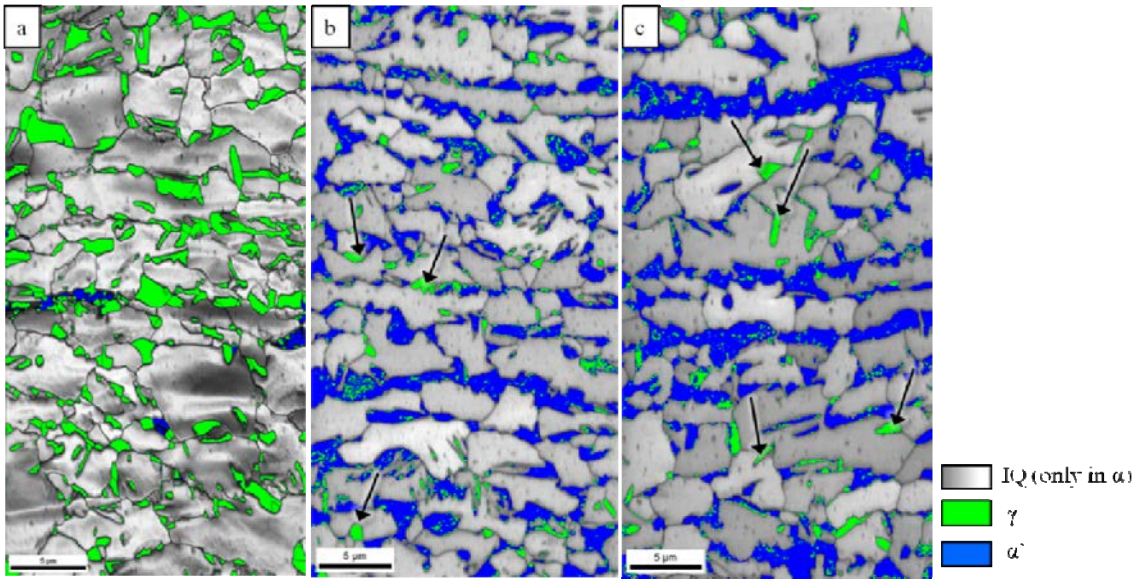

Fig. 5-14. IQ and phase maps of (a) BM and samples heat treated at (b) 780°C and (c) 850°C (c).

In both samples the α' vol% is increased significantly compared to the BM. This is caused by austenite formation in the intercritical temperature regime, which transforms into α' during cooling. The α' is preferentially formed in bands in the microstructure lying parallel to the rolling direction. The directionality is explained from the segregation of alloying elements; mainly segregation of the austenite stabilizing element Mn plays a role.

The vol% of martensite is almost identical in the samples heat treated at 780°C and 850°C, indicating that, for the short heating time (10 seconds), the temperature at which the heat treatment is performed is not significant for the amount of martensite formed. The hardness is comparable in the two samples (Table 5-1), which is consistent with equal amounts of α'.

There are still austenite grains present in the microstructure after 780°C and 850°C and these grains are mostly observed to be located away from the bands of martensite (indicated with arrows in Fig. 5-14). This may indicate that the observed retained austenite is a remnant from the BM and not austenite formed at 780°C and 850°C.

The presence of α_B was also investigated in the intercritically heat treated samples with the KAM function. Almost no α_B was identified, which confirms that bainite formation does not continue above Ac_1. The absence of α_B in these two samples indicates that the α_B present in the BM before heat treatment has disappeared. This may have been caused by the formation of martensite, which has consumed the bainite.

5.2.4 Investigation of ferrite grains after heat treatments

The ferrite grains in the microstructure were also investigated after the heat treatments, to verify whether their orientation has changed. Fig. 5-15 shows inverse pole figure (IPF) colored maps of ferrite in all heat treated samples and in the BM.

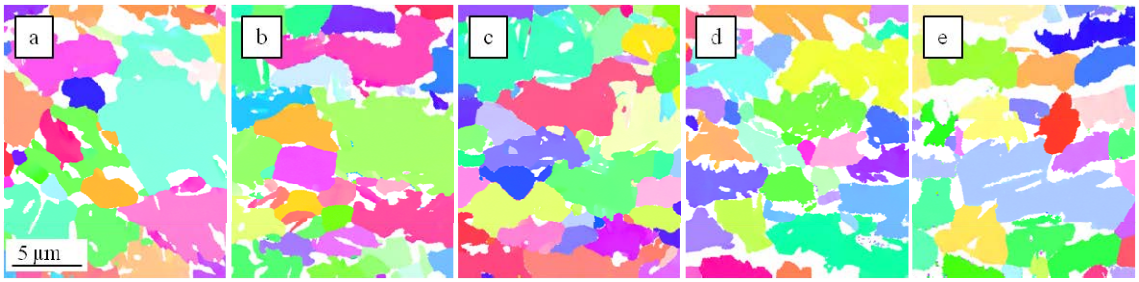

Fig. 5-15. IPF coloring of ferrite in (a) BM, and the samples heat treated at (b) 500°C, (c) 700°C, (d) 780°C and (e) 850°C.

It is clear from the maps that all ferrite grains have a homogenous orientation color within a single grain, indicating that no rotation occurred in the ferrite grains at any of the chosen temperatures.

For deeper investigation of a possible rotation of the ferrite grains, misorientation profiles were made on the ferrite grains in the IPF maps in Fig. 5-15. Misorientation lines were drawn in ferrite grains, parallel with RD. The maximum misorientation difference from origin to end of the misorientation line was 0.1°/µm, which is very small. This was found for all the maps and grains presented in Fig. 5-15.

5.2.5 Correlation between heat treatments and weld characterization

At 500°C and 700°C the bainite transformation is not continued and instead ferrite is formed. No carbides were identified, so if carbides are formed, they are smaller than the resolution limit of EBSD and SEM.

After heating to 780/850°C the microstructure attained a sheer dual-phase morphology, containing ferrite and martensite. The amount of martensite does not differ significantly at the two temperatures. In addition, some austenite grains remain, which indicates that a pure thermal influence will not cause full transformation of all austenite grains.

The orientation difference along RD in the ferrite grains is measured to 0.1°/µm after the heat treatments. This leads to the conclusion that if larger rotations are observed, it should have its origin in deformation and not in heat treatment. This is particularly important knowledge, which can be used for understanding microstructure changes in the welded samples.

6 Evaluation of all welded samples

6.1 Lap shear tensile strength

The strength of the welds was examined by lap shear tensile tests; the results for the 1st generation are shown in Fig. 6-1.

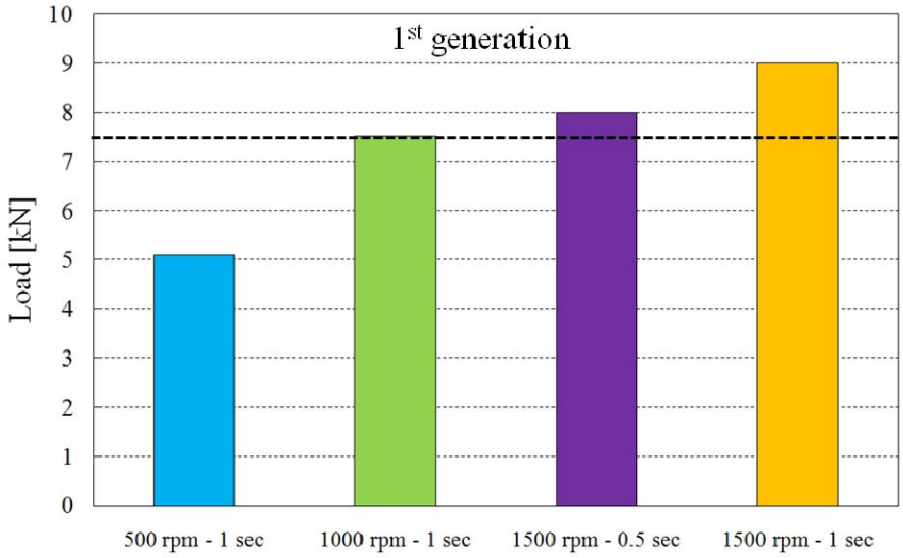

Fig. 6-1. Lap shear tensile strength of the 1st generation welds. The dashed line indicates the minimum lap shear strength specified by American Welding Society (AWS) [36]. The colors are applied for an easier comparison with Fig. 6-4 and Fig. 6-5.

It is clear from Fig. 6-1 that by increasing the rotation speed, the strength is increased. Also the increase in dwell time from 0.5 sec to 1 sec at 1500 rpm induces an increased strength. The dashed line in the figure indicates the minimum required strength of automotive spot welds given by American Welding Society (AWS) [36]. It is evident that samples with a rotation speed above 1000 rpm meet the requirements.

The lap shear tensile strength of the 2nd generation welds is presented in the graph in Fig. 6-2.

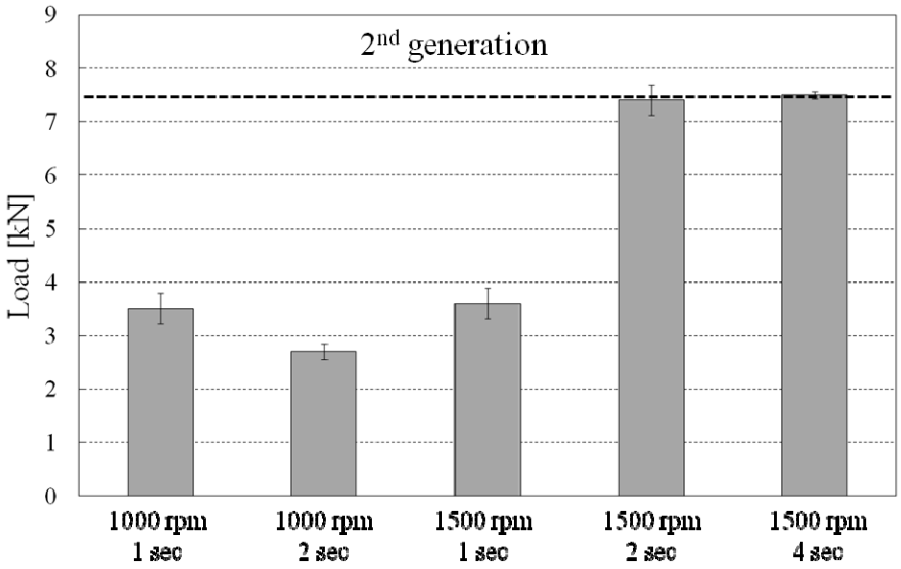

Fig. 6-2. Lap shear tensile strength of the 2nd generation welds. The dashed line indicates the minimum lap shear strength specified by AWS [36].

It is seen for the 1000 rpm samples that by increasing the dwell time the strength is reduced while for the 1500 rpm samples a pronounced increase in strength is observed. This discrepancy is most likely related to the plunge depth, which varied significantly. A detailed explanation will be given in the next section. For the 1500 rpm samples, it can be seen in Fig. 6-2 that by increasing the dwell time from 1 to 2 seconds a remarkably increase in strength is obtained; no change is observed when the dwell time is prolonged from 2 to 4 seconds. This suggests that an optimal dwell time occurs, above which no effect of dwell time on strength is observed. For 1500 rpm the optimum dwell time is between 1 and 2 seconds.

The samples “1000-1” and “1500-1” were welded in both generations, but the strength of the welds in the 2nd generation did not reach the same high level as in the 1st generation. For instance, the strength of “1500-1” is 9 kN, while the strength of “1500-1-2nd“ is only 3.6 kN. It indicates poor repeatability of the welding technique, in general, but there is a reasonable explanation to the difference between the two generations; the plunge depth.

6.2 Effect of varying plunge depths

As indicated in the descriptions above, the plunge depth varies significantly for some of the welds. Particularly, the 2nd generation welds suffered from a strong variation in plunge depth. In Fig. 6-3 cross sections of selected samples with measured plunge depths are shown.

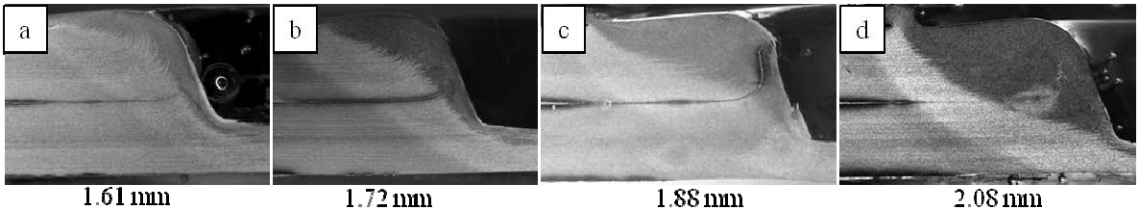

Fig. 6-3. Cross sections of sample 1500-1-2nd (a), 1500-1-1st (b) and 1500-2-2nd (c+d) with the measured plunge depths indicated below the micrographs.

The cross sections in a) and b) are welded with the same welding parameters, and this is also the case for c) and d). It is clear that the width of the welded region differs significantly, despite the use of similar welding parameters. The variation in the plunge depth is the responsible parameter for these deviations.

The welding machine employed in the present study was position controlled and not force controlled. Consequently, a repeatable and exact plunge depth is difficult to obtain, which leads to a large variation of the plunge depths. It is recommended to use force controlled welding machines in order to obtain repeatable welds. For the distance controlled welding machines, it is important to use proper clamping of the sheets before welding, but there is still a risk of varying plunge depths. The sample size of the 2nd generation welds were unintentionally performed on sheets with only half the width of the 1st generation welds. This may have led to poorer conditions for clamping of the samples during welding, which may explain the difference between 1st and 2nd generation regarding the plunge depths.

The conclusion to the above discussion regarding the plunge depth is that the 1st generation welds were the most reliable due to the comparable plunge depths. To support this, the plunge depths of the 1st generation welds are given in Table 6-1.

Table 6-1. Depth of tool measured from original sheet surface to bottom of pin hole.

	500-1	1000-1	1500-0.5	1500-1
Depth of tool	1.70 mm	1.70 mm	1.75 mm	1.72 mm

The depth was measured from the bottom of the pin hole to the original surface of the upper sheet. It is observed that the variation within the generation is relatively small (1.70-1.75 mm) as compared to the variations observed in Fig. 6-3 (1.61-2.08 mm). As a consequence of the comparable plunge depths and consistent lap shear strength (Fig. 6-1), the 1st generation welds were selected for detailed investigation of hardness distribution and microstructure.

6.3 Cross sections

Cross sections of the 1st generation welds are shown in Fig. 6-4.

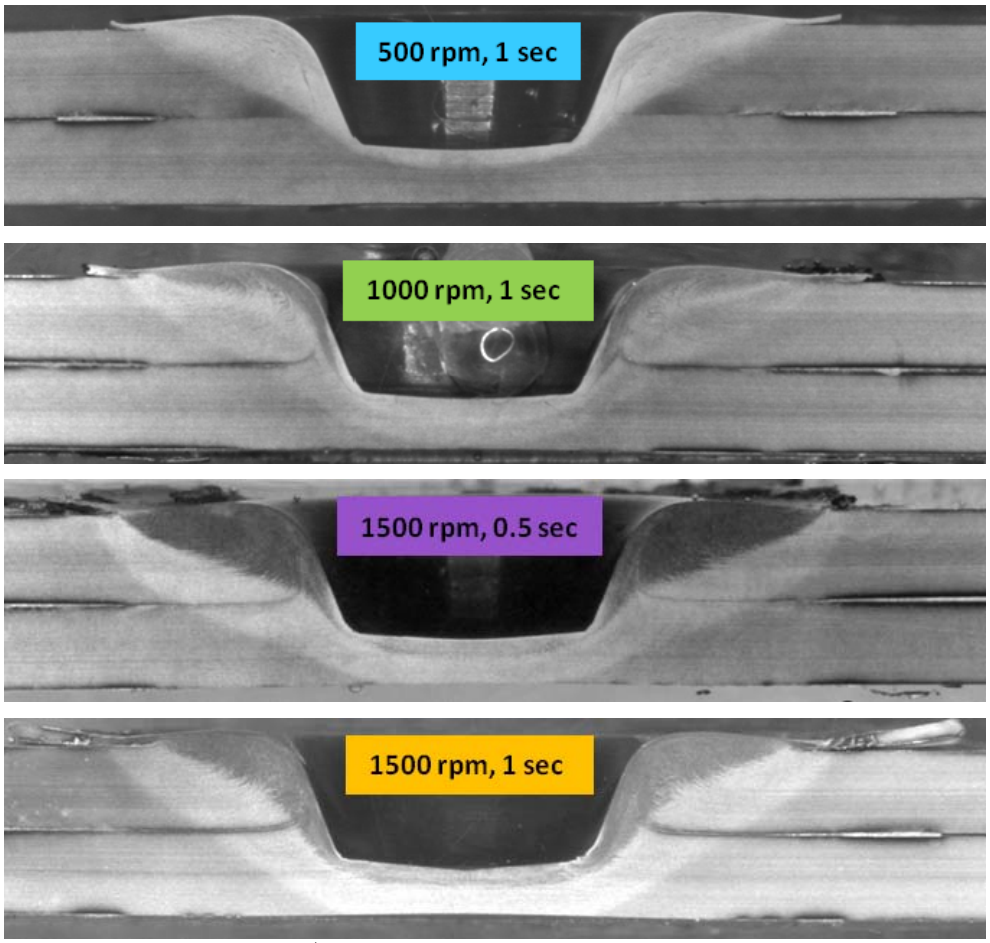

Fig. 6-4. RLM images of the 1st generation welds. Etched with Nital.

Immediate observations of the samples indicate that there is a clear difference in microstructure between “500-1” and the other three samples. In “500-1” the weld contains only a bright region,

whereas the other samples contain two regions in the weld; a dark zone close to the pin hole, and a bright zone next to this dark zone. This coincides with a strength of "500-1", which is far below the strength of the other samples (cf. Fig. 6-1).

Another observation from Fig. 6-4 is the remarkable difference between 1000 rpm and 1500 rpm; the dark close to the pin hole is largest after 1500 rpm. This indicates that a large dark zone and high strength are correlated. The difference in dwell time between "1500-0.5" and "1500-1" is not significant but the dark zone is slightly larger in "1500-0.5" than in "1500-1", which appears inconsistent with the higher strength of "1500-1". Again, the plunge depth could be responsible for the deviating behavior. It is observed in Table 6-1, that the tool is plunged slightly deeper into "1500-0.5" than into "1500-1" (as well as "500-1" and "1000-1"), which may explain the deviation in the width of the dark zone closest to the pin hole, as observed in Fig. 6-4.

6.4 Hardness profiles

Hardness measurements were performed along profiles over the welded zones and are shown in Fig. 6-5 for the 1st generation samples.

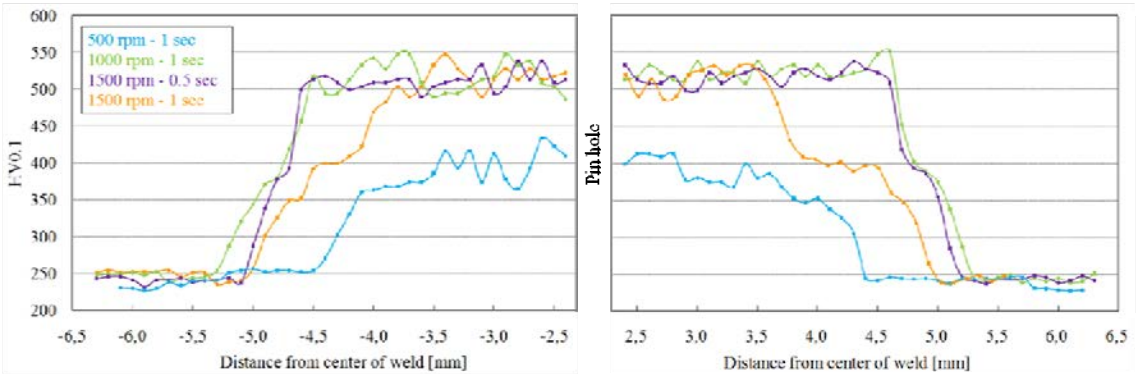

Fig. 6-5. Hardness profiles over the welded region in the 1st generation samples.

It is observed that "500-1" deviates significantly from the three other samples by not reaching the same hardness in the weld region closest to the pin hole. Furthermore, the width of the region with increased hardness is much narrower in sample "500-1" as compared to the others. These differences are consistent with the cross section (Fig. 6-4) and the tensile strength (Fig. 6-1) of "500-1", which were also found to deviate from the other samples.

Another observation from the hardness profiles in Fig. 6-5 is that “1500-1” has a plateau at the same hardness value as maximally attained in “500-1”. This leads to more gradual transition between low and high hardness. A tendency towards such a plateau is also observed in “1000-1” and “1500-0.5” albeit to a much lesser extent.

6.5 Bonding ligament width

The strength of the weld emanates from the region where the two sheets are joined, which is commonly known as the bonding ligament width or the bonding interface region [43][47][40]. There is no standardized method for measuring the bonding ligament width. A method often applied is to draw a line parallel to the sheets, as shown in Fig. 6-6.

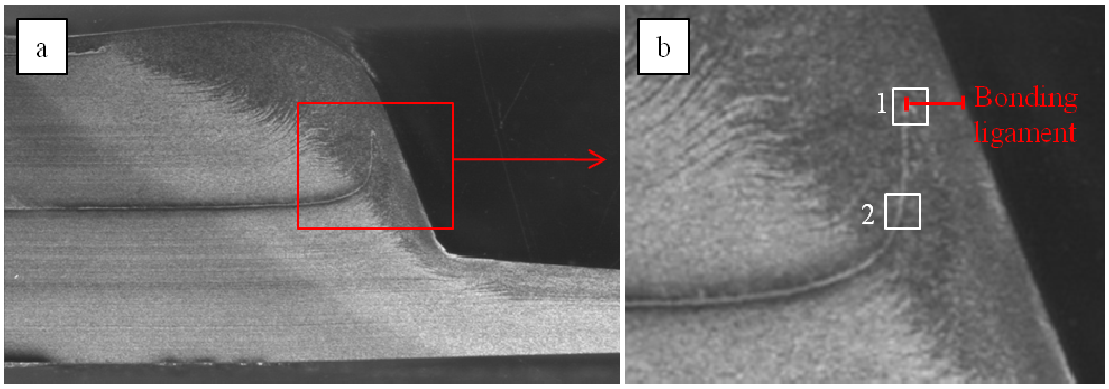

Fig. 6-6. Location of the bonding ligament width. Numbers 1 and 2 refers to the SEM images in Fig. 6-7.

The interface between the two sheets was investigated with SEM; micrographs of this investigation are shown in Fig. 6-7.

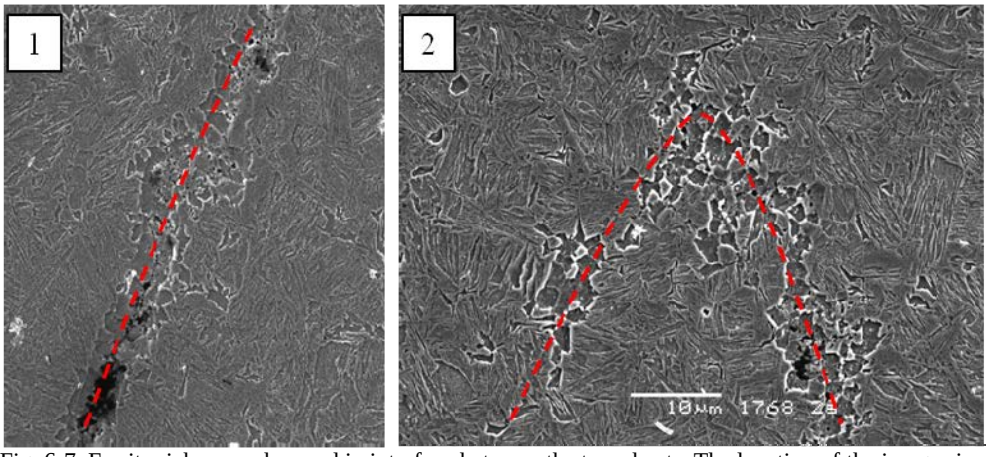

Fig. 6-7. Ferrite rich zone observed in interface between the two sheets. The location of the images is indicated in Fig. 6-6. The red, dashed lines indicate the original interface between the sheets.

The micrograph in Fig. 6-7 (1) shows a part of the interface, where porosities appear, which indicate insufficient joining of the sheets. The micrograph in Fig. 6-7 2) shows a region in the interface, that does not contain porosity and only ferrite grains. The original interface between the sheets is marked with red dashed lines. The ferrite grains were analyzed with EDX to verify whether they contain Zn. The source of Zn is the galvanized coating, which was not removed before welding. Zn is known to be a ferrite stabilizer [142]. The EDX measurement shows that there is a content of Zn in the ferrite grains, which suggests that the ferrite grains are stabilized by Zn. The evaporation of Zn during welding may contribute to the development of the porosities, which were observed in Fig. 6-7 (1).

The micrograph in Fig. 6-7 (2) is the last remaining trace of the original interface. Approaching the pin hole from this location, the original interface between the sheets cannot be recognized. This is where the bonding ligament is starts. The bonding ligament width was measured for all 1st generation samples, and the measured widths are listed in Table 6-2.

Table 6-2. Bonding ligament width measured in the 1st generation welds.

	500-1	1000-1	1500-0.5	1500-1
Bonding ligament width	285 µm	130 µm	220 µm	175 µm
Shear tensile strength	5.1 kN	7.5 kN	8.0 kN	9.0 kN

No correlation is observed between the bonding ligament width and the strength of the weld. This is particularly evident for sample 500-1, which has the lowest strength and the widest bonding ligament. It indicates that not only the bonding ligament width is responsible for the strength, but also the type of microstructure developed in the bonding ligament. Therefore, a

microstructure investigation is necessary to explain a correlation between the microstructure and the strength of the welds.

6.6 Material flow during welding

The material flow during welding can be delineated from the alignment of the microstructure, in comparison with predictions from literature. Sample 1500-1 was selected for investigation of the material flow; In Fig. 6-8 the cross section of Sample 1500-1 is compared with the predicted material flow for FSSW (cf. Fig. 2-9) [67].

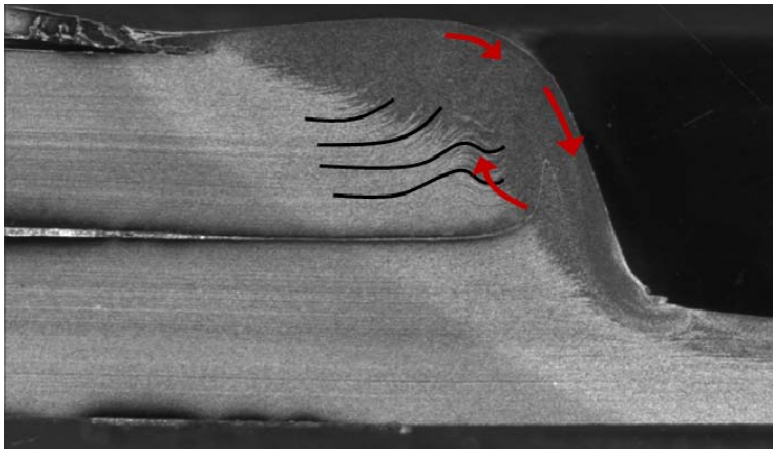

Fig. 6-8. Sample 1500-1 as an example to illustrate the material flow during welding. The black lines indicate the alignment of the microstructure, whereas the red arrows are the predicted flow during FSSW reported from [67].

The black lines indicate the alignment of the microstructure in Sample 1500-1, and the alignment is more or less similar for all samples. The red arrows indicate the directions, by which the microstructure flows during FSSW, as reported in [67]. It is obvious that the flow according to the red arrows is capable of causing the alignment of the microstructure in the samples.

6.7 Observed defects in welds

For the 2nd generation welds, not only the plunge depth was observed to vary. Frequently, defects were observed on the cross section micrographs. In Fig. 6-9 cross sections of two selected samples from the 2nd generation are shown.

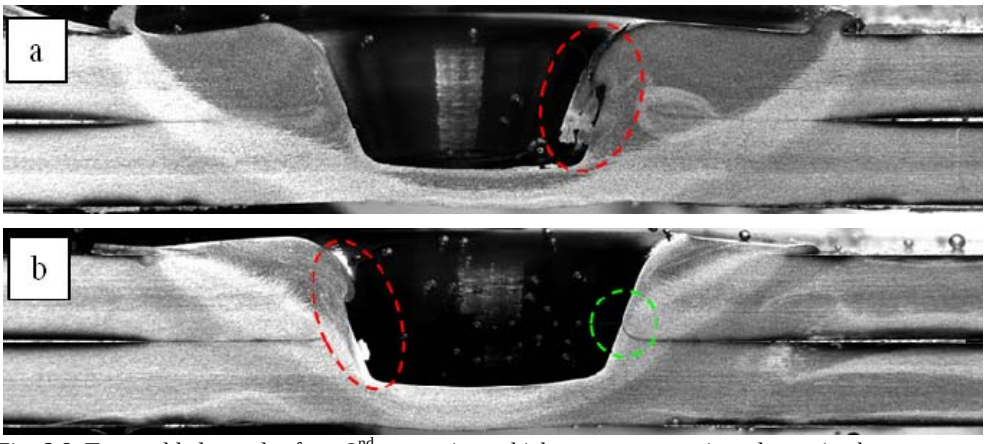

Fig. 6-9. Two welded samples from 2nd generation, which were asymmetric and contained excess material in the pin hole. Sample 1500-1-2nd (a) and sample 1000-2-2nd (b).

It is observed that excess material is located inside the pin hole (red ellipses). It is unexpected that material would be left in the pin hole since the pin is retracted during rotation, which should result in a smooth surface on the inside of the pin hole. In Fig. 6-9 b) an asymmetric appearance of the welded region is observed on comparing the left and right side. The FSSW process is expected to be symmetric because of the numerous rotations of the tool during welding. The asymmetric appearance in Fig. 6-9 b) has apparently lead to poor bonding on the right-hand side of the weld (green ellipse), which is very critical for the weld. The excess material in Fig. 6-9 a) has not lead to poor bonding but is only causing a visual defect of the weld. This is certainly not desirable because inhomogeneous spot welds are unwanted in the automotive industry.

The above described defects were only observed in the samples of the 2nd generation. Various causes could be put forward for this anomaly: i) the tool was destroyed, or ii) the tool had excess material sticking onto the pin/shoulder after initial welds, iii) the sheets were not mounted correctly, or iv) operator dependent causes. The exact causes are impossible to elucidate.

It confirms the better quality of 1st generation welds.

6.8 Conclusion

1st generation

- Higher rotation speed gives stronger weld.
- Nothing can be concluded on dwell time since plunge depth varies in the two samples with different dwell time.
- Plunge depth appears to be a dominant parameter.

2nd generation

- Higher rotation speed gives stronger welds.
- Higher dwell time gives stronger welds but this is not a very strong dependence.
- Plunge depth varies a lot for the various samples, which obscures the correlation between welding parameters, strength and width of welding zones.
- Asymmetry is observed in some samples, which is remarkable because welds are expected to be symmetric. The cause is impossible to retrace.

The 1st and 2nd generation welds were not comparable, because the 2nd generation welds suffered from large variations in the plunge depth. The plunge depth obviously is difficult to control or reproduce on a distance-controlled welding machine. Also the 1st generation samples suffered from some variation of the plunge depths, which caused uncertainties between weld parameters and the outcome. In the present study, welding was carried out by the industry partner and without influence from the author, with which the quality of the welds were out of command of the author. Therefore, a discussion of the influence of the weld parameters onto the weld quality is restricted. Instead, focus will be pointed towards understanding the microstructure changes occurring during the welding process. For this, one representative sample was selected from the 1st generation. Immediate investigations of the 1st generation welds indicated the presence of comparable zones in three samples; 1000-1, 1500-0.5 and 1500-1. Sample 1500-1 was achieved the highest lap-shear strength, why it was selected for a detailed study.

7 Microstructure evolution in Sample 1500-1

7.1 Identification of zones

The cross section of Sample 1500-1 is shown in Fig. 7-1 with indications of the identified zones (numbers 1-4) and corresponding EBSD maps for each of the zones in the weld.

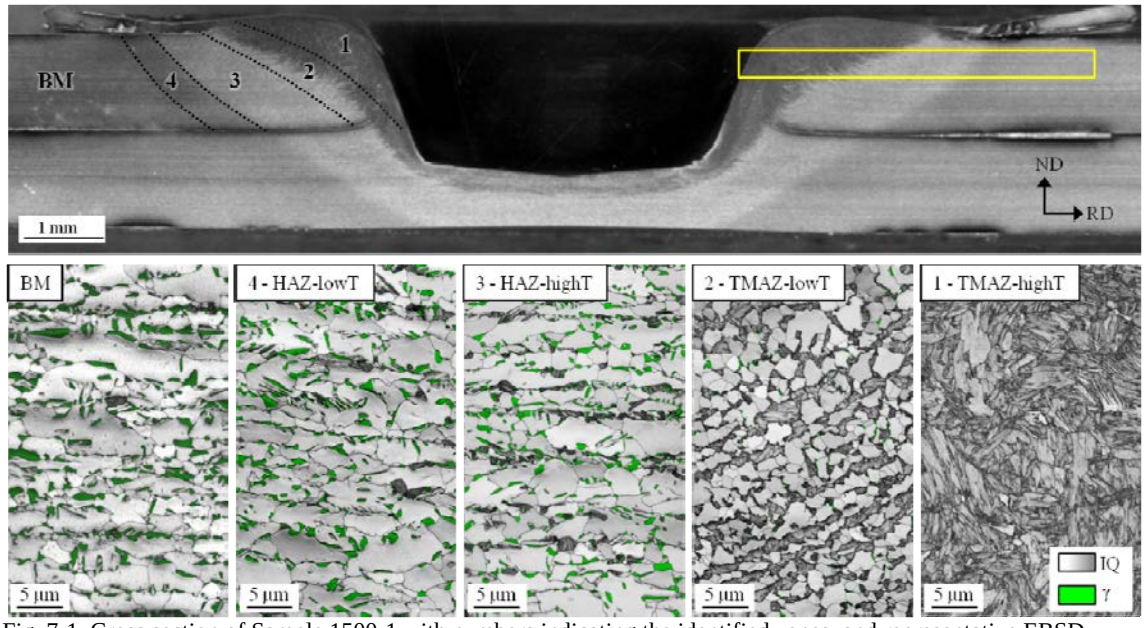

Fig. 7-1. Cross section of Sample 1500-1 with numbers indicating the identified zones, and representative EBSD maps of the zones. The yellow box indicates where characterization of zones has been carried out.

The location of the four identified zones is marked with numbers in the RLM image. The contrast of zone 4 is difficult to see on the RLM image, but microstructure and hardness investigations indicated that it is a separate zone. The identification of the four zones is based on a detailed microstructure characterization, which will be thoroughly described in the following sections. The zones are just mentioned here as an introduction and the chapter is subdivided in sections in accordance with the various zones.

The results presented in the following will show that there exists two TMAZs and two HAZs; each in their temperature interval. Due to the different temperature ranges in the zones, the terminology used for the four zones will refer to the temperature, high or low. The four zones are:

- Zone 1: TMAZ-highT
- Zone 2: TMAZ-lowT
- Zone 3: HAZ-highT
- Zone 4: HAZ-lowT

The characterization of the zones is performed in the region marked with a yellow box in Fig. 7-1, which involves various characterization techniques, including hardness measurements, EBSD, RLM, SEM, and XRD characterization.

The hardness measured along a line covering all zones is given in Fig. 7-2. EBSD maps were obtained in along a similar line (not the same sample) as the hardness measurements, and for each EBSD map the area fraction (area%) of α’ and γ were determined. Therefore, all points on the area% curves in Fig. 7-2; corresponds to an EBSD map.

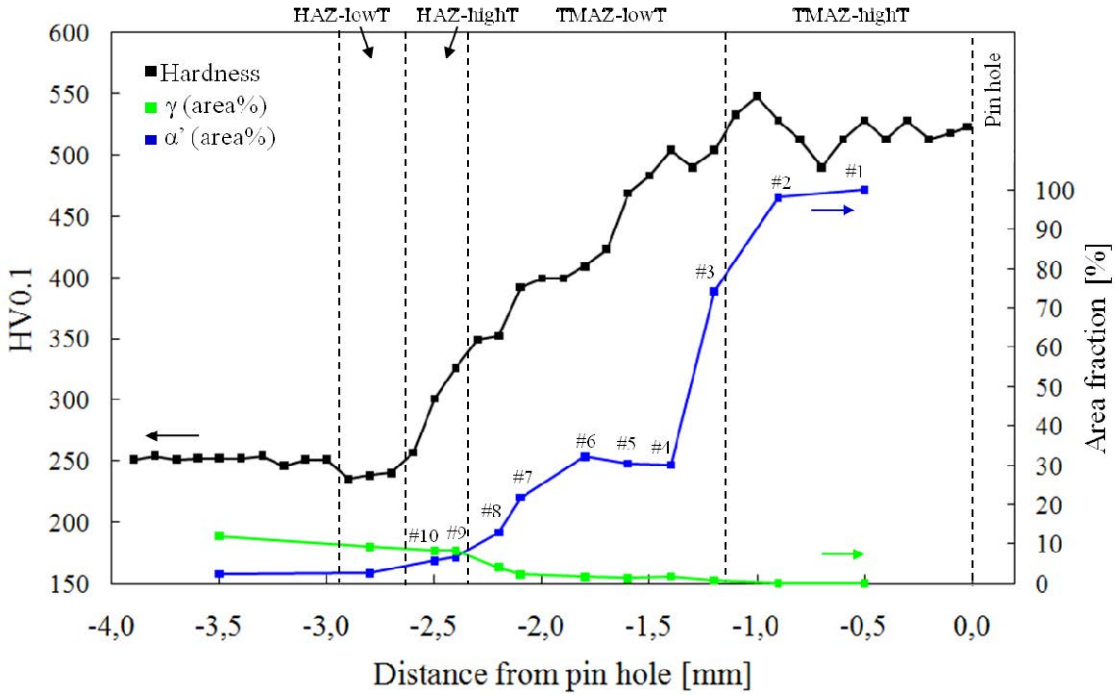

Fig. 7-2. Hardness profile of the entire weld, in comparison with area% of γ and α'.

The area% of γ corresponds to the f.c.c. phase fraction in the maps, while the α' area% is determined after the GAIQ method, which was described in section 4.3.3.

The identified weld zones are marked in the graph and thorough investigations of the curves will be included in the following sections. In the zones containing more than one EBSD map, the maps are numbered in Fig. 7-2 (along the α' area% curve), and the numbers will be used in the following evaluations of the EBSD maps.

Modeling of the thermal behavior during welding was performed. The results are enclosed in Appendix 1. In the present study, a useful prediction from the model is the peak temperature, which was estimated at 1100°C near the pin hole. This result will be used to support the discussion in this chapter.

7.2 HAZ-lowT

It is observed from Fig. 7-2 that the hardness decreases slightly in the HAZ-lowT as compared to the BM. The α' area% is unchanged, thus this is not the cause for the decreased hardness. The γ area%, on the other hand, is decreased as compared to BM. It is known that the carbon content is higher in γ than in α, and the hardness is also highest in γ [23]. As a result, the hardness decrease in this zone should be related to the decrease of the γ area%. The decrease of γ area% in the HAZ-lowT indicates that the temperature was below Ac_1 during welding. A temperature

below Ac_1 may also induce tempering of the α', which is present in the BM before welding; this will lead to decreased hardness as well [1].

Further microstructure characterization will contribute to investigate the transformations, which occurred at the temperature. SEM micrographs of HAZ-lowT and BM are shown in Fig. 7-3.

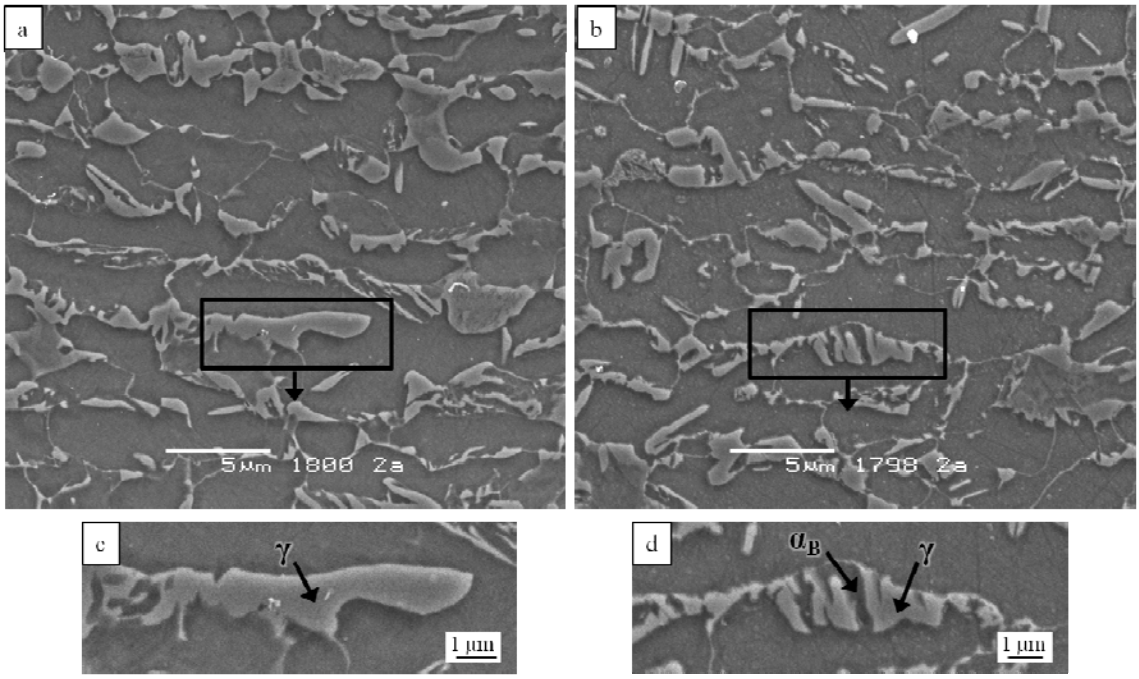

Fig. 7-3. SEM micrographs of BM (a+c) and HAZ-lowT (b+d).

Observing only Fig. 7-3 (a) and (b), it is difficult to identify a difference but the magnified images in Fig. 7-3 (c) and (d) clarify that the morphology of γ grains has changed in the HAZ-lowT as compared to BM. The explanation for the changed morphology is that bainitic ferrite has developed as lamellar grains, that grow into the austenite grains, which in combination form bainite in TRIP steel. When bainitic ferrite is formed, carbon is accumulated into the neighboring γ lamellae, thereby enriching the remaining γ lamellae with carbon. The same mechanism occurs in the processing heat treatment of TRIP steels to produce bainite. Bainite formation in TRIP steels is commonly achieved at a temperature in the range of 375-450°C [7]. Hence, it can be concluded that the temperature was in this interval in the position in HAZ-lowT, where the SEM micrographs in Fig. 7-3 (b) and (d) are from.

The presence of bainitic ferrite can be confirmed by the KAM function in EBSD. Fig. 7-4 shows EBSD maps of BM and HAZ-lowT.

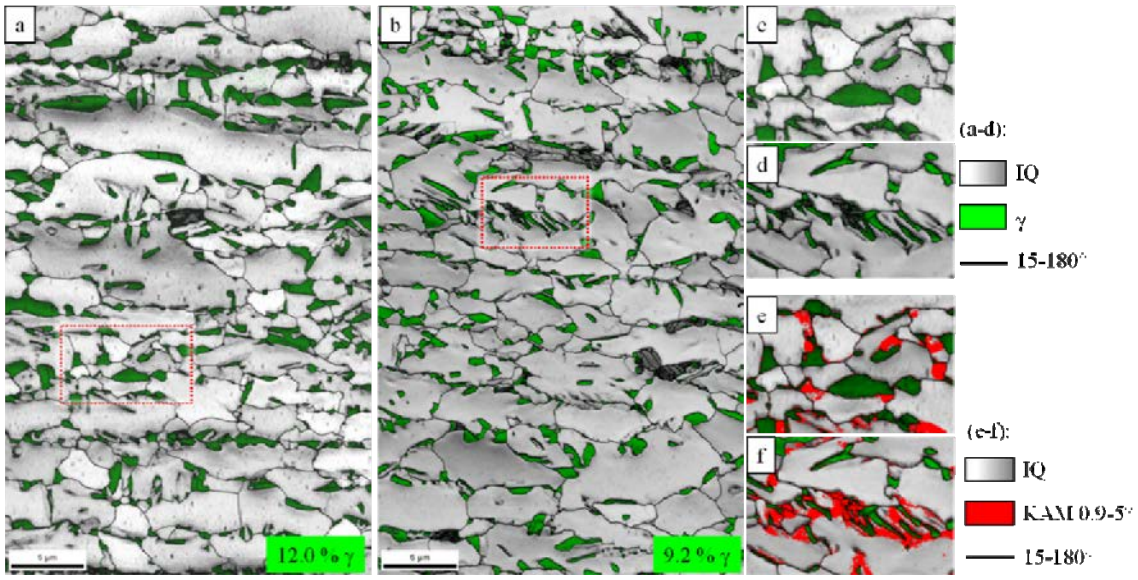

Fig. 7-4. IQ maps of BM (a,c,e) and HAZ-lowT (b,d,f). In e) and f) the α_B is identified with KAM in the range 0.9-5°.

It is clear from the EBSD maps, that the location of α_B coincides with the γ lamellae in the HAZ-lowT, which corroborates that the transformation product of γ is bainite, as a combined structure of α_B and carbon-rich γ. The shape and size of γ was also investigated with EBSD. First, in Fig. 7-5 the grain size of γ in BM and HAZ-lowT is shown. The colors in the graph (c) correspond to the colors in the EBSD maps (a+b).

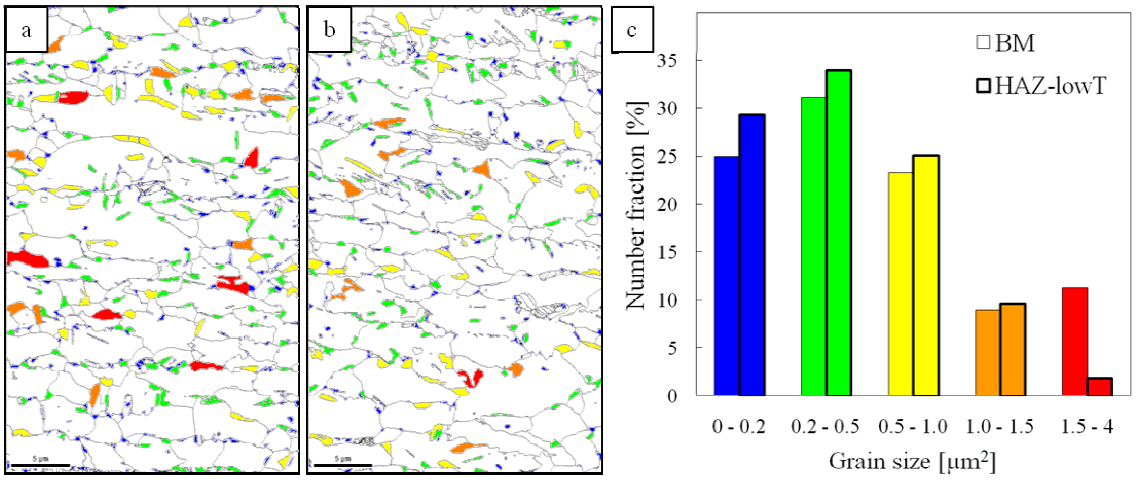

Fig. 7-5. Grain size of austenite in BM (a) and HAZ-lowT (b), and a graph (c) illustrating the number fraction of each grain size in a) and b).

It is observed that the γ grain size is smallest in HAZ-lowT, which indicates the growth of more small size γ grains in HAZ-lowT from the large grains in the BM. The shape of the γ grains was

investigated with the EBSD function GSAR. In the graph in Fig. 7-6 the distribution of the γ grains is shown, as a function of their elongation.

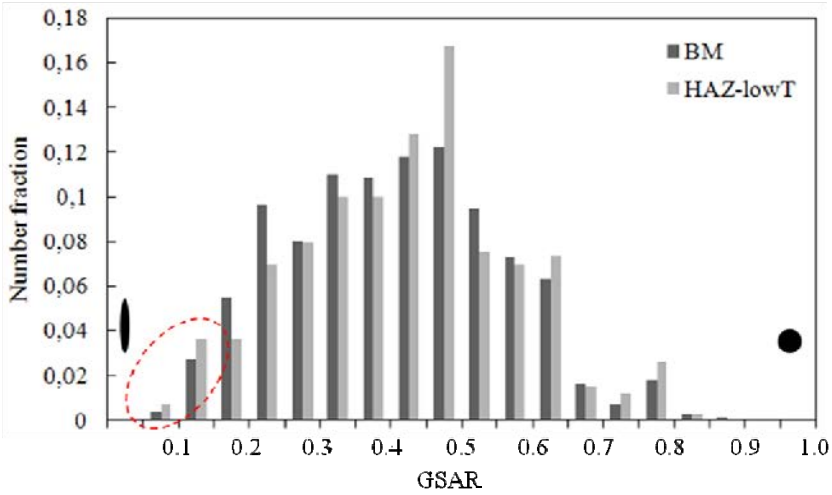

Fig. 7-6. GSAR analysis of austenite grains in EBSD maps of HAZ-lowT and BM.

The number fraction of very elongated grains having a GSAR < 0.15 is slightly increased in the HAZ-lowT zone as compared to BM (see the red ellipse in the graph). The remaining range of GSAR values is randomly dominated by the two zones, with no systematic difference. There is a large scattering in the results of the GSAR analysis, which indicates an uncertainty of the results. Therefore, the GSAR analysis cannot be used to confirm whether the austenite grains in the HAZ-lowT are more elongated than in the BM. Only the morphology investigations with SEM (Fig. 7-3) and EBSD (Fig. 7-4) confirm the presence of bainitic ferrite in HAZ-lowT.

It should be pointed out that only one EBSD map was obtained in the HAZ-lowT. The exact location of the EBSD map is seen in Fig. 7-2 (2.8 mm from the pin hole), and it is evident that the location is in the middle of the HAZ-lowT. Therefore, it can be concluded that the temperature where the EBSD map was obtained was in the range of 375-450°C [7]. In the characterization of the heat treated samples (Section 5.2) it was found that after exposing TRIP steel to 500 and 700°C, ferrite is the major phase formed. Therefore, approaching the HAZ-highT zone from the location of the EBSD map in HAZ-lowT will cause formation of ferrite. Accordingly, towards BM, bainitic ferrite will form. The lower limit of the HAZ-lowT is taken as 300°C, since it is known that no detectable differences occur in the microstructure below this temperature [21][78].

7.3 Transition from HAZ-lowT to HAZ-highT

The transition from HAZ-lowT to HAZ-highT occurs with an increase in α' area% and increased hardness, (Fig. 7-2). It was found from the characterization of HAZ-lowT that the upper limit of HAZ-lowT is the Ac_1 temperature. Above Ac_1, α and γ coexist, and part of the microstructure is transformed into γ, which upon cooling becomes transformed into α'. Therefore, a temperature above Ac_1 is associated with the formation of α', and this constitutes the transition between the two HAZs.

7.4 HAZ-highT

The α' area% increases on approaching the pin hole, which is seen in Fig. 7-2, and correspondingly the hardness increases. The γ area% is almost similar in the HAZ-highT zone as compared to the HAZ-lowT zone.

The microstructure in HAZ-highT is shown in the IQ and phase map (Fig. 7-7), in which the martensite has been identified by the GAIQ function (Section 4.3.3).

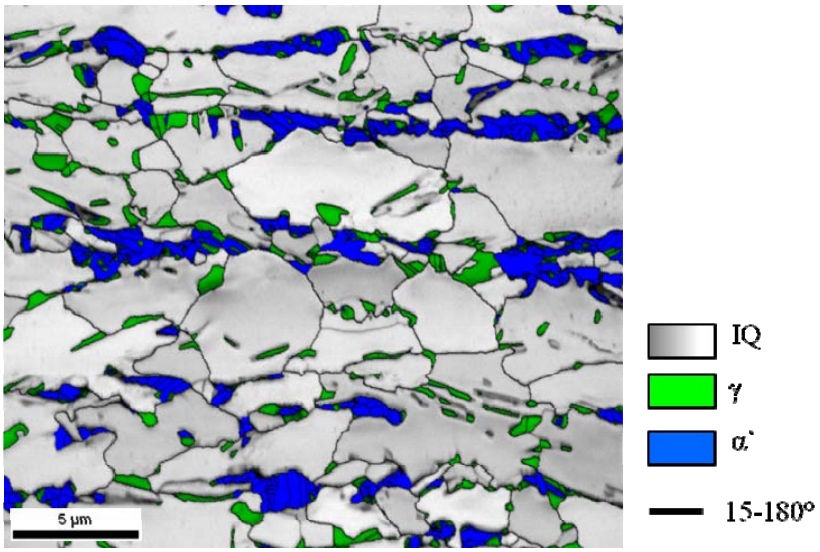

Fig. 7-7. EBSD map of the microstructure in HAZ-highT.

The α' grains are formed in bands, comparable to the location of γ grains in the BM. In the BM the band formation of the γ grains occurs during processing, as a result of segregation of austenite stabilizing elements. When the microstructure is exposed to an intercritical temperature, which is the case in the HAZ-highT, it is expected that γ will continue its growth from the pre-existing γ grains and the presence of γ stabilizing elements. The carbon content in

the newly formed part of the γ grain is determined by the carbon content in the α grain, it develops from. Increasing time and temperature, carbon will diffuse away from the carbon-rich part of γ into the new carbon-poor part. Upon cooling, the part of the γ grain, which is insufficiently stabilized with carbon, is transformed into α'. This explains why α' is formed along bands in Fig. 7-7, and it also explains the presence of γ adjacent to α'.

The γ-to-α' transformation is associated with a volume expansion and the neighboring α grains may be affected from this. The effect onto the α grains is investigated in Fig. 7-8 by the use of misorientation lines, which calculate the misorientation from point-to-origin along the line. It should be pointed out that the analysis was performed on the entire area, where EBSD was measured, and the results presented in Fig. 7-8 is consistent with the entire microstructure in this region and serves as an example.

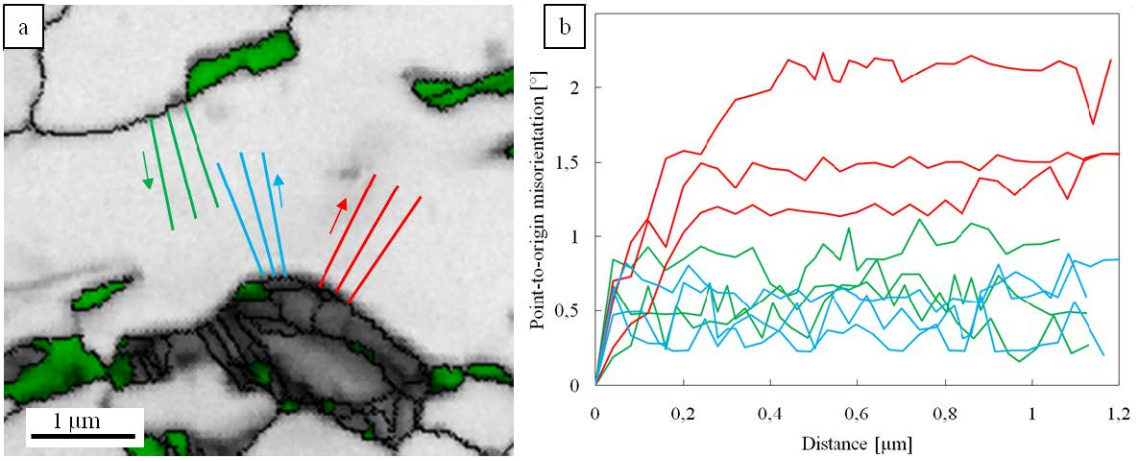

Fig. 7-8. Misorientation of α adjacent to α' (blue and red lines) and to α (green lines), measured from point to origin. The arrows in (a) indicate the direction, by which the misorientation lines are drawn.

It is observed that there is a significantly larger misorientation in the beginning of the red curves compared to the blue and the green curves, which indicates that α' has a larger influence on neighboring α. The red and the blue curves were both drawn adjacent to α', and it is clear that the effect of α' is direction dependent, since the misorientation is only significant along the red curves. The largest misorientation occurs in the first 200 nm of the ferrite grain, which is seen from the red curves, and it indicates that the α lattice is rotated over a distance of approximately 200 nm from neighboring α'. It can therefore be concluded that the volume expansion of α' affects α in the nearest 200 nm and the effect is more widespread in certain directions. The directions from α', which are not causing much effect, have a comparable effect as if α is the neighbor, which is considered within the angular accuracy of the method (0.5°) [143]. In [144] similar observations were done in α in a dual-phase steel. Comparable orientation gradients were observed in α adjacent to α', and the affected distance in the α grains is consistent with the present study, namely 200 nm. Furthermore, it was found in [144] that only in the case of very

small α grains (<1 μm^3) surrounded by a high number of α' grains, the α grain was entirely work-hardened due to the martensitic phase transformation. This contributes to the above findings to conclude that the martensitic transformations are not the cause of the deformation in ferrite.

The KAM function can be used to indicate the rotations in ferrite near α', which can act as a more global overview of the effect of α', instead of manually drawing misorientation lines. In Fig. 7-9 KAM is colored in orange, to illustrate the effect of α' on its neighboring α grains.

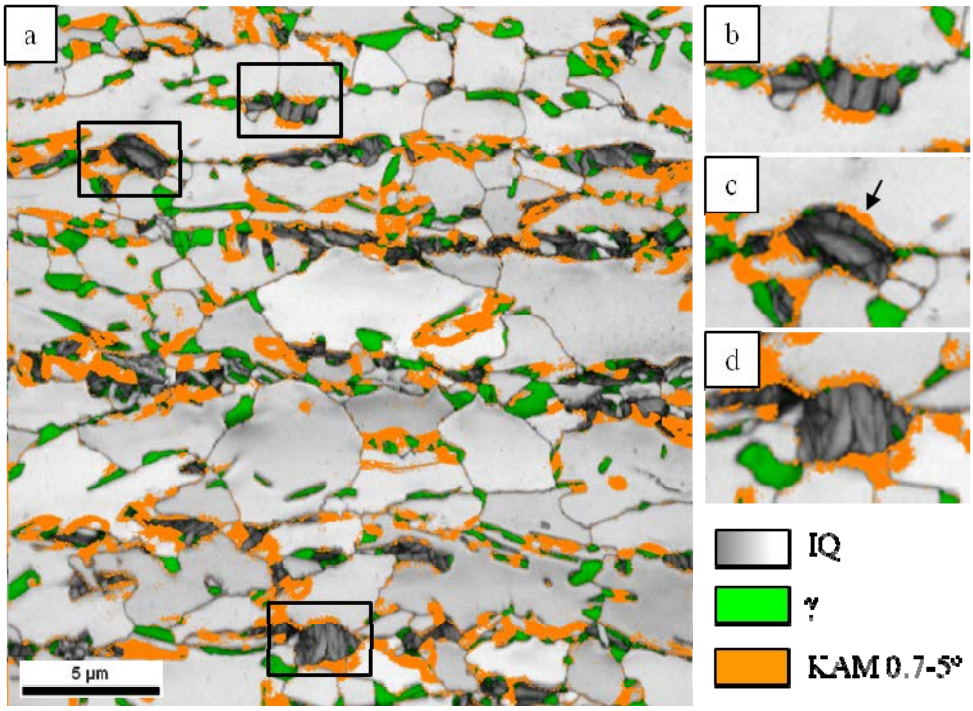

Fig. 7-9. IQ and phase map, where KAM is used to identify the impact on α from α' volume expansions.

The KAM function was used earlier for the identification of bainitic ferrite, therefore also bainitic ferrite is colored orange in Fig. 7-9. The presence of bainitic ferrite is not considered here; only the areas near α' grains are investigated. Observing the magnified martensite grains in Fig. 7-9 (b-d), it is clear that the orange color is exactly located in the ferrite grains adjacent to the martensite grains. KAM identifies small and gradual misorientations between neighboring points in a defined area (kernel), and it identifies exactly the rotations of α near α'. The α' grain in (c) is the same grain investigated with misorientation lines in Fig. 7-8 and it is seen how the local misorientation is only significant in one direction (arrow).

7.5 Transition from HAZ-highT to TMAZ-lowT

The transition from HAZ-highT to TMAZ-lowT causes only small differences in the microstructure, which are difficult to identify. It is deformation that constitutes the difference between the zones, but the very initial deformation causes only small changes in the microstructure, which will be shown in the following.

For the heat treated samples (cf. Section 5.2), misorientation lines were drawn in α grains, to clarify the degree of rotation inside of a grain, which is only affected thermally. It was found that the α grains rotate in the range of 0.1°/µm, measured parallel (or almost parallel) to the RD (Section 5.2.4). This turned out to be very useful knowledge for the distinction between the HAZ and TMAZ in the present sample, which will be presented in the following. In Fig. 7-10 IQ and phase maps from HAZ-highT (a) is shown in comparison with TMAZ-lowT affected by the smallest deformation (b), and TMAZ-lowT, slightly more deformed (c).

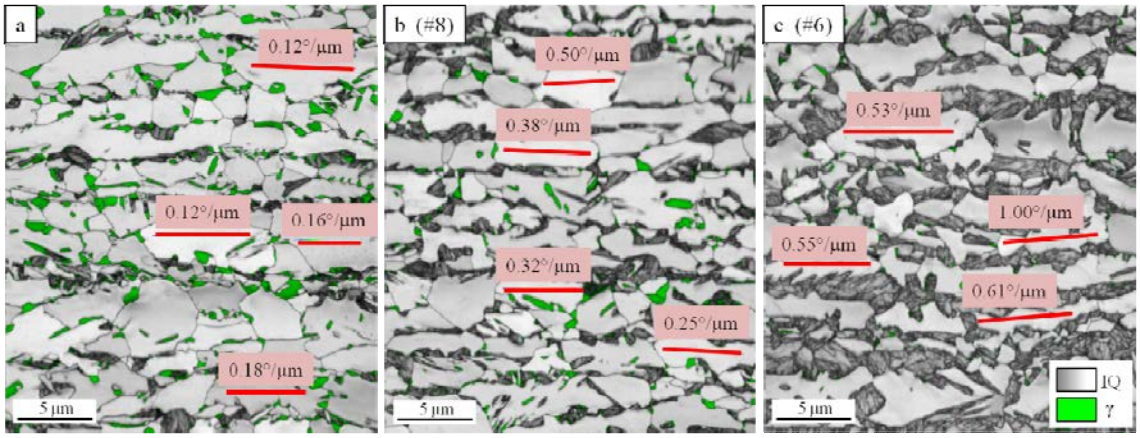

Fig. 7-10. EBSD maps of HAZ-highT (a) and TMAZ-lowT (b, c) with misorientation lines drawn in the ferrite grains.

The location of the EBSD maps can be seen in Fig. 7-2, where (b) is from #8 and (c) is from #6. Misorientation lines are drawn in the ferrite grains in all three maps (red lines), aligned parallel to RD, and the corresponding point-to-origin rotation is indicated for each line. It is observed that the misorientation increases slightly from (a) to (b), and the difference is clearer from (a) to (c), which is closer to pin hole. It was found in the heat treated samples (Section 5.2.4) that the average point-to-origin misorientation in ferrite grains caused only by thermal impact was 0.1°/µm. Therefore, it can be concluded that the rotations in Fig. 7-10 (b+c) certainly are caused by applied deformation.

In the HAZ-lowT it was investigated how the volume expansions caused by α' formation has influenced adjacent α grains. It was found that the ferrite grains were affected by slight rotations

in the nearest 200 nm of α'. This distance is so small that it would not be strong enough to rotate an entire α grain. This argumentation can be used to conclude that the rotations observed in (b+c) are not caused by martensite, but rather by the external deformation applied during welding.

7.6 TMAZ-lowT

The TMAZ-lowT is a broad zone compared to the two HAZs, which can be seen from Fig. 7-2. Six EBSD maps were obtained in the zone, numbered from #3 to #8 along the α' area% curve. It is observed that the hardness profile continues its increase towards the pin hole, similar as observed for the HAZ-highT. In the middle of the TMAZ-lowT (i.e. -2.0 mm from pin hole) the hardness profile reaches a minor plateau before it continues to increase. The α' area% also increases in the beginning of the zone, and enters a plateau at -1.5 mm. The plateau observed in the hardness curve does not precisely coincide with the plateau of the α' curve. Actually, the hardness curve is increasing where the α' area% is decreasing. Microstructure analyses will clarify this behavior later in this chapter. The γ area% is significantly reduced on entering the TMAZ-lowT (#8), and in the remaining part of the zone (#3-7) γ has almost disappeared.

The microstructure development throughout the TMAZ-lowT zone is shown by the IQ and phase maps #3-8 in Fig. 7-11.

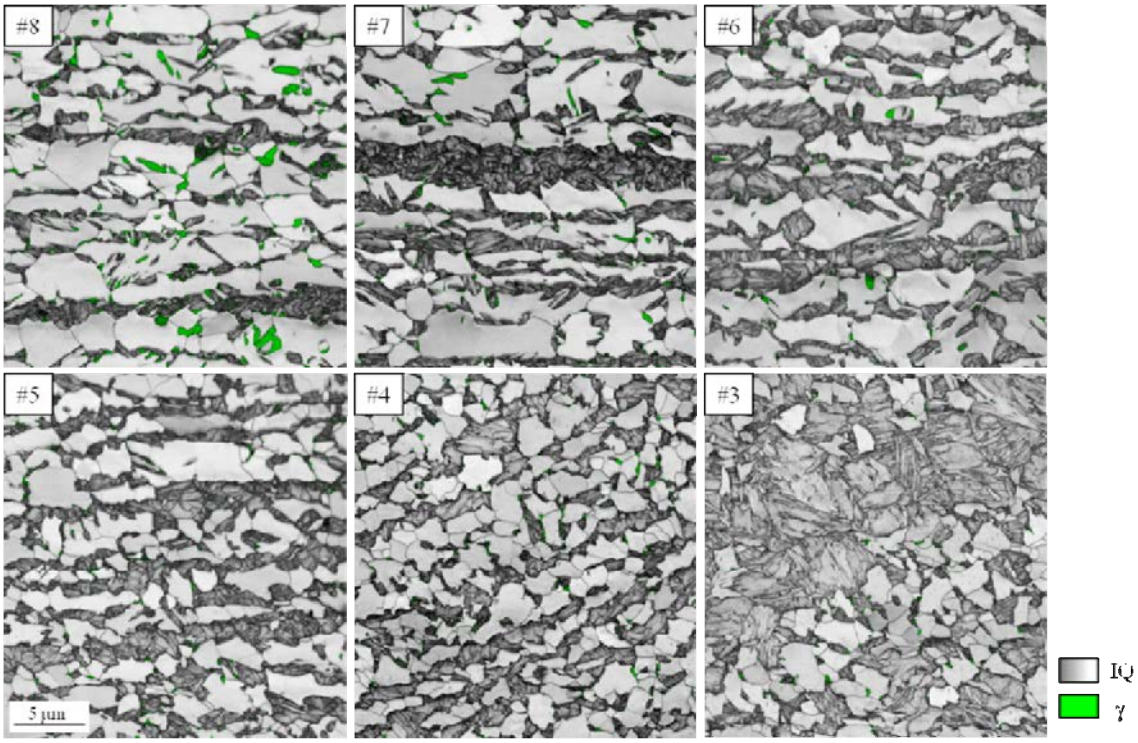

Fig. 7-11. IQ maps of #3-8 in TMAZ-lowT, where austenite is shown in green. The location of the maps can be seen in Fig. 7-2. The magnification is similar in all maps.

It is obvious from the maps that the α' content increases (dark grey) on approaching the weld center. The presence of γ is observed in #8, whereas only a few γ grains can be observed in the other maps. Martensite develops along bands, which was also found in the HAZ-highT. It was earlier described that the preferred formation of α' in bands is caused by segregation of austenite stabilizing elements. The alignment of the α' bands is observed to undergo a shift in #4-5. In #5-8 the bands are aligned mostly parallel with the plane of the sheets. In #4 the α' bands are inclined as a clear indication of the effect of the externally applied deformation. It was shown in Chapter 6 – "Evaluation of all welded samples" that there is an upward flow of the microstructure in this region, caused by the tool rotation. The inclined α' bands in #3-4 are consistent with this.

In the explanation of the transition from HAZ-highT to TMAZ-lowT in Fig. 7-10 it was shown that the first indication of externally applied deformation is a rotation of the ferrite grains. Analogously, the development of the rotation in the ferrite grains is of interest to investigate throughout the zone HAZ-lowT. However, considering misorientation lines is not sufficient for a comparative analysis of all maps. The investigation of LAGBs (with misorientation of 1-15°) would also be inappropriate because, particularly at low deformations, the misorientations from point-to-point are too small. If the rotations occur over a longer distance, they do not become identified with LAGBs because grain boundaries only identify point-to-point misorientations, which will be shown later in this section (Fig. 7-13). Therefore, another method was used to

examine the development of rotations caused by the deformation throughout the TMAZ-lowT; again the KAM function was considered suitable. By using KAM, misorientations occurring over a longer distance are identified. Selecting a very low angle as the lower limit, in this case 0.4° within a kernel of 80 nm, rotations in the range of this angle will appear. The selection of the angular range and kernel size the low angle KAM coloring was done with focus on giving the clearest visualization of the diffuse boundaries developed at the very low deformation. Fig. 7-12 shows EBSD maps from locations #3 to #8 with IPF coloring and low angle KAM (of the ferrite part only) colored black.

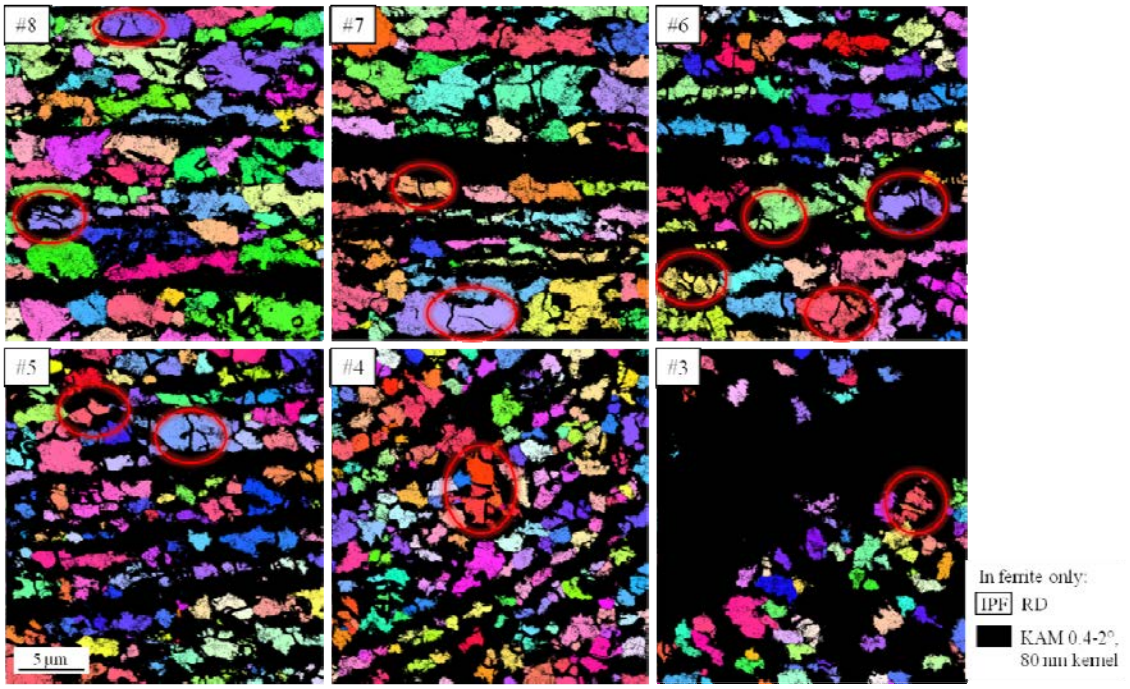

Fig. 7-12. Identification of very small and/or long-range misorientations by low angle KAM colouring. The magnification is similar in all maps. The maps cover similar areas of the microstructure as the maps in Fig. 7-11.

By coloring the low angle KAM, the low angle rotations become evident. This is consistent with the observations in Fig. 7-12, where the black color looks like grain boundaries in some grains (marked with red ellipses), even at very low deformation (#8). These very low angle grain boundaries cannot be identified with LAGBs, because the misorientations are either too low or occur over a long range. The IPF colors also indicate that the rotations are very small, because the neighboring colors are almost identical. On approaching the pin hole, more black lines appear. In #4 and #3, the IPF coloring becomes more random, indicating that the rotations and corresponding orientation changes become larger. For a better view of the significance of the low angle KAM coloring, LAGBs down to 1° were drawn on the maps #3-8 in comparison with low angle KAM (Fig. 7-13).

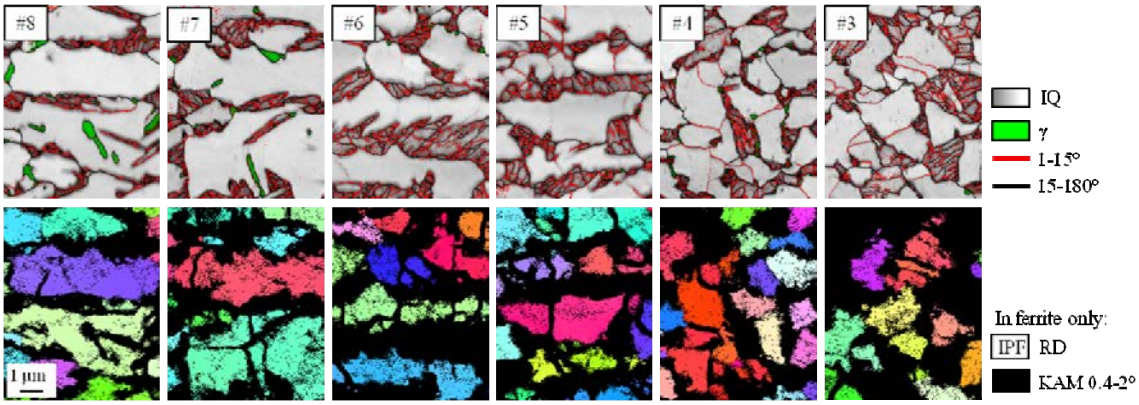

Fig. 7-13. Comparison of LAGB and low angle KAM colouring to show development of LAGBs. It is the same area of the microstructure in the upper and lower row for the six maps.

The IQ maps in the upper row are from the same section as the row below and correspondingly, the same grains are observed in the two rows. for each of the maps #3-8. Evidently, LAGBs were not detected in ferrite grains in #8-6, whereas the low angle KAM coloring indicates that something happens in the ferrite grains. In #5 LAGBs starts to appear but still the low angle KAM identifies boundaries, which are not detected with LAGBs. It is clear from all maps that low angle KAM detects more rotations than LAGBs.

Another way to illustrate the small and long-range rotations is coarsening of the EBSD map, by which the distance between the misorientations becomes smaller. When an EBSD map is coarsened every other point on each row and every other row is removed from the dataset by an automated process, the resolution is reduced by a factor 4. In Fig. 7-13 it was observed that #7 did not contain any LAGBs despite the low angle KAM color indicates misorientations within the ferrite grains. Two selected grains from #7 are shown in Fig. 7-14, to show the effect of coarsening. The EBSD map was coarsened from the original step size of 40 nm up to a step size of 160 nm.

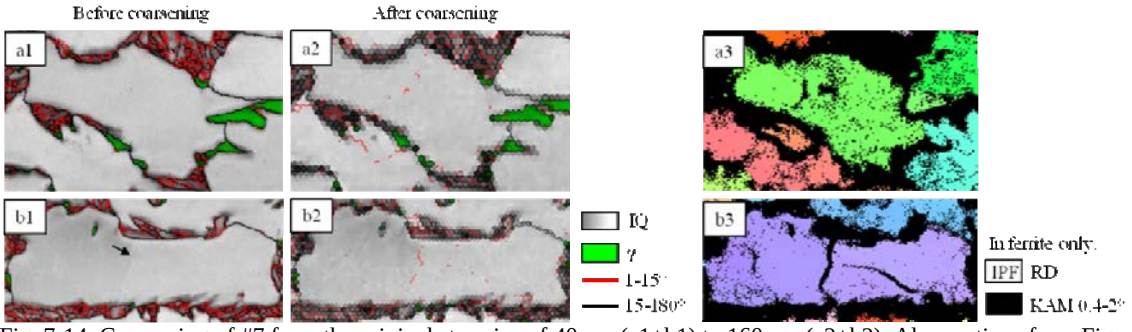

Fig. 7-14. Coarsening of #7 from the original step size of 40 nm (a1+b1) to 160 nm (a2+b2). Also sections from Fig. 7-12 are shown (a3+b3) for comparison.

In the IQ map in (b1) a contrast difference is observed at the location indicated by the black arrow. The contrast difference of the IQ indicates a more or less sudden change in the crystal lattice in this area, however no LAGB was identified. After reducing the resolution by a factor 4, fragments of LAGBs are identified at the same location (a2+b2), which indicates that coarsening of the EBSD map might be used to identify these very small misorientations. Coarsening has the effect that small misorientations in-between four successive pixels are now concentrated to be present in-between 2 pixels. This is interpreted as follows. The slight misorientations indicate the presence of a dislocation distribution. The low angle KAM coloring in (a3+b3) confirms the identification of LAGBs, since misorientations as small as 0.4° occur in the same regions. All together, the small misorientations between pixels suggest the presence of dislocations that bring about a non random rotation of the ferrite grains and a “diffuse” LAGB, i.e. an LAGB that extends of a certain distance. This is interpreted as the initial stage of subgrain formation, where dislocations pile up, before they become ordered to form a LAGB, suggesting that either the mobility of point defects is insufficiently rapid for a reorganization of dislocations (recovery), or that the driving force for this reorganization is insufficiently large (low dislocation density)

From the above analyses it is clear that the externally applied deformation imposes misorientations to develop within the ferrite grains and rotations of the lattice, which increases with applied deformation. It is also clear how to illustrate even the initiate stages of subgrain development by various methods in the EBSD software. Now it is of interest to investigate the orientation of the ferrite crystal lattice with regard to the developed subgrain boundaries, in an attempt to verify if there is a correlation between the developed subgrain boundaries and the crystallographic orientation of the lattice. B.c.c. iron deforms by slip in the <111> direction on the {110}, {112}, and {123} planes [1]. The <111> directions are indicated in IQ maps in Fig. 7-15 in magnified sections of #7 and #5.

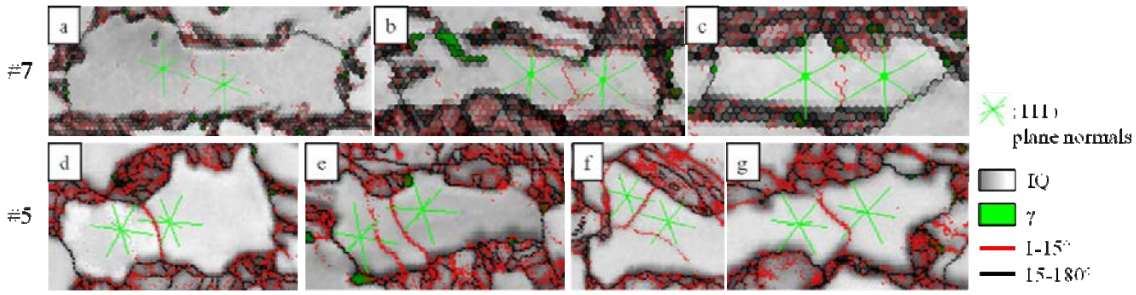

Fig. 7-15. (111) plane normals drawn on IQ maps of #7 and #5 in the ferrite grains where subgrains are developed. The grain in (a) is the same as in Fig. 7-14 (b2).

It is observed in most of the grains that one of the <111> directions are parallel to the developed LAGB. An explanation of this observation requires an investigation of slip systems in the associated ferrite grains. This was not done in the present work

In HAZ-highT, the effect of a volume expansion of α' was investigated and the same investigation is done in TMAZ-lowT to verify how large impact the α' transformation has in the α grains. The α' area% increases significantly towards the pin hole and the impact of the volume expansions becomes larger when the area% of α' is increased. In the HAZ-highT the KAM function was shown to be useful for illustrating the affected distance of ferrite (Fig. 7-9). The same method is used in Fig. 7-16.

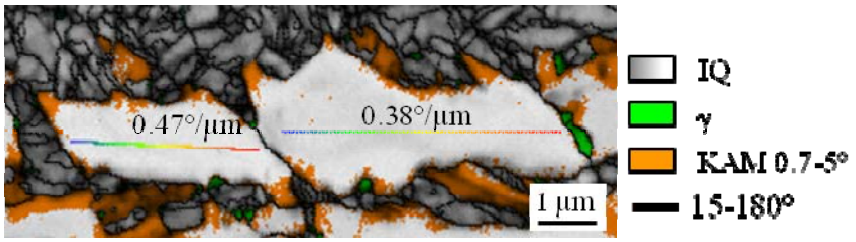

Fig. 7-16. Investigation of the impact of α' volume expansions onto adjacent α grains, investigated with KAM by a similar method as in Fig. 7-9.

It is observed that the region, where α is affected by the neighboring α' is comparable in size to the observations in HAZ-highT, where it was found that α is affected in a distance of less than 200 nm from the α' grain. The rotation gradients (point-to-origin) inside of the α grains are significantly larger in the TMAZ-lowT zone (see lines in Fig. 7-16) as compared to the HAZ-highT zone (0.10°/µm). Since the higher fraction α' does not induce a deeper lattice rotation in the neighboring α grain but the α grains have a significantly higher orientation gradient in the TMAZ-lowT than in HAZ-highT, it can be concluded that the increased α' area% in TMAZ-lowT is not the cause of the α rotations observed in Fig. 7-16.

The mechanism, which explains the subgrain formation at the very beginning of the TMAZ-lowT (#8-7-6) is dynamic recovery (DRV), which leads to subgrain formation separated by LAGBs under the combined effect of temperature and strain. DRV can take place both in the ferrite regime and in the intercritical region, as it was described in Section 2.3.3. In the intercritical region at high strains, DRV is superseded by continuous dynamic recrystallization (CDRX) [99]. During CDRX the sub-boundaries absorb dislocations continuously on further straining; and as a result, the misorientation gradually increases to become HAGBs at higher strain [103]. On approaching the pin hole, the misorientations in ferrite were observed to increase, which is an indication that CDRX takes over from DRV, as a result of the increased strain. However, the changes observed close to the TMAZ-highT zone (#5-4-3) are more difficult to understand and further investigations are needed to clarify the transformations occurring in this region.

It was indicated in Fig. 7-2 that the area % of α' does not follow the hardness curve, but reaches a plateau in #4-5, despite the observation that the hardness continues to increase towards the pin hole. This is an important observation. Correspondingly, the ferrite area% is similar in #4-6 (Fig. 7-17), despite of the hardness increase. The average misorientation in ferrite was calculated with KAM and Grain reference orientation deviation (GROD), which are two useful functions for calculation of the average misorientation of an EBSD map. In this case, the calculations were only applied to the ferrite phase, which was separated from the remaining map with GAIQ. Average KAM was calculated by using a kernel of 80 nm and an angular range of 0-2°. GROD is an automated function, which determines the angular deviation of a point in a grain with reference to the average orientation of that grain. The average GROD of a map is found from averaging over all points in the map. The average KAM and GROD values of ferrite throughout the TMAZ-lowT are shown in Fig. 7-17, in comparison with the α area%. The α' and γ area% curves were already shown in Fig. 7-2.

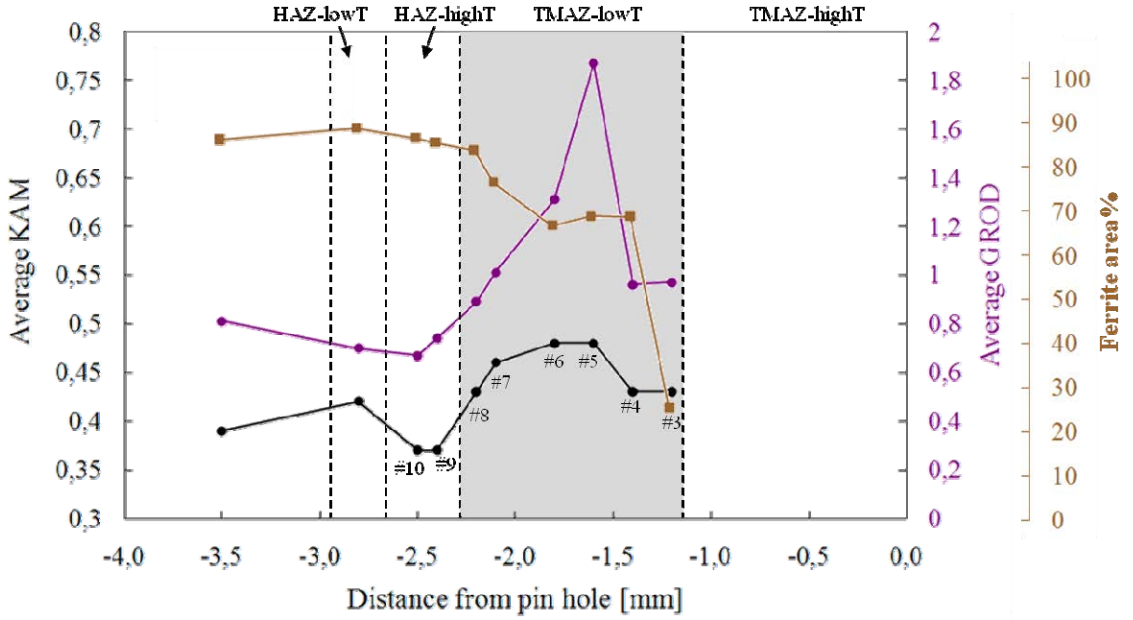

Fig. 7-17. Average KAM (black curve) and GROD (pink curve) of the ferrite phase in TMAZ-lowT, and the α area% (brown curve). The α area% of is almost 0 in TMAZ-highT, therefore no points are seen in this zone.

Clearly, the α area% curve (brown) remains constant from #6 to #4 and interrupts the reduction in area% in the TMAZ-lowT consistent with a constant α' area area% (Fig. 7-2) because the b.c.c. part of the EBSD maps is comprised by the sum of α and α'. The KAM (black curve) and GROD (pink) curves are increasing in the direction towards the pin hole, but both drop drastically from #5 to #4. This indicates lower misorientation within the α grains, which can be a sign of new and/or strain-released α grains. Taken this together with the interrupted decrease in the α area% #4-5, this may indicate that not only are the α grains strain-released, but also new α are formed. Hence, CDRX cannot be the only mechanism occurring in the TMAZ-lowT, otherwise the α' area% curve would not be expected to show a plateau, because the increasing temperature towards the pin hole will increase the area% of α'. Strain-induced transformation (SIT) of ferrite may occur in the present region. SIT of ferrite occurs in the temperature range between Ar_3 and Ae_3 under the influence of very high strain [92][145]. The α grains formed by SIT attain a characteristic fine grained (1-3 μm) morphology; the grains are equiaxed and are aligned in arrays, intragranularly in austenite [92][111][107]. Depending on the strain level, the morphology changes; at relatively low strains the ferrite grains impinge on only the neighboring grain, thereby creating planar arrays; at relatively high strains the impingement is three-dimensional, so that the fine ferrite grains attain a more massive morphology (Fig. 2-1) [111][112]. In an attempt to separate between ferrite formed by CDRX and SIT from their morphology, the characteristics from Table 2-5 are considered, which will be used in the following to discuss the microstructure evolution occurring in the part of the TMAZ-lowT zone (#3-4), which is closest to the pin hole. Combined IPF and IQ maps of this region are shown in Fig. 7-18.

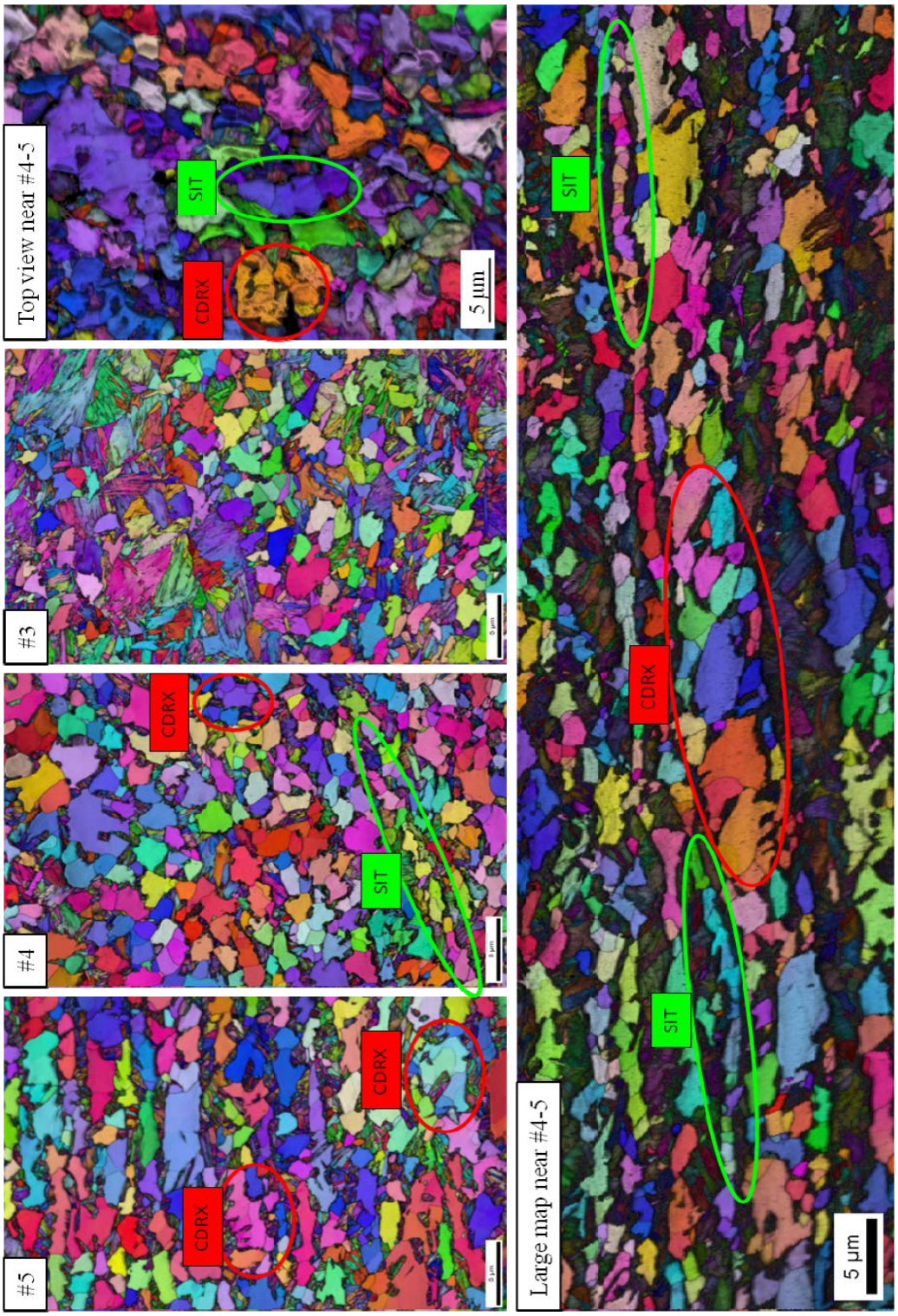

Fig. 7-18. IQ and [RD] IPF maps of the microstructure in TMAZ-lowT close to TMAZ-highT. Red and green ellipses mark morphologies, which are indicative for CDRX and SIT, respectively.

In #5 the original ferrite grains can still be recognized, and the fragmentation is clearly seen, indicating that DRV and CDRX have taken place. Since for the present case a continuous process applies, no distinction will be made between the two mechanisms, and only CDRX will be used to describe the formation of LAGBs and HAGBs within deformed ferrite grains. There is a significant change in the morphology from #5 to #4, where the orientation of the ferrite grains becomes much more random, and the original large ferrite grains are no longer recognized. The ferrite grains are observed as more equiaxed and fine grained in #4 as compared to #5. From Fig. 7-17 it was found that the area% of ferrite changed its tendency from #5 to #4 indicating that new ferrite is formed in #4, and furthermore that the average misorientation of ferrite decreased from #5 to #4. These observations point towards SIT as a possible mechanism to the formation of new ferrite in #4. Based on morphology observations, ferrite grains with a typical SIT appearance are indicated in Fig. 7-18 with green ellipses. The arrays of fine equiaxed ferrite grains is a typical sign of SIT, and the location in-between martensite bands points towards that it has formed intragranularly in austenite. Particularly in "Large map near #4-5" in Fig. 7-18 the ferrite grains marked with SIT are seen to be sandwiched in-between α' arrays. In #3 it is not possible to recognize any characteristic morphology of the ferrite grains. The EBSD map from "top-view" in Fig. 7-18 is performed to verify whether the formation of thin bands of ferrite is caused by flattening out of ferrite grains from the material flow, which cannot be identified from RD. From the top-view both large ferrite grains (red ellipse) is recognized, and bands of equiaxed ferrite grains are observed (green). Thus, the equiaxed morphology is observed in both cross section and in the top-view section. This finding confirms that the arrays of equiaxed ferrite grains, as observed in #4 are not just elongated ferrite grains.

To support the observation of ferrite formed by SIT from Fig. 7-18, a schematic illustration of the mechanism is shown in Fig. 7-19.

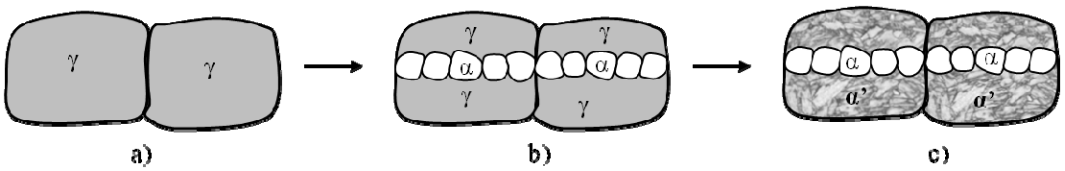

Fig. 7-19. Illustration of SIT of ferrite. Austenite grains (a) are deformed in the temperature range between Ar_3 and Ae_3 with the result of SIT of ferrite nucleated intragranularly in austenite (b). Upon cooling, remaining austenite is transformed into martensite (c).

Fig. 7-19 illustrates the intragranular growth of ferrite in austenite grains during SIT, and how the characteristic appearance of the ferrite grains is developed. This is particularly important in comparison with the observation in "Large map near #4-5" in Fig. 7-18 (green ellipses), where arrays of small, equiaxed ferrite grains are observed to be sandwiched in-between martensite. This location of the ferrite arrays is a clear indication that ferrite has nucleated intragranularly

within austenite, and the austenite surrounding the new ferrite grains, is transformed into martensite upon cooling.

Texture analysis is another way to determine the origin of the ferrite grains, which is very reliable because the texture of ferrite is strongly bound to the transformation mechanism. The ferrite texture of the various transformation mechanisms was presented in Table 2-5. However, the texture analysis cannot be applied in the present study. First, because it would require a minimum of 200-500 grains to enable a reliable texture analysis, and the EBSD maps obtained in the present study do not contain that many ferrite grains. That could be overcome by acquiring larger maps but then arises the next and most constraining problem: CDRX and SIT transformations both occur in the same (or nearly the same) location, and separation of the two types of ferrite grains is not possible by any automated functions in EBSD, because the ferrite grains attain a comparable size and shape. Therefore, both types of ferrite grains would be included in the analysis, and no conclusion can be drawn. The texture analysis can be performed in #6-8 to confirm that shear is occurring, but that was already obvious from the previous investigations.

Summarizing, the following indications of CDRX and SIT are found:

Indications for CDRX:

- The development of subgrains in α at a low strain is clear and it becomes more pronounced on approaching the pin hole
- The morphology clearly indicates that recrystallization occurs in α
- (111) slip plane normals assist to show that subgrain formation occurs along the <111> direction which is expected for deformed α (less strong evidence)

Indications for SIT:

- The ferrite area% is reduced towards the pin hole in the entire TMAZ-lowT but this tendency is interrupted in #4-5
- SIT is known to occur just below Ae_3, consistent with the temperature, where it is observed (close to TMAZ-highT)
- The morphology indicates that SIT of α has produced fine, equiaxed ferrite grains aligned in arrays in-between martensite bands.

All-together it is concluded that CDRX is the dominating mechanism in the TMAZ-lowT, and SIT of ferrite occurs concurrently with CDRX in the narrow temperature range between Ar_3 and Ae_3, which is neighboring the TMAZ-highT zone.

7.7 Transition between TMAZ-lowT and TMAZ-highT

In the transition from TMAZ-lowT to TMAZ-highT, the hardness reaches a maximum and the area% of α' becomes close to 100 % (Fig. 7-2). This is an indication that the temperature has been above Ac_3 in the TMAZ-highT during welding. The exact value of the Ac_3 temperature cannot be determined because deformation, i.e. external work exerted on the system, will shift the transition temperature. In this study the subdivision in zones is the transition between the martensitic-ferritic dual-phase microstructure and the fully martensitic microstructure. The Ac_3 temperature will be referred to as the border between the zones, but the actual value is not clarified further.

7.8 TMAZ-highT

The hardness profile and the area% of γ and α' in TMAZ-highT are seen in Fig. 7-2. It is observed that the microstructure is almost fully martensitic in the TMAZ-highT. The hardness reaches a maximum just after entering the zone (-1.0 mm), and thereafter falls to a more or less constant level.

The morphology of the microstructure can be seen in from the IQ maps in Fig. 7-20.

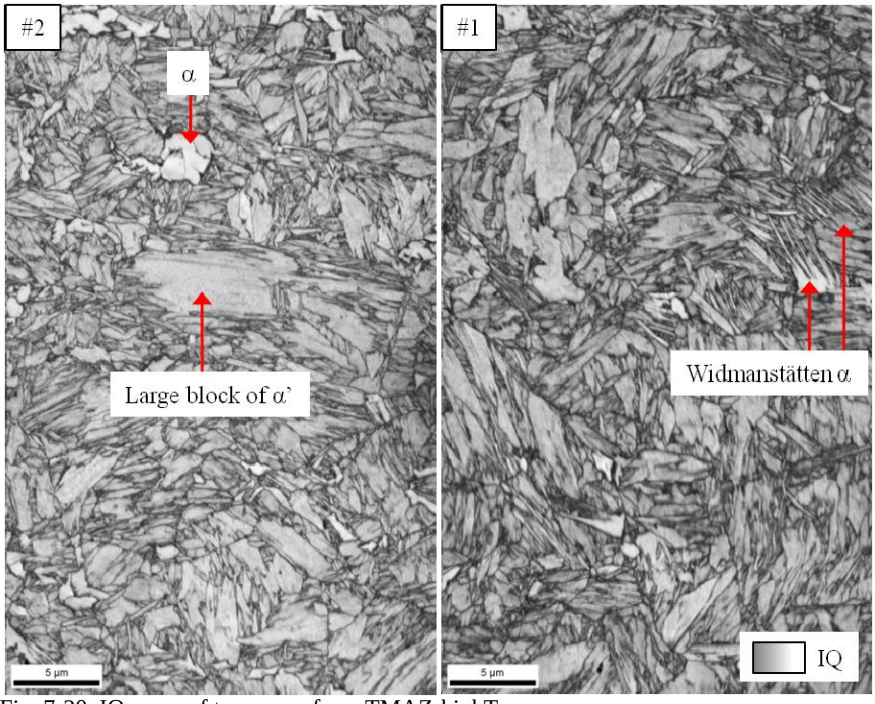

Fig. 7-20. IQ maps of two maps from TMAZ-highT.

A martensite grain with a very large block size is observed in #2, as indicated in the image. Since the block size in lath martensite increases with decreasing carbon content [146], it can be concluded that there is a locally lower carbon content in the large martensite blocks compared to the remaining microstructure. The variation in carbon content will cause variations in the hardness. The most significant variation in hardness was observed close to the TMAZ-lowT, where the temperature and strain are lower. The characterization of the microstructure also revealed a more varied block size in this region, thus confirming the relation between the block size (and thereby carbon content) and hardness. Perhaps the stirring of the microstructure and/or diffusion was lower in this region and therefore not sufficient to mix up the carbon content in the austenite microstructure before transformation into α'.

In the almost fully martensitic microstructure a few α grains are observed, as pointed out with an arrow in #2 in Fig. 7-20. This was also confirmed by characterization with SEM and RLM, but not shown here. It may be ferrite grains, which have remained from the BM, as a result of stabilization by alloying elements such as Zn and O [147]. Alternatively, it may be ferrite grains, which have nucleated on inclusions or highly dislocated regions during cooling [148]. It could also be a combination of the two described reasons.

Another observation from the microstructure in Fig. 7-20 is the presence of Widmanstätten ferrite grains, which are pointed out in #1. Widmanstätten ferrite has a very characteristic appearance consisting of parallel plates emanating from the same grain. The broad faces of the plates are partially or fully coherent with the parent phase and the growth occurs displacively [1]. Widmanstätten ferrite develops within a range of particular cooling rates but it can also be caused by local conditions, which promote the directional growth of the plates, such as the carbon content and deformation [1].

EBSD does not indicate any significant amount of γ or carbides in the TMAZ-highT, because the resolution of EBSD is too poor to identify carbides and very small austenite grains. Therefore, TEM analysis is necessary (Fig. 7-21).

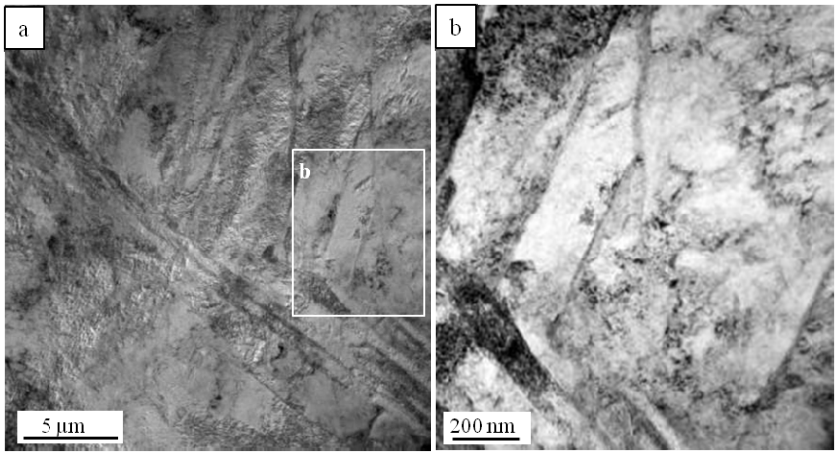

Fig. 7-21. TEM micrographs from TMAZ-highT.

The TEM micrographs in Fig. 7-21 indicate a typical lath martensite microstructure with the presence of dislocations. Several diffraction analyses were performed to verify which phases are present. The indexing of the diffraction patterns pointed towards an identical phase in the entire microstructure; a slightly tetragonal b.c.c. lattice. This confirms that it is lath martensite. The tetragonality depends on the carbon content and it was attempted to determine the carbon content from the lattice constants achieved in the diffraction patterns [149]. However, the results were inconsistent, which may be caused by large variation in the carbon content, or stresses and stacking faults in the microstructure. Therefore, the results could not be used to determine the carbon content. No other phases than martensite were identified from the diffraction patterns.

A particular morphology was observed during the TEM analysis, as is shown in Fig. 7-22.

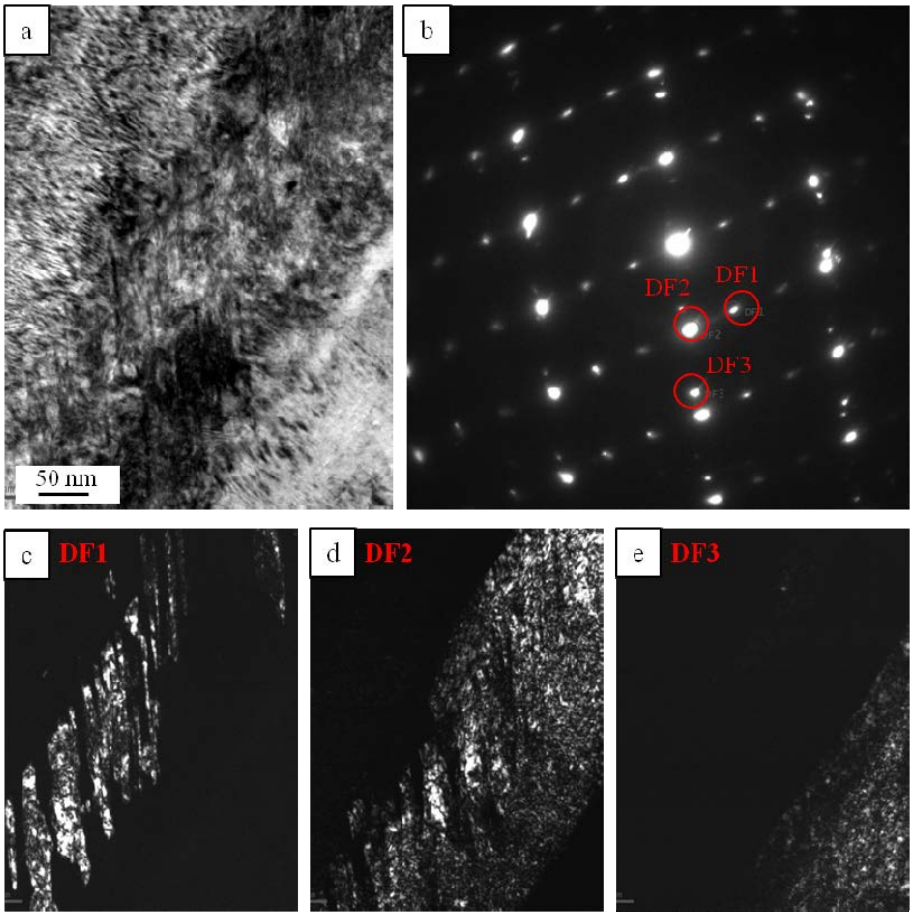

Fig. 7-22. Diffraction analysis of area containing lamellar structures. Bright field image (a), diffraction pattern (b), and three corresponding dark field (DF) images (c,d,e).

The particular morphology becomes evident from the dark field images in (c-e), where parallel laths are observed. In the electron diffraction pattern (Fig. 6-22b) three spots were selected for dark field imaging (Figs. 6-22 c-e). The dark field images show that several regions diffract independently, but have the same lattice spacing. The lamellar features in the microstructure are from the diffraction pattern suggested to be microtwins. Twins do normally not form in lath martensite, only in plate martensite [1]. Therefore, the suggested presence of twins indicates that locally in the TMAZ-highT zone the carbon content is high enough to promote plate martensite. Apparently, such regions compensate for those in the same zone, where the carbon content is locally lower than the average content in the alloy.

It was concluded from the almost fully martensitic microstructure that the temperature was above Ac_3 in the TMAZ-highT during welding. During welding, γ was exposed to a high strain simultaneously with the high temperature, and that will probably lead to recrystallization of γ before it transforms into α'. To verify whether recrystallization has indeed occurred, the morphology of the prior γ grains was retrieved. The prior austenite grain boundaries can be reconstructed from the EBSD maps of the martensite microstructure [150][151][152][153][154].

When γ is transformed into lath α', the Kurdjumov-Sachs (K-S) orientation relationship is generally followed [1], which can be expressed as:

There are 24 crystallographically equivalent combinations of planes and directions (variants) that fulfill the K-S relationship. The 24 variants of martensite are given in Fig. 7-23 on a (001)[100] stereographic projection of austenite.

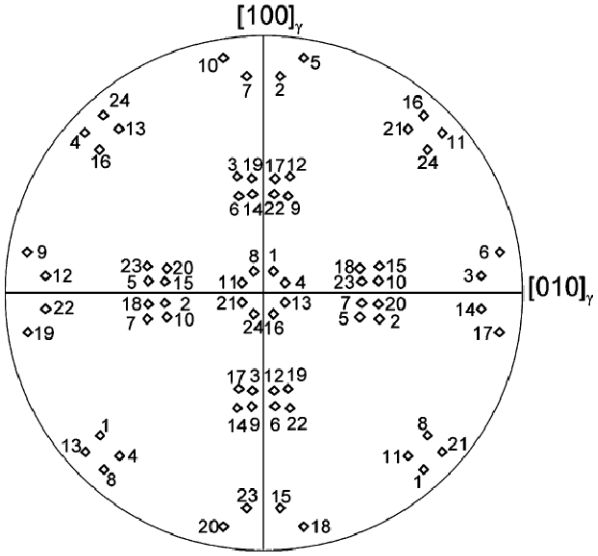

Fig. 7-23. (001)[100] pole figure showing the orientations of the 24 possible martensite variants, which can form from one austenite grain, when the K-S orientation relationship is followed [150].

To determine the prior austenite grain the IPF colored map and the [001] pole figure of the b.c.c. phase have to be considered simultaneously. Martensite blocks are pointed out in the IPF colored map by the highlighting tool in the software, and the corresponding orientation will be plotted in the pole figure. The method is illustrated in Fig. 7-24, where an IPF colored map from #1 and the corresponding [001] pole figure are shown.

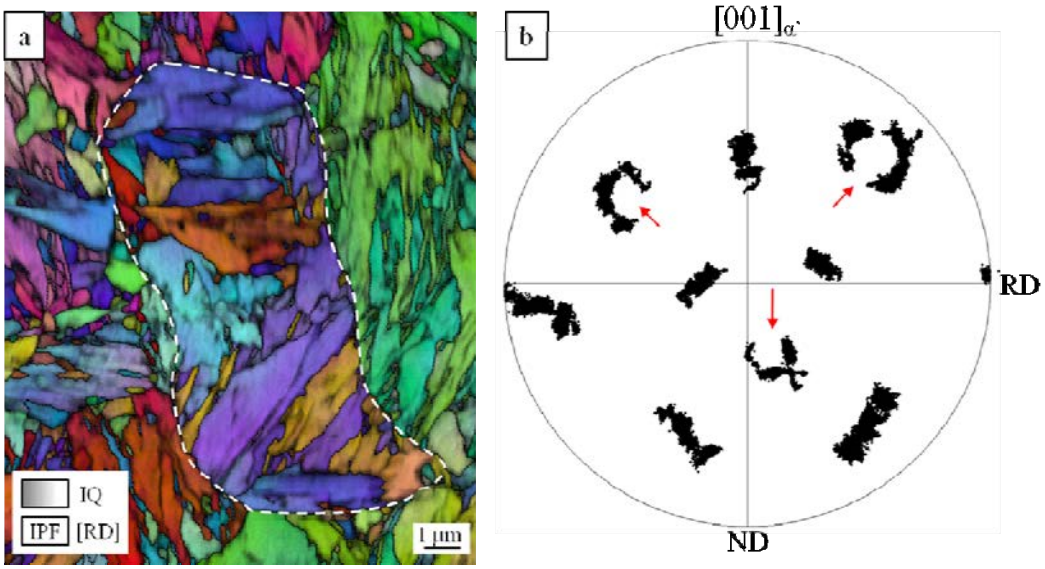

Fig. 7-24. IPF colored map in #1 (a) with a white, dashed line indicating a prior austenite grain boundary. The [001] pole figure of martensite (b) shows the orientations of the crystals within the prior austenite grain in (a).

The white dashed line in Fig. 7-24 (a) indicates a prior austenite grain boundary, and the orientation of all points within this boundary is shown in Fig. 7-24 (b). This indicates that the points have their origin in the same austenite grain. Based on the pole figure, the prior austenite grain boundary in Fig. 7-24 (a) can be drawn. In the literature, it has recently been attempted to develop an automated method for the determination of prior γ grains by EBSD [155]. The manual method is also acceptable if the amount of data to be analyzed is relatively small. In the following, the manual method is applied to the two EBSD maps from the TMAZ-highT zone (Fig. 7-25).

Some variants are not represented in the prior austenite grain (red arrows in Fig. 7-24) but no further investigation as to why they are missing was performed in the present study. This could be related to the role of deformation/stress which promotes some of the variants and suppresses others.

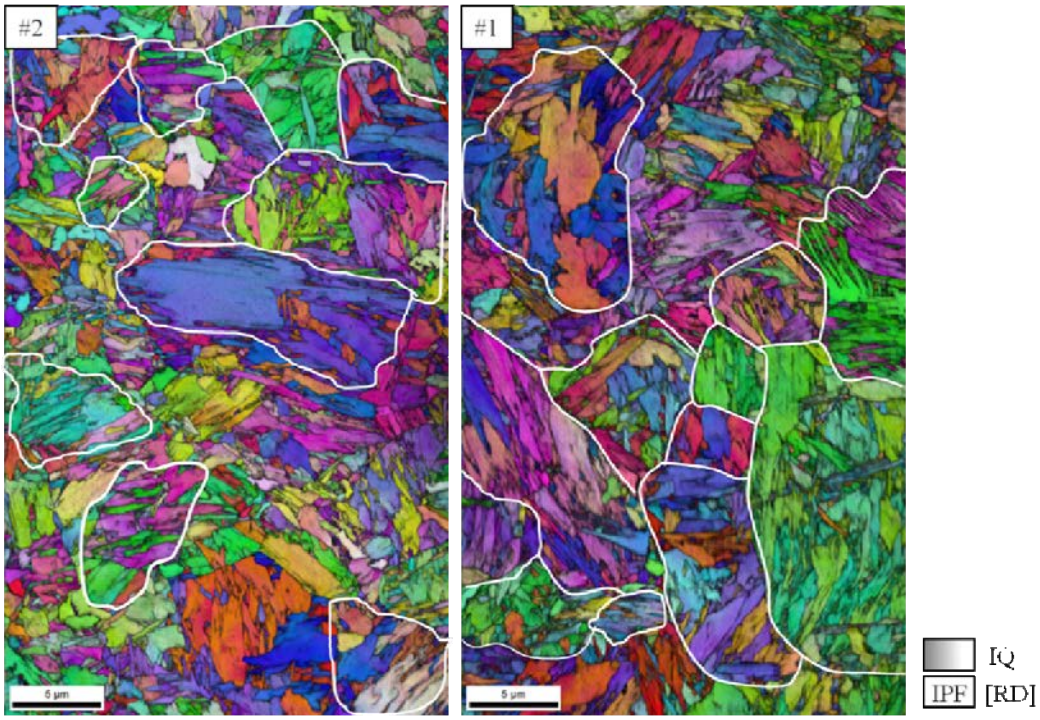

Fig. 7-25. IPF colored maps from #2 (a) and #1 (b), where prior austenite grain boundaries are indicated with white lines.

The result of the manual analysis of former austenite grain boundaries is shown in Fig. 7-25. It is observed that the main part of the γ grains is equiaxed, which indicates that recrystallization has occurred in the zone. It would have been interesting to investigate the prior γ grain size in the entire TMAZ-highT, as a function of the distance to the pin hole. This would allow to clarify whether the entire zone was recrystallized before martensite formation, and whether grain growth occurred locally.

In FSSW, and particularly FSW, the zone closest to the pin hole is known as the stir zone (SZ), which indicates a region, where full stirring has been achieved. However, in the case of low carbon steel, it is not straightforward to determine the SZ. After the investigations of the TMAZ-highT, the term SZ would be acceptable to use for this zone, but TMAZ-highT is preferred because it divides the zones according to the transformation temperatures, and not according to their state of stirring. Therefore, for comparison with other studies, it is acceptable to use SZ for the TMAZ-highT identified in Sample 1500-1, but in general for low carbon steel, TMAZ-highT should be used.

7.9 Edge of pin hole

In the almost fully martensitic microstructure in TMAZ-highT, an area of ferrite grains is observed along the edge of the pin hole. In Fig. 7-26 the location of these observed ferrite grains are shown.

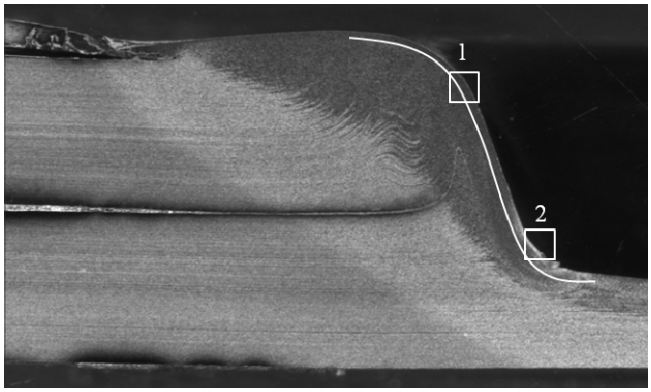

Fig. 7-26. Location of ferrite in TMAZ-highT (marked with the white line). 1 and 2 refer to the detailed investigations in Fig. 7-27.

The narrow zone of ferrite grains is pointed out with the white line. In the bottom of the pin hole at location (2), the ferrite zone is widest. The numbers 1 and 2 refer to two different widths, where (2) is from the wide ferrite zone, and (1) is representative for the upper part. Magnified RLM images of the regions marked with 1 and 2 are shown in Fig. 7-27.

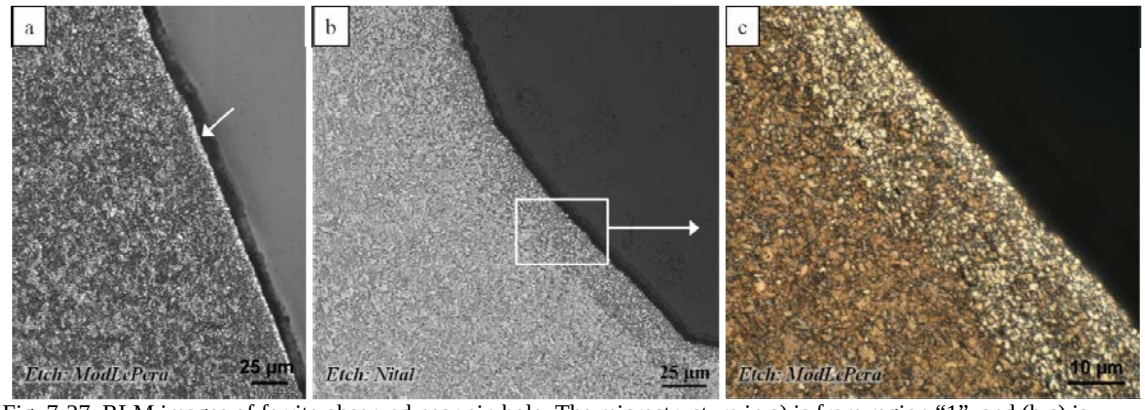

Fig. 7-27. RLM images of ferrite observed near pin hole. The microstructure in a) is from region “1”, and (b,c) is from “2”, both marked in Fig. 7-26.

In Fig. 7-27 a) the ferrite zone is very narrow (< 10 µm), which is representative for the main part of the ferrite zone. The wider ferrite zone (> 25 µm) in (b+c) is only observed in the bottom

of the pin hole, which is marked with “2” in Fig. 7-26. In both regions, the ferrite zone follows the shape of the pin hole.

In the literature, similar ferrite zones were observed in FSSW of low carbon steel [63]. The ferrite is also located in regions with a fully martensitic microstructure, similar as seen in the present study. So far it was not verified how this ferrite zone was formed. Several hypotheses will be discussed below.

Ferrite can be stabilized by the presence of certain alloying elements such as Zn, Al and Si [147]. However, the microstructure is fully stirred, where the ferrite region is observed, and consequently, alloying elements will not concentrate along the edge but become mixed up in the microstructure. Alloying elements from oxides are also not expected to contribute to ferrite stabilization since Ar gas was used as shielding gas during welding, which prevents the formation of oxides.

It is possible that δ-ferrite has formed near the pin hole during welding. The temperature, where δ-ferrite develops, is around 1400°C [1]. The maximum temperature is not completely determined in the present study but the thermal modeling suggest a peak temperature in the range of 1100°C, which is far below the temperature regime for δ-ferrite. However, deformation plays a significant role for the transformation temperature, and the temperature does not necessarily have to be above 1400°C for the production of δ-ferrite if heavy deformation is applied simultaneously. The observed ferrite is located near the edge of the pin hole, which is the region of highest temperature. The ferrite zone is found to be widest in the bottom of the pin hole, and this is the region of the workpiece, which has been exposed to the largest degree of deformation, according to the findings of microstructure flow, as described in Fig. 6-8”. Here it can be seen that the microstructure flow changes direction, exactly in the bottom of the pin hole, which induces the largest deformation. Therefore, it is very likely that the ferrite observed near the pin hole is δ-ferrite.

Another possible explanation to the ferrite band near the pin hole is decarburization from the surface of the pin hole. At the high temperature during welding, carbon burn off from the surface by reaction with oxygen. If there is not enough carbon, α’ cannot form and instead α will be formed from γ on cooling. The diffusion distance of carbon is at elevated temperatures can be calculated, and a calculation was done with the following assumptions:

- Carbon content in steel; 0.25 wt%
- Carbon content in surroundings; 0 wt%
- Temperature: 1100°C
- Phase at elevated temperature: γ-Fe
- Solubility limit of C in α-Fe at 25°C: 0.021 wt% [142][147]

The calculation was done after three different times at the temperature; 5, 10 and 20 seconds. The calculated distance of carbon to diffuse out of the material was **2.3 µm** after 5 seconds, **3.3**

µm after 10 seconds; and **4.6 µm** after 20 seconds. When deformation is applied simultaneously, diffusion occurs much easier, and larger distances can be expected. Also the temperature may have been higher than 1100°C, which would increase the diffusion distance as well. Based on the calculations, it can be concluded that decarburization is also a possible explanation for the formation of ferrite along the pin hole edge. In addition to the lower carbon content along the pin hole, also the temperature for δ-ferrite formation is lowered, why the decarburization will contribute to the formation of δ-ferrite.

It cannot be verified whether formation of δ-ferrite or decarburization is most probable for the formation of the ferrite region, and probably it is a combination of the two. Both decarburization and formation of δ-ferrite are increased by increasing temperature and deformation, and therefore it is expected that there is a correlation between weld parameters and the presence of ferrite along the pin hole. In samples welded at lower temperature and deformation (e.g. 500 rpm) no ferrite band along the pin hole was found, which is consistent with the given.

The fact that the ferrite region is wider in the bottom of the pin hole is consistent with δ-ferrite formation and decarburization. In the bottom of the pin hole, the deformation is larger than in the upper part of the pin hole as a result of the material flow during welding (cf fig X in All welds). Both δ-ferrite formation and decarburization are promoted by deformation, and therefore the width of the ferrite region is consistent with the two proposed mechanisms.

7.10 XRD analysis

XRD was performed on Sample 1500-1 with two different collimator sizes (0.5 mm and 0.1 mm, respectively), which correspond to different spot sizes on the sample and hence, XRD averages over different volumes in both cases. The 0.5 mm collimator is useful for a reliable identification of the phases at different locations in the weld, but the fairly large spot size does not allow to resolve all individual zones in the weld. The 0.1 mm collimator is used for more localized measurements, but the correspondingly lower diffracted intensity hinders proper analysis of the measured peak profiles in terms of quantification of the present phases and microstructural features. Only the $(110)_{\alpha}$ peak has a high enough intensity in the 0.1 mm collimator measurement, which allows reliable evaluation of the peak position and width in the localized measurements covering all welded zones. The location of both XRD measurements on the cross section of the sample was shown in Fig. 3-8.

The three diffractograms measured with the 0.5 mm collimator measurements are seen in Fig. 7-28.

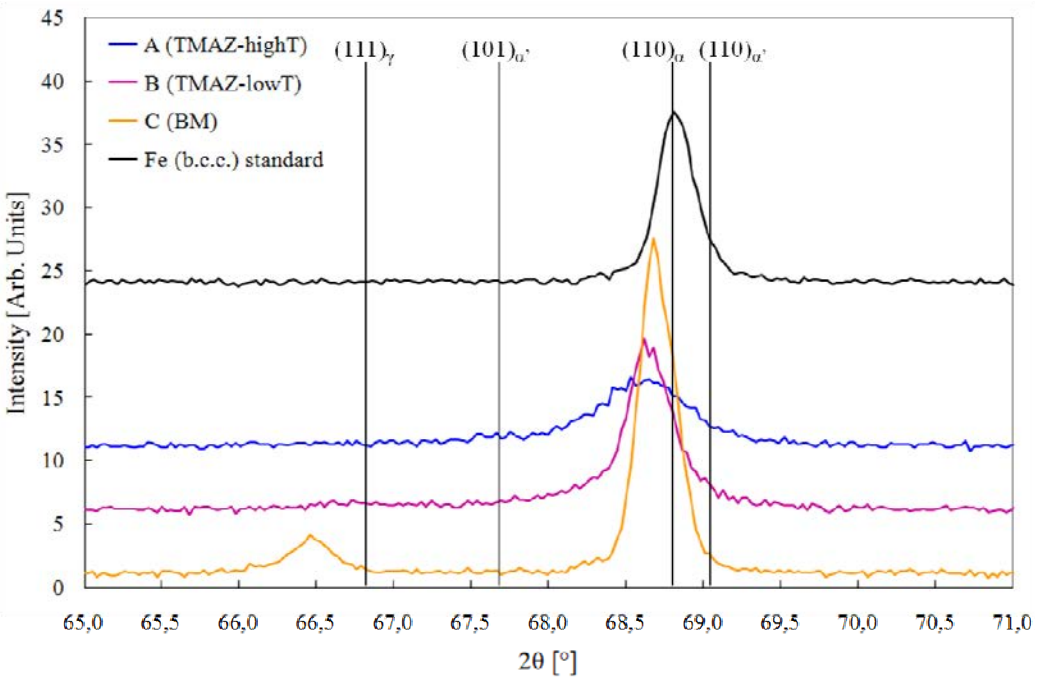

Fig. 7-28. X-ray diffractograms measured in three regions on Sample 1500-1 (A, B, C) and in the Fe (b.c.c.) standard. The four diffraction patterns are shifted vertically for a clearer interpretation of the peaks. Theoretical peak positions are marked according to the JCPDS card numbers: γ – 31-0619, α – 06-0696, α' – 44-1291. The black curve indicates a good alignment status of the instrument.

Only the 65-71° 2θ section of the diffractograms is shown, since it covers the highest diffracted intensities.

The diffraction pattern measured in BM was discussed in Chapter 4 – "TRIP steel base material", but will also be analyzed in the following, in comparison with the welded zones. It is observed in Fig. 7-28 that the $(111)_\gamma$ and $(110)_\alpha$ peaks are easily identified in C (BM). In B, the $(110)_\alpha$ peak is also clearly identified whereas the $(111)_\gamma$ peak is very weak in Fig. 7-28, but the fitting procedure confirmed a minor peak at 66.7°2θ, which corresponds to $(111)_\gamma$. In A the $(111)_\gamma$ peak is even weaker but peak profile fitting also confirmed its presence in this pattern. No other phases, such as cementite or other carbides, were identified in any of the three regions.

In C, the position of both the $(111)_\gamma$ and $(110)_\alpha$ peak is shifted to lower °2θ compared to the database values. In Chapter 4 the shift was discussed with regards to the effect of carbon. There is an average content of carbon of 0.24 wt% in the alloy, which certainly will cause a shift of the diffraction peaks due to the increased lattice parameter. However, also compressive macrostresses contribute to a shift of the peaks in BM, and distinction between the effect of alloying elements and stresses cannot be verified from the present analysis. In B and A, the $(110)_\alpha$ peak is also observed to be shifted, and the width of the peaks has also increased. The $(110)_\alpha$ peak is the only peak, which is significant in all three regions in Fig. 7-28, and it allows

for line profile analysis. That will delineate differences in the position and width of the peak as a result of differences in the microstructure in the three regions. The results of the line profile analysis are given in Fig. 7-30 and Fig. 7-31, where the FWHM and °2θ of the $(110)_{\alpha}$ peak are plotted as a function of the distance to the pin hole. Both figures include also results from the XRD measurements with the 0.1 mm collimator, where more localized XRD measurements were performed at different locations within the various weld zones

Peak profile fitting for applied to measurements in all three regions shown in Fig. 7-28 revealed that the $(110)_{\alpha}$ peak is asymmetric. The asymmetry was found to be caused by the presence of b.c.t.-Fe, which gives rise to two peaks; $(101)_{\alpha'}$ and $(110)_{\alpha'}$, which overlap with the b.c.c. $(110)_{\alpha}$ peak. The location of the b.c.t. peaks according to database values is marked in Fig. 7-28 on both sides of the $(110)_{\alpha}$ peak. The identification of b.c.t. peaks in all three diffraction patterns indicates a minor amount of b.c.t. in all three zones, which means that a minor part of the microstructure contains the tetragonal martensite, whereas the remaining b.c.c. part can originate either from ferrite or martensite or a combination of both. It cannot be verified from XRD whether the b.c.c. is martensite or ferrite, and microscopy is needed as supporting analysis. The findings from Fig. 7-28 are combined with the EBSD characterization performed earlier in this chapter, and for comparison, representative EBSD maps of the three regions, A, B and C, are presented in Fig. 7-29.

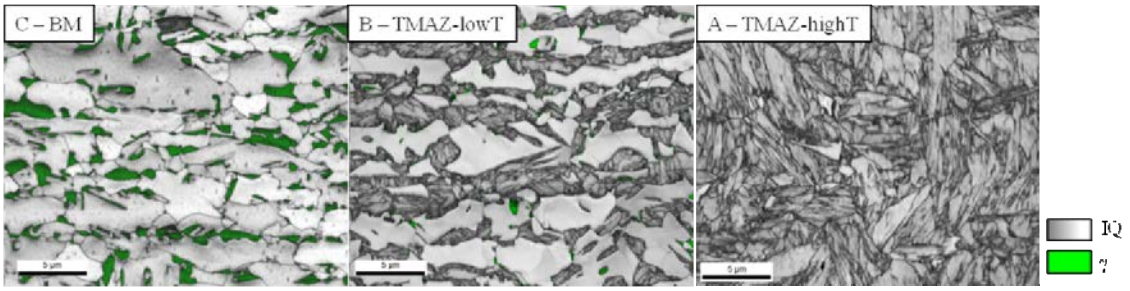

Fig. 7-29. IQ maps from region A, B, and C, where the XRD measurements in Fig. 7-28 are performed.

The microstructure characterization performed prior to the XRD measurements on exactly the sampe sample has concluded the following; C contains austenite and ferrite as the main components, with a minor amount of martensite and bainitic ferrite. B contains a dual-phase microstructure with varying amounts of ferrite and martensite, and only very few austenite grains. A was found to be almost fully martensitic. Ferrite, martensite and bainitic ferrite are all indexed as a b.c.c. phase in EBSD (grayscale in Fig. 7-29), and the minor variation in lattice parameters caused by e.g. carbon is not detectable by EBSD. However, the EBSD analysis is very useful in comparison with the XRD results. As mentioned above, the b.c.c. indexed in XRD cannot distinguish between ferrite, martensite and bainitic ferrite, and the b.c.t. is not the only content of martensite in the microstructure. The results from XRD can only conclude the following: The identification of mainly b.c.c. in A, B and C with an increased d-spacing

indicates that the main part of the microstructure is b.c.c. iron with a relatively low carbon content, which does not induce a tetragonal shape of the lattice but the cubic lattice is retained. Furthermore, a minor part of b.c.t. is identified in all three regions, which is caused by local carbon rich regions. In the EBSD analysis it was found in TMAZ-highT that the block size of α' was varying as a result of a heterogeneous carbon content, and the finding of a minor amount of tetragonal martensite in the XRD analysis confirms this.

The combined EBSD and XRD results lead to the following conclusions on the phases identified in the three regions in Fig. 7-29:

- C (BM): Ferrite (b.c.c.), austenite (f.c.c.), and a minor amount of martensite (b.c.t.)
- B (TMAZ-lowT): Ferrite (b.c.c.), Martensite (mainly b.c.c. and minor part of b.c.t.), and minor amounts of austenite (f.c.c.)
- A (TMAZ-highT): Martensite (mainly b.c.c. and minor part of b.c.t.) and traces of austenite

As mentioned above, the $(110)_{\alpha}$ peak is the only peak, which is significant in all the XRD measurements performed with both the 0.5 mm (A,B,C) and the 0.1 mm collimator (profile of 12 measurements). That allows for a line profile analysis yielding the peak position (and calculation of the corresponding d-spacing) and the FWHM. The d-spacing as a function of the distance from the pin hole is given in Fig. 7-30.

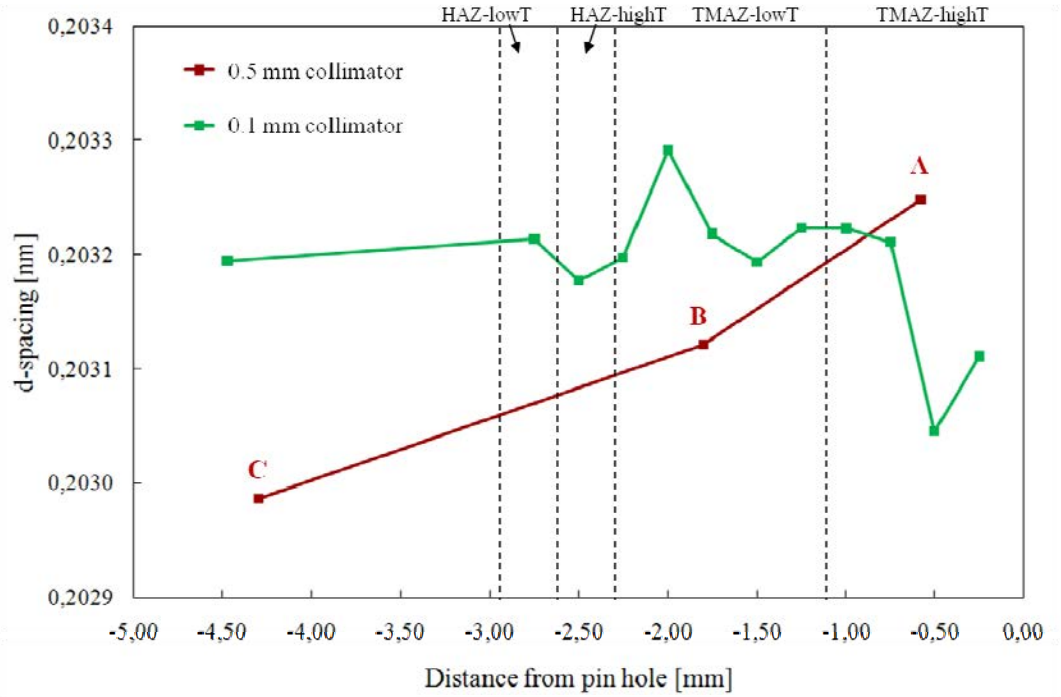

Fig. 7-30. The d-spacing of the (110)α peak as a function of the distance from pin hole.

It is observed that the d-spacing increases on approaching the pin hole, which is most significant from the red curve but the green curve is also slightly increasing towards the pin hole. Furthermore, the green curve experiences a decrease near the edge of pin hole. As mentioned earlier, a shift of peaks is mainly caused by alloying elements, macrostresses and sample displacement. In the BM, the main C-content is present in austenite, and during welding martensite is produced and carbon becomes redistributed to martensite (b.c.c. and b.c.t.). The martensite content increases as approaching the pin hole, and correspondingly the carbon content increase in the b.c.c. phase. This certainly contributes to increased d-spacing on approaching the pin hole (as observed in Fig. 7-30), however, compressive macrostresses will also contribute to increased d-spacing, but the amount of stresses is unknown. Whether the d-spacing shift is caused by the carbon content or macrostresses can only be speculated upon, certainly there is a contribution of both effects. A stress analysis would enable a determination of the contribution of stresses to the shift, but it is not straightforward and was not performed in the present study.

The martensite transformations are associated with volume expansions, which will act on neighboring ferrite. Increased d-spacing of the $(110)_{\alpha}$ plane is a sign of compressive stresses, and it is very likely that the compressive stresses from the martensite volume expansions also contribute to the increased d-spacing in the zones containing martensite (HAZ-highT and the two TMAZs).

On the green curve in Fig. 7-30 there is a peak around -2.0 mm from the pin hole, which cannot directly be related to the EBSD results, which did not show any peculiarity there. The 0.1 mm collimator covers only an area of approximately 0.1 mm, and local inhomogeneities in the microstructure may have caused the peak shift.

The significant decrease of the green curve near the pin hole can be related to the free surface, which can cause stress relaxation (stress gradients) and/or depletion of carbon. Along the pin hole a region of ferrite was observed, which were found to be caused by formation of δ-ferrite, decarburization or both. The possibility of decarburization agrees well with the finding of a decreased d-spacing close to the pinhole.

The FWHM of the $(110)_{\alpha}$ peak as a function of the distance from the pin hole is seen in Fig. 7-31.

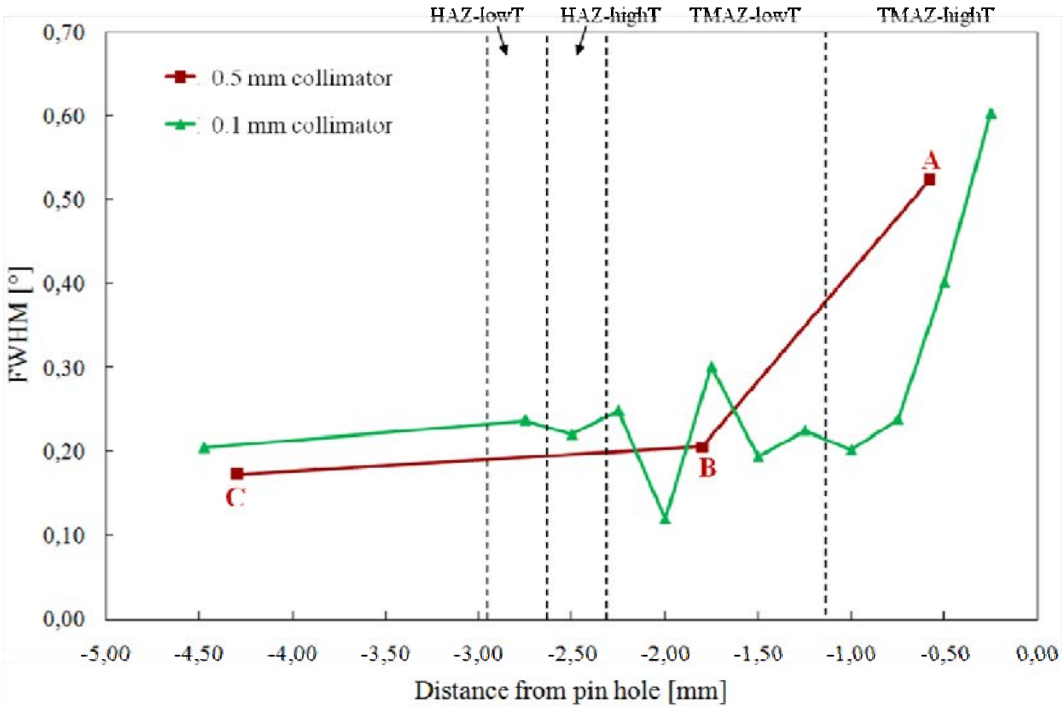

Fig. 7-31. The FWHM of the (110)α peak as a function of the distance from the pin hole.

It is seen that FWHM increases towards the weld center, where the main increase occurs on entering the TMAZ-highT. This trend is seen in both curves and can be related to the microstructure in the various weld zones. Lath martensite contains a large amount of microstrains, and therefore, the increased FWHM is most likely caused by the fully martensitic microstructure in TMAZ-highT. Composition variations also induce microstrains. It was found earlier that the martensite generally attains a b.c.c. lattice and a minor amount of b.c.t.

martensite, as a result of local variations of the carbon content. These carbon inhomogenities in martensite will broadens the peaks. The FWHM is not only affected by microstrains, but also small grains, or more correctly: small, coherently diffracting domains, which will broaden the peaks. Martensite is a structure consisting of packets, blocks and sub-blocks, which will diffract as a fine grained structure in XRD. Therefore, the martensite structure (both b.c.c. and b.c.t.) will contribute to the broadening due to the substructures. The combined influence of both size and strain contributions on peak broadening cannot be separated for the present samples due to the strongly overlapping peaks.

In B, the microstructure contains a considerable amount of martensite and it would be expected to have a greater impact on the FWHM, but it is seen in Fig. 7-31 that the FWHM is only slightly increased in B compared to C. It indicates that only a fully martensitic microstructure is significant for the broadening. The green curve shows scattering near region B, which most likely is caused by inhomogeneities in the microstructure within the measured volume.

7.11 Conclusion

Based on detailed microstructure characterization in Sample 1500-1, it is concluded that the following four zones exists:

- HAZ-lowT - Temp. < Ac_1
- HAZ-highT - Temp = Ac_1 - Ac_3
- TMAZ-lowT - Temp = Ac_1 - Ac_3
- TMAZ-highT - Temp > Ac_3

In the HAZ-lowT zone bainite is developed from retained austenite, similar as the bainite formation applied to TRIP steel in the processing heat treatment. Closest to HAZ-highT, austenite will transform into ferrite instead as a result of the temperature just below Ac_1.

In the HAZ-highT zone the microstructure is exposed to an intercritical temperature range, from where a dual-phase microstructure of ferrite and martensite is developed.

On entering the TMAZ-lowT zone the externally applied deformation appear from rotation gradients within the ferrite grains indicating increased dislocation density. As rotation gradients become larger, subgrain boundaries are developed by dynamic recovery. At higher strain closer to the pin hole, the boundaries increase to become high angle grain boundaries indicating a

transition from dynamic recovery to continuous dynamic recrystallization. On approaching the transition to TMAZ-highT new ferrite grains are developed by strain-induced transformation.

The microstructure is fully martensitic in the TMAZ-highT zone, as a result of the temperature above Ac_3. The carbon content is in-homogeneously distributed throughout the microstructure in the zone.

Along the edge of the pin hole, a region of ferrite has formed, aligned parallel with the pin hole. The ferrite was proposed to originate by either δ-ferrite formation or decarburization, or a combination hereof.

8 Conclusions

The present study has shown that TRIP steel can be successfully joined with friction stir spot welding. The produced welds meet the specifications for automotive spot welds. It is crucial that weld parameters are adjusted in order to improve the quality of the welds. The investigation of weld parameters in the present work suffered from variations in the plunge depth. This was caused by the type of welding machine, which was distance controlled. It is anticipated that force control is most desirable, since it allows a correct adjustment of pin and shoulder in the workpiece.

Lap shear tensile testing was applied for an evaluation of the weld strength. If a detailed study of the mechanical properties of a weld is wanted, further mechanical tests must be performed, e.g. cross sectional shear test, uniaxial tensile tests and Erichsen deformation tests, whereby the strength, ductility and fracture toughness can be determined. In the present study, the main focus was on investigating and understanding the microstructural evolution occurring during FSSW.

For cross section characterization, reflected light microscopy (RLM) of Nital-etched samples was successfully applied for a macroscopic investigation of the weld zone that had developed, and combined with hardness measurements along a line over the welded region. RLM was also useful for the identification of defects (if any) in the weld, and for an analysis of the material flow that had occurred during welding. The most important observation is the assessment of the bonding ligament between the two joined sheets. The bonding ligament width is the distance over which the joint bridges, and determines the strength of the weld. It is expected that substantial improvement in the strength can be achieved if the bonding ligament width by focusing on an optimization of weld parameters and/or the tool geometry. However, also the microstructure in the region of the bonding ligament was found to be crucial for the strength. In a detailed analysis of the microstructure in the strongest welds, it was found that a fully martensitic microstructure was present in the bonding ligament region; this was obtained for tool

rotations above 1000 rpm. Therefore, it is recommended to focus future development on increasing the width of the fully martensitic zone so it always covers the bonding ligament. There is also an indication that the production of fine ferrite grains by strain-induced transformation in the transition between the two TMAZs has a substantial effect on the quality of the welds by providing a more gradual behavior of the hardness (and thereby a distribution of the stresses) between the zones. The TRIP effect is not preserved throughout the welded zone as austenite is not retained during welding.

The combined result of the lap shear tensile test, microhardness measurements and macroscopic RLM characterization, indicated one best sample among the entire amount of samples welded. The sample was welded by a combination of 1500 rpm and 1 second of dwell time. The sample was applied for a thorough microstructure characterization, in order to understand the microstructure evolution occurring during welding.

In the characterization of TRIP steel base material it was found that the complementary use of RLM, SEM and EBSD allows the identification of all micro-constituents in the multiphase microstructure. For RLM etching with Modified LePera is recommended. Identification of bainite can be done according to its morphology, and both RLM, SEM and EBSD can be used for this. However, the identification of austenite in the lamellae of bainite is only reliable with EBSD analysis, because it is based on crystallographic information. Austenite in the remaining microstructure must be identified with EBSD because the identification on the basis of RLM and SEM only is ambiguous. Martensite can be identified by all three techniques, but also for this phase, EBSD is preferred since the colors in RLM micrographs can be misleading, and the lamellar structure as observed in SEM is not always visible. Therefore, EBSD is recommended for the unambiguous identification of all micro-constituents, and SEM and RLM contribute by providing overview over a larger region.

The characterization of Sample 1500-1 was performed mainly with EBSD and hardness measurements, but also RLM and SEM were used. The characterization was performed at the same location of the weld with all techniques; along a line in the upper sheet parallel to the surface, at a depth of 200-300 μm from upper surface. This allowed a direct comparison of the results. Certainly, hardness measurements should be performed on separate samples or samples should be re-polished to remove hardness indentations before microscopy, while the indentations will affect the microstructure.

The detailed characterization revealed a division of the welded region into four welded zones; two thermo-mechanically affected zones (TMAZs) and two heat affected zones (HAZs). The designation stir zone (SZ), as used in friction stir welding, is considered not useful for FSSW of steel because the division into TMAZs better describes the occurring microstructural changes. The identification of zones can be done primarily by observing the hardness and the area fraction of martensite and austenite as can be supplied by microstructure observations. Despite the fact that FSSW applies a combined action of deformation and temperature, the individual effects of the two factors were identified in the microstructure. The initial thermal impact is observed by a

reduced hardness and austenite content, as a result of austenite transformation. The initial deformation is observed as rotation of the lattice in ferrite grains, which increases upon larger deformation. The transition between the HAZ and TMAZ is not easily identified because the initiated rotations of ferrite grains are very small. A few methods were suggested for determination of the initial deformation in EBSD maps. For this purpose low angle KAM coloring, coarsening of the datasets and drawing of misorientation lines were demonstrated to be useful procedures.

The separation between zones can be applied for the characterization of samples welded by other parameters, where the effect of temperature and deformation is different on applying knowledge from Sample 1500-1. Furthermore, the formation of the four zones is expected to occur in other low alloyed, low carbon steels, as a result of their comparable composition with the TRIP steel investigated in the present study. In the low temperature HAZ the transformations may be slightly different if there is no austenite in the initial microstructure, but in the other three zones, a similar behavior would be expected.

The results from the investigations of the individual effects of heat and deformation were useful for understanding the microstructure evolution during welding.

9 Outlook

In the present study the weld parameter study was constrained by the use of a distance control welding machine, which induced a large variation in the plunge depths. Therefore, it would be highly recommended to perform a parameter study on a force controlled welding machine, in order to optimize the parameters. Besides variation of the rotational speed and dwell time, also plunge rate would be of interest to investigate.

As found for Sample 1500-1, development of ferrite by SIT appears to be beneficial for the properties of the weld, because the transition between high and low hardness occurs more gradual in the TMAZ-lowT zone. Therefore, for further development of FSSW in TRIP steel, it is recommended to adjust weld parameters to promote the formation of ferrite by SIT. The exact conditions for SIT during FSSW are not known but most likely at highest possible strain.

The corrosion resistance of the present TRIP steel relies on the Zn coating, which is removed during welding. Accordingly, the corrosion protection is destroyed. It would of interest to investigate the severity of the removal of the coating, as well as developing a method or coating to overcome the problems, which may arise by the lack of the Zn coating.

In the automotive industry the potential of using TRIP steels is high due to the excellent properties compared to other high strength steels. In any application in a vehicle where TRIP steel is expected to be inserted it has to be joined with other materials, serving other needs in the body structure of the vehicle. Therefore, the TRIP-TRIP joint is not of large commercial interest and other joining configurations must be considered. A suggestion for a future continuation of the work is to investigate other material combinations with TRIP steel in order to accomplish this need from the industry.

10 References

[1] A. K. Sinha, *Physical Metallurgy Handbook*. McGraw-Hill Professional, 2002.

[2] S. Keeler, "Advanced High Strength Steel (AHSS) Application Guidelines v. 4.1." World Auto Steel, 2009.

[3] T. Senuma, "Physical Metallurgy of Modern High Strength Steel Sheets," *ISIJ International*, vol. 41, no. 6, pp. 520-532, 2001.

[4] E. Girault et al., "Metallographic Methods for Revealing the Multiphase Microstructure of TRIP-Assisted Steels," *Materials Characterization*, vol. 40, no. 2, pp. 111-118, 1998.

[5] P. J. Jacques, "Transformation-induced plasticity for high strength formable steels," *Current Opinion in Solid State & Materials Science*, vol. 8, no. 3-4, pp. 259-265, 2004.

[6] J. G. Speer, F. C. R. Assunção, D. K. Matlock, and D. V. Edmonds, "The 'quenching and partitioning' process: background and recent progress," *Materials Research*, vol. 8, pp. 417-423, 2005.

[7] E. Girault, A. Mertens, P. Jacques, Y. Houbaert, B. Verlinden, and J. Van Humbeeck, "Comparison of the effects of silicon and aluminium on the tensile behaviour of multiphase TRIP-assisted steels," *Scripta Materialia*, vol. 44, no. 6, pp. 885-892, 2001.

[8] S. Zaefferer, J. Ohlert, and W. Bleck, "A study of microstructure, transformation mechanisms and correlation between microstructure and mechanical properties of a low alloyed TRIP steel," *Acta Materialia*, vol. 52, no. 9, pp. 2765-2778, 2004.

[9] B. Hutchinson, L. Ryde, E. Lindh, and K. Tagashira, "Texture in hot rolled austenite and resulting transformation products," *Materials science & engineering. A, Structural materials: properties, microstructure and processing*, vol. 257, no. 1, pp. 9-17, 1998.

[10] M. J. Santofimia, L. Zhao, and J. Sietsma, "Microstructural Evolution of a Low-Carbon Steel during Application of Quenching and Partitioning Heat Treatments after Partial Austenitization," *Metallurgical and Materials Transactions A*, vol. 40, no. 1, pp. 46-57, 2009.

[11] H. B. Ryu, J. G. Speer, and J. P. Wise, "Effect of thermomechanical processing on the retained austenite content in a Si-Mn transformation-induced-plasticity steel," *Metallurgical and Materials Transactions A*, vol. 33, no. 9, pp. 2811–2816, 2002.

[12] A. Basuki and E. Aernoudt, "Influence of rolling of TRIP steel in the intercritical region on the stability of retained austenite," *Journal of Materials Processing Technology*, vol. 89, pp. 37–43, 1999.

[13] P. Cizek, B. P. Wynne, C. H. . Davies, B. C. Muddle, and P. D. Hodgson, "Effect of composition and austenite deformation on the transformation characteristics of low-carbon and ultralow-carbon microalloyed steels," *Metallurgical and Materials Transactions A*, vol. 33, no. 5, pp. 1331–1349, 2002.

[14] D. N. Hanlon, J. Sietsma, and S. Zwaag, "The effect of plastic deformation of austenite on the kinetics of subsequent ferrite formation," *ISIJ international*, vol. 41, no. 9, pp. 1028–1036, 2001.

[15] J. Jung, H. Kim, and B. C. De Cooman, "Yielding Behavior of Nb Micro-alloyed C–Mn–Si TRIP Steel Studied by In-situ Synchrotron X-ray Diffraction," *ISIJ International*, vol. 50, no. 4, pp. 620–629, 2010.

[16] F. D. Fischer, G. Reisner, E. Werner, K. Tanaka, G. Cailletaud, and T. Antretter, "A new view on transformation induced plasticity (TRIP)," *International Journal of Plasticity*, vol. 16, no. 7-8, pp. 723-748, 2000.

[17] M. De Meyer, D. Vanderschueren, and B. C. . Cooman, "The influence of the substitution of Si by Al on the properties of cold rolled C-Mn-Si TRIP steels," *ISIJ International*, vol. 39, no. 8, pp. 813–822, 1999.

[18] S. J. Kim, C. G. Lee, I. Choi, and S. Lee, "Effects of heat treatment and alloying elements on the microstructures and mechanical properties of 0.15 wt pct C transformation-induced plasticity-aided cold-rolled steel sheets," *Metallurgical and Materials Transactions A*, vol. 32, no. 3, pp. 505–514, 2001.

[19] T. Hanamura, S. Torizuka, A. Sunahara, M. Imagumbai, and H. Takechi, "Excellent Total Mechanical-Properties-Balance of 5% Mn, 30000 MPa% Steel," *ISIJ International*, vol. 51, no. 4, pp. 685-687, 2011.

[20] S.-J. Park, C.-S. Oh, and S.-J. Kim, "Microstructure and Mechanical Properties of a TRIP Steel Containing 7 Mass% Mn," in *Advanced Steels*, Y. Weng, H. Dong, and Y. Gan, Eds. Berlin, Heidelberg: Springer Berlin Heidelberg, 2011, pp. 275-278.

[21] P. Jacques, F. Delannay, X. Cornet, P. Harlet, and J. Ladriere, "Enhancement of the mechanical properties of a low-carbon, low-silicon steel by formation of a multiphased microstructure containing retained Austenite," *Metallurgical and Materials Transactions A*, vol. 29, no. 9, pp. 2383-2393, 1998.

[22] H. C. Chen, H. Era, and M. Shimizu, "Effect of phosphorus on the formation of retained austenite and mechanical properties in Si-containing low-carbon steel sheet," *Metallurgical and Materials Transactions A*, vol. 20, no. 3, pp. 437–445, 1989.

[23] P. J. Jacques, Q. Furnémont, F. Lani, T. Pardoen, and F. Delannay, "Multiscale mechanics of TRIP-assisted multiphase steels: I. Characterization and mechanical testing," *Acta Materialia*, vol. 55, no. 11, pp. 3681-3693, 2007.

[24] Q. Furnémont, M. Kempf, P. J. Jacques, M. Göken, and F. Delannay, "On the measurement of the nanohardness of the constitutive phases of TRIP-assisted multiphase steels," *Materials Science & Engineering A*, vol. 328, no. 1-2, pp. 26-32, 2002.

[25] M. I. Khan, M. L. Kuntz, A. Biro, and Y. Zhou, "Microstructure and Mechanical Properties of Resistance Spot Welded Advanced High Strength Steels," *Materials Transactions*, vol. 49, no. 7, pp. 1629-1637, 2008.

[26] C.-Y. Kang, T.-K. Han, B.-K. Lee, and J.-K. Kim, "Characteristics of Nd:YAG Laser Welded 600 MPa Grade TRIP and DP Steels," *Materials Science Forum*, vol. 539-543, pp. 3967-3972, 2007.

[27] M. Amirthalingam, M. Hermans, and I. Richardson, "Microstructural Development during Welding of Silicon-and Aluminum-Based Transformation-Induced Plasticity Steels---Inclusion and Elemental Partitioning Analysis," *Metallurgical and Materials Transactions A*, vol. 40, no. 4, pp. 901-909, 2009.

[28] M. Amirthalingam, M. J. M. Hermans, and I. M. Richardson, “Microstructural Evolution during Gas Tungsten Arc, Laser and Resistance Spot Welding of Al-Containing Transformation Induced Plasticity (TRIP) Steel,” *Advanced Materials Research*, vol. 89, pp. 23–28, 2010.
[29] M. Amirthalingam, M. J. M. Hermans, L. Zhao, and I. M. Richardson, “Quantitative Analysis of Microstructural Constituents in Welded Transformation-Induced-Plasticity Steels,” *Metallurgical and Materials Transactions A*, vol. 41, no. 2, pp. 431–439, 2010.
[30] Y. Peng, Y. Qi, C. He, Z. Tian, and H. Xiao, “Microstructure and Its Formation Mechanism of Weld Metal of Al-bearing TRIP Steel,” in *Materials science forum*, 2010, vol. 638, pp. 3591–3596.
[31] T. K. Han, S. S. Park, K. H. Kim, C. Y. Kang, I. S. Woo, and J. B. Lee, “CO2 Laser Welding Characteristics of 800 MPa Class TRIP Steel,” *ISIJ international*, vol. 45, no. 1, pp. 60–65, 2005.
[32] T. Kim, H. Park, and S. Rhee, “Optimization of welding parameters for resistance spot welding of TRIP steel with response surface methodology,” *International Journal of Production Research*, vol. 43, no. 21, pp. 4643–4657, 2005.
[33] L. Cretteur, A. Koruk, and L. Tosal-Martinez, “Improvement of weldability of TRIP steels by use of in-situ pre- and post-heat treatments,” *Steel research*, vol. 73, no. 6-7, pp. 314-319, 2002.
[34] G. Shi and S. Westgate, “Techniques for improving the weldability of TRIP steel using resistance spot welding,” *TWI Research Reports*, vol. 798, 2004.
[35] T. B. Hilditch, J. G. Speer, and D. K. Matlock, “Effect of susceptibility to interfacial fracture on fatigue properties of spot-welded high strength sheet steel,” *Materials and Design*, vol. 28, no. 10, pp. 2566–2576, 2007.
[36] American welding society, “Specification for automotive weld quality - resistance spot welding of steel, AWS D8.1M:2007.” 2007.
[37] R. W. Rathbun, D. K. Matlock, and J. G. Speer, “Fatigue Behavior of Spot Welded High-Strength Sheet Steels.,” *Welding Journal*, vol. 82, no. 8, pp. 207–218, 2003.
[38] R. Ohashi, M. Fujimoto, S. Mironov, Y. S. Sato, and H. Kokawa, “Effect of contamination on microstructure in friction stir spot welded DP590 steel,” *Science and Technology of Welding and Joining*, vol. 14, no. 3, p. 221, 2009.
[39] M. I. Khan, M. L. Kuntz, P. Su, A. Gerlich, T. North, and Y. Zhou, “Resistance and friction stir spot welding of DP600: a comparative study,” *Science and Technology of Welding & Joining*, vol. 12, no. 2, pp. 175-182, 2007.
[40] Z. Feng et al., “Friction Stir Spot Welding of advanced high-strength steels-a feasibility study,” 2005.
[41] M. P. Miles, J. Pew, T. W. Nelson, and M. Li, “Comparison of formability of friction stir welded and laser welded dual phase 590 steel sheets,” *Science and Technology of Welding & Joining*, vol. 11, pp. 384-388, Jul. 2006.
[42] M. P. Miles, T. W. Nelson, R. Steel, E. Olsen, and M. Gallagher, “Effect of friction stir welding conditions on properties and microstructures of high strength automotive steel,” *Science and Technology of Welding &# 38; Joining*, vol. 14, no. 3, pp. 228-232, 2009.
[43] C. Mazzaferro, “FSSW of TRIP 800; process, microstructure and properties,” Ph.D thesis, Universidade Federal Do Rio Grande Do Sul, 2008.
[44] R. S. Mishra and Z. Y. Ma, “Friction stir welding and processing,” *Materials Science & Engineering R*, vol. 50, no. 1-2, pp. 1-78, 2005.
[45] D. Bakavos and P. B. Prangnell, “Effect of reduced or zero pin length and anvil insulation on friction stir spot welding thin gauge 6111 automotive sheet,” *Science and Technology of Welding &# 38; Joining*, vol. 14, no. 5, pp. 443–456, 2009.

[46] W. M. Thomas, E. D. Nicholas, J. C. Needham, M. G. Murch, P. Temple-Smith, and C. J. Dawes, "International patent application PCT/GB92/02203 and GB patent application 9125978.8," *UK Patent Office, London*, 1991.
[47] R. S. Mishra and M. W. Mahoney, *Friction Stir Welding and Processing*. ASM International, 2007.
[48] R. Nandan, T. DebRoy, and H. Bhadeshia, "Recent advances in friction-stir welding–Process, weldment structure and properties," *Progress in Materials Science*, 2008.
[49] C. Y. Lee, D. H. Choi, Y. M. Yeon, and S. B. Jung, "Dissimilar friction stir spot welding of low carbon steel and AlMg alloy by formation of IMCs," *Science and Technology of Welding &# 38; Joining*, vol. 14, no. 3, pp. 216-220, 2009.
[50] R. S. Coelho, A. Kostka, S. Sheikhi, J. dos Santos, and A. R. Pyzalla, "Microstructure and Mechanical Properties of an AA6181-T4 Aluminium Alloy to HC340LA High Strength Steel Friction Stir Overlap Weld," *Advanced Engineering Materials*, vol. 10, no. 10, pp. 961-972, 2008.
[51] R. S. Coelho, A. Kostka, J. dos Santos, and A. R. Pyzalla, "EBSD Technique Visualization of Material Flow in Aluminum to Steel Friction-stir Dissimilar Welding," *Advanced Engineering Materials*, vol. 10, no. 12, pp. 1127-1133, 2009.
[52] P. Cavaliere, E. Cerri, L. Marzoli, and J. Dos Santos, "Friction stir welding of ceramic particle reinforced aluminium based metal matrix composites," *Applied Composite Materials*, vol. 11, no. 4, pp. 247–258, 2004.
[53] J. A. Wert, "Microstructures of friction stir weld joints between an aluminium-base metal matrix composite and a monolithic aluminium alloy," *Scripta materialia*, vol. 49, no. 6, pp. 607–612, 2003.
[54] W. M. Thomas, P. L. Threadgill, and E. D. Nicholas, "Feasibility of friction stir welding steel," *Science and Technology of Welding & Joining*, vol. 4, no. 6, pp. 365-372, 1999.
[55] R. Ueji, H. Fujii, L. Cui, A. Nishioka, K. Kunishige, and K. Nogi, "Friction stir welding of ultrafine grained plain low-carbon steel formed by the martensite process," *Materials Science and Engineering: A*, vol. 423, no. 1-2, pp. 324-330, May 2006.
[56] H. Fujii, L. Cui, M. Maeda, and K. Nogi, "Effect of tool shape on mechanical properties and microstructure of friction stir welded aluminum alloys," *Materials Science & Engineering A*, vol. 419, no. 1-2, pp. 25-31, 2006.
[57] H. Fujii, L. Cui, N. Tsuji, M. Maeda, K. Nakata, and K. Nogi, "Friction stir welding of carbon steels," *Materials Science & Engineering A*, vol. 429, no. 1-2, pp. 50-57, 2006.
[58] A. Al-Shahrani and B. P. Wynne, "Effect of Dwell Time on Friction Stir Spot Welded Dual Phase Steel," *Advanced Materials Research*, vol. 83, pp. 1143–1150, 2010.
[59] S. Bozzi, A. L. Etter, T. Baudin, A. Robineau, and J. C. Goussain, "Mechanical behaviour and microstructure of aluminum-steel sheets joined by FSSW," *Texture, Stress and Microstructure*, vol. 2008, no. 360617, pp. 1-8, 2008.
[60] H. Huh and W. J. Kang, "Electrothermal analysis of electric resistance spot welding processes by a 3-D finite element method," *Journal of Materials Processing Technology*, vol. 63, no. 1-3, pp. 672-677, Jan. 1997.
[61] S. Klingensmith, J. N. Du Pont, and A. Marder, "Microstructural Characterization of a Double-Sided Friction Stir Weld on a Superaustenitic Stainless Steel," *Welding journal*, vol. 84, no. 5, pp. 77-85, 2005.
[62] T. J. Lienert, W. L. Stellwag Jr, B. B. Grimmett, and R. W. Warke, "Friction Stir Welding Studies on Mild Steel," *Welding Journal*, vol. 82, no. 1, p. 1, 2003.
[63] Y. Hovanski, M. L. Santella, and G. J. Grant, "Friction stir spot welding of hot-stamped boron steel," *Scripta Materialia*, vol. 57, no. 9, pp. 873-876, 2007.

[64] S. H. C. Park, Y. S. Sato, H. Kokawa, K. Okamoto, S. Hirano, and M. Inagaki, "Microstructure of Friction-Stir-Welded High-Nitrogen Stainless Steel," *Materials Science Forum*, vol. 539-543, pp. 3757-3762, 2007.

[65] P. Su, A. Gerlich, T. H. North, and G. J. Bendzsak, "Intermixing in Dissimilar Friction Stir Spot Welds," *Metallurgical and Materials Transactions A*, vol. 38, no. 3, pp. 584-595, Mar. 2007.

[66] M. Guerra, C. Schmidt, J. C. McClure, L. E. Murr, and A. C. Nunes, "Flow patterns during friction stir welding," *Materials characterization*, vol. 49, no. 2, pp. 95-101, 2002.

[67] Q. Yang, S. Mironov, Y. S. Sato, and K. Okamoto, "Material flow during friction stir spot welding," *Materials Science and Engineering: A*, vol. 527, no. 16-17, pp. 4389–4398, 2010.

[68] A. Simar et al., "A multiscale multiphysics investigation of aluminum friction stir welds," *Phd Thesis*.

[69] Y. D. Chung, H. Fujii, R. Ueji, and K. Nogi, "Friction stir welding of hypereutectoid steel (SK5) below eutectoid temperature," *Science and Technology of Welding & Joining*, vol. 14, no. 3, pp. 233-238, 2009.

[70] Y. S. Sato, H. Yamanoi, H. Kokawa, and T. Furuhara, "Microstructural evolution of ultrahigh carbon steel during friction stir welding," *Scripta Materialia*, vol. 57, no. 6, pp. 557-560, 2007.

[71] S. H. C. Park, Y. S. Sato, H. Kokawa, K. Okamoto, S. Hirano, and M. Inagaki, "Rapid formation of the sigma phase in 304 stainless steel during friction stir welding," *Scripta Materialia*, vol. 49, no. 12, pp. 1175-1180, 2003.

[72] T. Weinberger, N. Enzinger, and H. Cerjak, "Microstructural and mechanical characterisation of friction stir welded 15-5PH steel," *Science and Technology of Welding &# 38; Joining*, vol. 14, no. 3, pp. 210-215, 2009.

[73] H. Fujii et al., "Friction Stir Welding of Ultrafine Grained Interstitial Free Steels," *Materials Transactions*, vol. 47, no. 1, p. 239, 2006.

[74] Y. S. Sato, T. W. Nelson, C. J. Sterling, R. J. Steel, and C. O. Pettersson, "Microstructure and mechanical properties of friction stir welded SAF 2507 super duplex stainless steel," *Materials Science & Engineering A*, vol. 397, no. 1-2, pp. 376-384, 2005.

[75] M. Ghosh, K. Kumar, and R. S. Mishra, "Analysis of microstructural evolution during friction stir welding of ultra high strength steel," *Scripta Materialia*, 2010.

[76] S. Nemecek, Z. Novy, and H. Stankova, "Optimization heat treatment of TRIP steels," *Metallurgia Italiana*, pp. 47-51, 2006.

[77] A. K. Lis and B. Gajda, "Modelling of the DP and TRIP microstructure in the CMnAlSi automotive steel," *Journal of Achievements in Materials and Manufacturing Engineering*, vol. 15, no. 1-2, 2006.

[78] I. B. Timokhina, P. D. Hodgson, and E. V. Pereloma, "Effect of microstructure on the stability of retained austenite in transformation-induced-plasticity steels," *Metallurgical and Materials Transactions A*, vol. 35, no. 8, pp. 2331–2341, 2004.

[79] S. Cheng, X. L. Wang, Z. Feng, B. Clausen, H. Choo, and P. K. Liaw, "Probing the Characteristic Deformation Behaviors of Transformation-Induced Plasticity Steels," *Metallurgical and Materials Transactions A*, vol. 39, no. 13, pp. 3105–3112, 2008.

[80] J. Wang and S. Van Der Zwaag, "Stabilization mechanisms of retained austenite in transformation-induced plasticity steel," *Metallurgical and Materials Transactions A*, vol. 32, no. 6, pp. 1527–1539, 2001.

[81] P. J. Jacques et al., "On measurement of retained austenite in multiphase TRIP steels results of blind round robin test involving six different techniques," *Materials Science and Technology*, vol. 25, no. 5, pp. 567-574, 2009.

[82] P. J. Jacques, J. Ladriere, F. Delannay, and others, "On the influence of interactions between phases on the mechanical stability of retained austenite in transformation-induced plasticity multiphase steels," *Metallurgical and Materials Transactions A*, vol. 32, no. 11, pp. 2759–2768, 2001.

[83] D. Q. Bai, A. Di Chiro, and S. Yue, "Stability of retained austenite in a Nb microalloyed Mn-Si TRIP steel," in *Materials Science Forum*, 1998, pp. 253–260.

[84] M. Wakita, Y. Adachi, and Y. Tomota, "Crystallography and mechanical properties of ultrafine trip-aided multi-phase steels," in *Materials science forum*, 2007, vol. 539, p. 4351.

[85] E. V. Pereloma, I. B. Timokhina, and P. D. Hodgson, "Transformation behaviour in thermomechanically processed C-Mn-Si TRIP steels with and without Nb," *Materials Science and Engineering A*, vol. 273-275, pp. 448-452, Dec. 1999.

[86] E. Jimenez-Melero et al., "Martensitic transformation of individual grains in low-alloyed TRIP steels," *Scripta Materialia*, vol. 56, no. 5, pp. 421-424, 2007.

[87] S. Kruijver et al., "In situ observations on the austenite stability in TRIP-steel during tensile testing," *Steel Research*, vol. 73, no. 6, pp. 236-241, 2002.

[88] K. K. Park et al., "In situ deformation behavior of retained austenite in TRIP steel," in *Materials Science Forum*, 2002, vol. 408, pp. 571-576.

[89] A. Itami, M. Takahashi, and K. Ushioda, "Plastic stability of retained austenite in the cold-rolled 0.14% C-1.9% Si-1.7% Mn sheet steel," *ISIJ International*, vol. 35, no. 9, pp. 1121-1127, 1995.

[90] A. Wasilkowska et al., "Microstructure and Texture Changes in a Low-alloyed TRIP-aided Steel Induced by Small Plastic Deformation," *ISIJ International*, vol. 46, no. 2, pp. 302-309, 2006.

[91] L. Zhao, N. M. van der Pers, J. Sietsma, and S. van der Zwaag, "In Situ X-Ray Diffraction Measurements of Deformation-Induced Austenite to Martensite Transformation in a Multiphase TRIP Steel," in *Materials Science Forum*, 2005, vol. 500, pp. 379–386.

[92] R. Song, D. Ponge, D. Raabe, J. G. Speer, and D. K. Matlock, "Overview of processing, microstructure and mechanical properties of ultrafine grained bcc steels," *Materials Science and Engineering: A*, vol. 441, no. 1-2, pp. 1–17, 2006.

[93] M. Calcagnotto, D. Ponge, and D. Raabe, "Ultrafine Grained Ferrite/Martensite Dual Phase Steel Fabricated by Large Strain Warm Deformation and Subsequent Intercritical Annealing," *ISIJ International*, vol. 48, no. 8, pp. 1096-1101, 2008.

[94] R. E. Smallman and R. J. Bishop, *Modern physical metallurgy and materials engineering: science, process, applications*, 6th ed. Butterworth-Heinemann, 1999.

[95] L. Longfei, Y. Wangyue, and S. Zuqing, "Dynamic recrystallization of ferrite in a low-carbon steel," *Metallurgical and Materials Transactions A*, vol. 37, no. 3, pp. 609–619, 2006.

[96] R. Song, D. Ponge, and D. Raabe, "Mechanical properties of an ultrafine grained C-Mn steel processed by warm deformation and annealing," *Acta Materialia*, vol. 53, no. 18, pp. 4881-4892, Oct. 2005.

[97] F. J. Humphreys and M. Hatherly, *Recrystallization and related annealing phenomena*. Pergamon, 2004.

[98] R. Wang and T. C. Lei, "Substructural Evolution of Ferrite in a Low Carbon Steel During Hot Deformation in(F+ A) Two-Phase Range," *Scripta Metallurgica et Materialia(USA)*, vol. 28, no. 5, pp. 629–632, 1993.

[99] R. Z. Wang and T. C. Lei, "Dynamic recrystallization of ferrite in a low carbon steel during hot rolling in the (F+ A) two-phase range," *Scripta Metallurgica et Materialia*, vol. 31, no. 9, pp. 1193–1196, 1994.

[100] R. Song, D. Ponge, D. Raabe, and R. Kaspar, “Microstructure and crystallographic texture of an ultrafine grained C-Mn steel and their evolution during warm deformation and annealing,” *Acta materialia*, vol. 53, no. 3, pp. 845–858, 2005.
[101] A. Smith, H. Luo, D. N. Hanlon, J. Sietsma, and S. Zwaag, “Recovery processes in the ferrite phase in C-Mn steel,” *ISIJ international*, vol. 44, no. 7, pp. 1188–1194, 2004.
[102] B. Eghbali and A. Abdollah-Zadeh, “Strain-induced transformation in a low carbon microalloyed steel during hot compression testing,” *Scripta materialia*, vol. 54, no. 6, pp. 1205–1209, 2006.
[103] B. Eghbali, A. Abdollah-Zadeh, H. Beladi, and P. Hodgson, “Characterization on ferrite microstructure evolution during large strain warm torsion testing of plain low carbon steel,” *Materials Science and Engineering: A*, vol. 435, pp. 499–503, 2006.
[104] R. Pandi and S. Yue, “Dynamic transformation of austenite to ferrite in low carbon steel,” *ISIJ international*, vol. 34, no. 3, pp. 270–279, 1994.
[105] P. J. Hurley, B. C. Muddle, and P. D. Hodgson, “The production of ultrafine ferrite during hot torsion testing of a 0.11 wt pct C steel,” *Metallurgical and Materials Transactions A*, vol. 33, no. 9, pp. 2985–2993, 2002.
[106] G. L. Kelly, H. Beladi, and P. D. Hodgson, “Ultrafine grained ferrite formed by interrupted hot torsion deformation of plain carbon steel,” *ISIJ international*, vol. 42, no. 12, pp. 1585–1590, 2002.
[107] J. K. Choi, D. H. Seo, J. S. Lee, K. K. Um, and W. Y. Choo, “Formation of ultrafine ferrite by strain-induced dynamic transformation in plain low carbon steel,” *ISIJ international*, vol. 43, no. 5, pp. 746–754, 2003.
[108] Y. D. Huang, W. Y. Yang, and Z. Q. Sun, “Formation of ultrafine grained ferrite in low carbon steel by heavy deformation in ferrite or dual phase region,” *Journal of Materials Processing Technology*, vol. 134, no. 1, pp. 19–25, 2003.
[109] B. Eghbali and A. Abdollah-Zadeh, “Influence of deformation temperature on the ferrite grain refinement in a low carbon Nb-Ti microalloyed steel,” *Journal of Materials Processing Technology*, vol. 180, no. 1-3, pp. 44–48, 2006.
[110] P. J. Hurley, B. C. Muddle, and P. D. Hodgson, “Nucleation sites for ultrafine ferrite produced by deformation of austenite during single-pass strip rolling,” *Metallurgical and Materials Transactions A*, vol. 32, no. 6, pp. 1507–1517, 2001.
[111] H. Beladi, I. B. Timokhina, S. Mukherjee, and P. D. Hodgson, “Ultrafine ferrite formation through isothermal static phase transformation,” *Acta Materialia*, 2011.
[112] H. Beladi, G. L. Kelly, and P. D. Hodgson, “Ultrafine grained structure formation in steels using dynamic strain induced transformation processing,” *International materials reviews*, vol. 52, no. 1, pp. 14–28, 2007.
[113] S. C. Hong, S. H. Lim, K. J. Lee, D. H. Shin, and K. S. Lee, “Effect of undercooling of austenite on strain induced ferrite transformation behavior,” *ISIJ international*, vol. 43, no. 3, pp. 394–399, 2003.
[114] J. J. Jonas and V. V. Basabe, “Ferrite Formation Above the Ae_3 in a Medium-Carbon Steel,” *Solid State Phenomena*, vol. 172-174, pp. 372-377, Jun. 2011.
[115] P. J. Hurley, B. C. Muddle, and P. D. Hodgson, “Microstructure and microtexture of ultrafine ferrite formed in 0.1 C steel using new strip rolling process,” *Materials Science and Technology, 16*, vol. 11, no. 12, pp. 1376–1379, 2000.
[116] P. J. Hurley and P. D. Hodgson, “Formation of ultra-fine ferrite in hot rolled strip: potential mechanisms for grain refinement,” *Materials Science and Engineering A*, vol. 302, no. 2, pp. 206–214, 2001.

[117] Y. Adachi, T. Tomida, and S. Hinotani, "Dislocation Substructures in Hot-deformed Ni-based Alloys: Simulation for Structure Evolution of Hot-worked Austenite in Low Carbon Steels," *ISIJ International*, vol. 40, no. Suppl, pp. 194–198, 2000.
[118] R. K. Ray, J. J. Jonas, M. P. Butron-Guillen, and J. Savoie, "Transformation textures in steels (Review)," *ISIJ International-Iron and Steel Institute of Japan*, vol. 34, no. 12, pp. 927–942, 1994.
[119] S. C. Hong and K. S. Lee, "Influence of deformation induced ferrite transformation on grain refinement of dual phase steel," *Materials Science and Engineering A*, vol. 323, no. 1-2, pp. 148-159, Jan. 2002.
[120] J. Baczynski and J. J. Jonas, "Texture development during the torsion testing of [alpha]-iron and two IF steels," *Acta Materialia*, vol. 44, no. 11, pp. 4273-4288, Nov. 1996.
[121] S. Li, I. J. Beyerlein, and M. A. M. Bourke, "Texture formation during equal channel angular extrusion of fcc and bcc materials: comparison with simple shear," *Materials Science and Engineering A*, vol. 394, no. 1-2, pp. 66-77, Mar. 2005.
[122] R. K. Ray, M. P. Butron-Guillen, J. J. Jonas, and G. E. Ruddle, "Effect of Controlled Rolling on Texture Development in a Plain Carbon and a Nb Microalloyed Steel," *ISIJ international*, vol. 32, no. 2, pp. 203–212, 1992.
[123] U. Fischer, *Tabellenbuch Metall.*, vol. 41. Europa-Lehrmittel Nourney, 2001.
[124] A. J. Schwartz, *Electron Backscatter Diffraction in Materials Science, 2nd Ed.*, 2nd ed. Springer.
[125] S. Oliver, T. B. Jones, and G. Fourlaris, "Dual phase versus TRIP strip steels: comparison of dynamic properties for automotive crash performance," *Materials Science and Technology*, vol. 23, no. 4, pp. 423-431, 2007.
[126] A. K. De, J. G. Speer, and D. K. Matlock, "Color tint-etching for multiphase steels," *Advanced Materials and Processes*, vol. 161, no. 2, pp. 27-30, Feb. 2003.
[127] T. Lyman, *Metals Handbook, Volume 7*. American Society for Metals, 1972.
[128] G. F. V. Voort, *Metallography, principles and practice*. ASM International, 1984.
[129] F. LePera, "Improved Ethcing Technique to Emphasize Martensite and Bainite in High-Strength Dual-Phase Steels," *Journal of Metals*, Mar. 1980.
[130] A. Barcellona, L. Cannizzaro, and D. Palmeri, "Microstructural Characterization of Thermo-Mechanical Treated TRIP Steels," *Key Engineering Materials*, vol. 344, pp. 71-78, 2007.
[131] E. Weck and E. Leistner, *Metallographic instructions for colour etching by immersion. Part II: Beraha colour etchants and their different variants.* Deutcher Verlag für Schweisstechnik (DVS) GmbH, 1983.
[132] ASTM International, "ASTM Standard E 975 - 03." ASTM International, United States, 2000.
[133] E. Miyoshi, T. Kunitake, T. Okada, and T. Katou, "The Relationship of Chemical Composition to the Critical Temperatures of Low-Carbon Low-Alloy Steels," *Tetsu-to-Hagane*, vol. 51, p. 2006, 1965.
[134] S. Zaefferer, P. Romano, and F. Friedel, "EBSD as a tool to identify and quantify bainite and ferrite in low-alloyed Al-TRIP steels," *Journal of Microscopy*, vol. 230, no. 3, pp. 499-508, 2008.
[135] M. De Meyer, L. Kestens, and B. C. De Cooman, "Texture development in cold rolled and annealed C-Mn-Si and C-Mn-Al-Si TRIP steels," *Materials Science and Technology(UK)*, vol. 17, no. 11, pp. 1353-1359, 2001.
[136] R. Petrov, L. Kestens, A. Wasilkowska, and Y. Houbaert, "Microstructure and texture of a lightly deformed TRIP-assisted steel characterized by means of the EBSD technique," *Materials Science & Engineering A*, vol. 447, no. 1-2, pp. 285-297, 2007.

[137] S. Morito, Y. Adachi, and T. Ohba, “Morphology and Crystallography of Sub-Blocks in Ultra-Low Carbon Lath Martensite Steel,” *Materials Transactions*, vol. 50, no. 8, pp. 1919–1923, 2009.
[138] K. Davut and S. Zaefferer, “Statistical Reliability of Phase Fraction Determination Based on Electron Backscatter Diffraction (EBSD) Investigations on the Example of an Al-TRIP Steel,” *Metallurgical and Materials Transactions A*, vol. 41, pp. 2187-2196, 2010.
[139] R. H. Petrov, J. Bouquerel, K. Verbeken, L. A. . Kestens, P. Verleysen, and Y. Houbaert, “OIM Analysis of Microstructure and Texture of a TRIP Assisted Steel after Static and Dynamic Deformation,” in *Materials Science Forum*, 2010, vol. 638, pp. 3447–3452.
[140] E. Jimenez-Melero et al., “The effect of aluminium and phosphorus on the stability of individual austenite grains in TRIP steels,” *Acta Materialia*, vol. 57, no. 2, pp. 533–543, 2009.
[141] E. Jimenez-Melero et al., “Characterization of individual retained austenite grains and their stability in low-alloyed TRIP steels,” *Acta Materialia*, vol. 55, no. 20, pp. 6713–6723, 2007.
[142] J. R. Davis, *Metals Handbook. Desk Edition.* ASM International, 1998.
[143] A. F. Gourgues-Lorenzon, “Application of electron backscatter diffraction to the study of phase transformations: present and possible future,” *Journal of Microscopy*, vol. 233, no. 3, pp. 460-473, 2009.
[144] M. Calcagnotto, D. Ponge, E. Demir, and D. Raabe, “Orientation gradients and geometrically necessary dislocations in ultrafine grained dual-phase steels studied by 2D and 3D EBSD,” *Materials Science and Engineering: A*, vol. 527, no. 10-11, pp. 2738–2746, 2010.
[145] H. Beladi, G. L. Kelly, A. Shokouhi, and P. D. Hodgson, “The evolution of ultrafine ferrite formation through dynamic strain-induced transformation,” *Materials Science and Engineering A*, vol. 371, no. 1-2, pp. 343–352, 2004.
[146] S. Morito, H. Tanaka, R. Konishi, T. Furuhara, and T. Maki, “The morphology and crystallography of lath martensite in Fe-C alloys,” *Acta Materialia*, vol. 51, no. 6, pp. 1789-1799, Apr. 2003.
[147] H. ASM International, *ASM handbook Vol 03 - Alloy phase diagrams*, vol. 3. ASM International, 1992.
[148] L. Cheng and K. M. Wu, “New insights into intragranular ferrite in a low-carbon low-alloy steel,” *Acta Materialia*, vol. 57, no. 13, pp. 3754–3762, 2009.
[149] L. Cheng, A. Bottger, T. H. H. de Keijser, and E. J. Mittemeijer, “Lattice Parameters of Iron–Carbon and Iron–Nitrogen Martensites and Austenites,” *Scr. Metall. Mater.*, vol. 24, no. 3, pp. 509–514, 1990.
[150] H. Kitahara, R. Ueji, N. Tsuji, and Y. Minamino, “Crystallographic features of lath martensite in low-carbon steel,” *Acta Materialia*, vol. 54, no. 5, pp. 1279-1288, Mar. 2006.
[151] H. Kitahara, R. Ueji, M. Ueda, N. Tsuji, and Y. Minamino, “Crystallographic analysis of plate martensite in Fe–28.5 at.% Ni by FE-SEM/EBSD,” *Materials Characterization*, vol. 54, no. 4-5, pp. 378-386, May 2005.
[152] V. A. Yardley, R. Sugiura, T. Matsuzaki, S. Tsurekawa, J. Yokobori, and Y. Hasegawa, “Quantitative study of W-alloyed 9–12 Cr steel microstructures using EBSD,” *Strength, Fracture and Complexity*, vol. 5, no. 1, pp. 39–52, 2007.
[153] A. Lambert-Perlade, A. F. Gourgues, and A. Pineau, “Austenite to bainite phase transformation in the heat-affected zone of a high strength low alloy steel,” *Acta Materialia*, vol. 52, no. 8, pp. 2337-2348, 2004.

[154] B. Narayanan, L. Kovarik, M. Quintana, and M. Mills, “Characterisation of ferritic weld microstructures using various electron microscopy techniques: a review,” *Science and Technology of Welding &# 38; Joining*, vol. 16, no. 1, pp. 12–22, 2011.

[155] N. Gey, P. Blaineau, L. Germain, M. Humbert, D. Barbier, and A. Perlade, “Restitution of the Shapes and Orientations of the Prior Austenitic Grains from Inherited Alpha’ Orientation Maps in Steels,” *Solid State Phenomena*, vol. 172-174, pp. 911-915, Jun. 2011.

11 Appendix 1

11.1 Modeling of the thermal distribution in Sample 1500-1

Below is presented the result from the thermal modeling conducted for Sample 1500-1. The work was performed by Cem Celal Tutum from the Department of Mechanical Engineering, Technical University of Denmark. The work was not fully completed by the deadline of the thesis, therefore only selected results will be presented. The results, which are particularly supportive for the results of the thesis are:

- The peak temperature is estimated at 1100°C
- The duration of the heating cycle during is estimated at approximately 5 seconds for all weld zones.

Fig. 0-1 shows the calculated temperature distribution in the assumed geometry. Isothermals are projected onto a micrograph of sample 1500-1 in Fig.0-2. A good correspondence is observed between the location of the Ac_3 temperature as estimated from the micrograph and the isotherm for 980 °C, i.e. Ac_3 temperature estimated in Chapter 7 – "Microstructure evolution in Sample 1500-1". Comparing the location of the isotherm 760 °C, which corresponds to Ac_1 (see Chapter 7 – "Microstructure evolution in Sample 1500-1") with the microstructure, no match with the location of the Ac_1 temperature as estimated from the microstructure is observed. In the modeling procedure it was attempted to modify the cooling conditions at the bottom plate, but no significant improvement was obtained. The cause for the discrepancy, particularly in the bottom part, remains to be resolved.

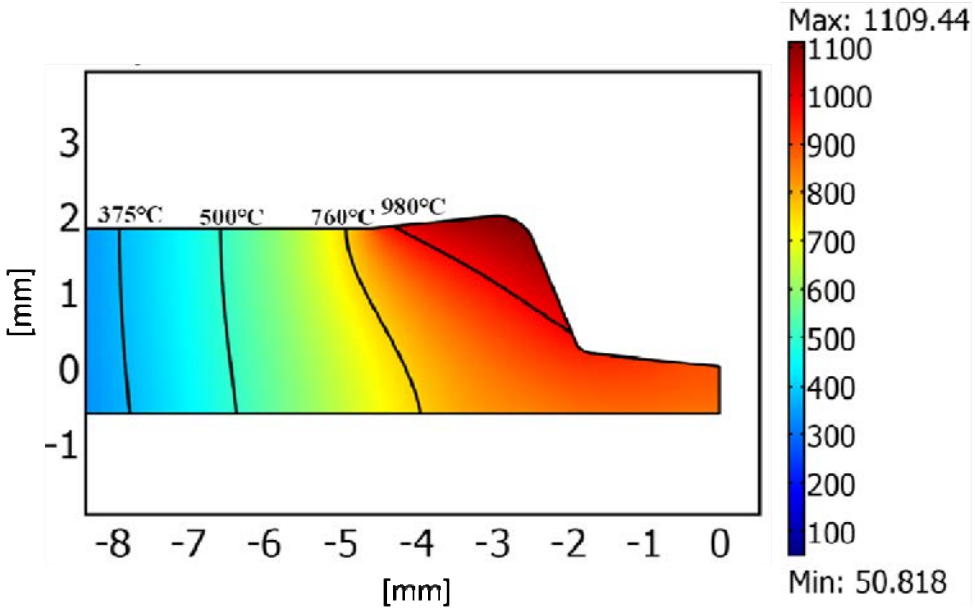

Fig. 11-1. Temperature distribution in Sample 1500-1.

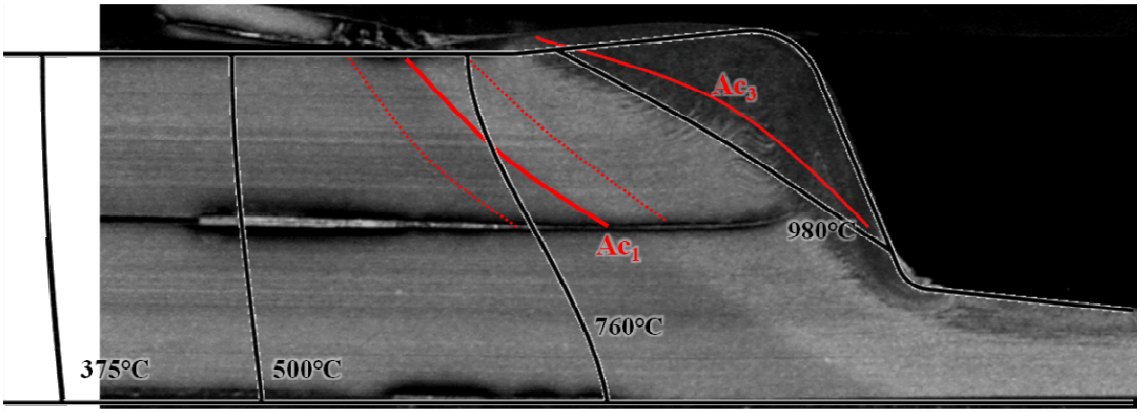

Fig. 11-2. Projection of isotherms onto a micrograph of sample 1500-1.

In Fig. 0-4 the temperature is given as a function of time at the locations given in Fig. 0-3. It is observed that it takes about 2 seconds to cool to a temperature below 300°C, after the tool is retracted. Consequently, the total time for heating of the sample is approximately 5 seconds.

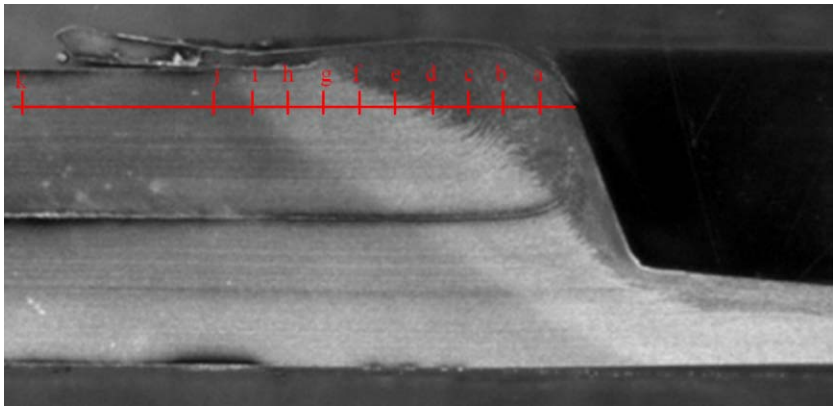

Fig. 11-3. Locations for curves giving the temperature as a function of time in Fig. 11-4.

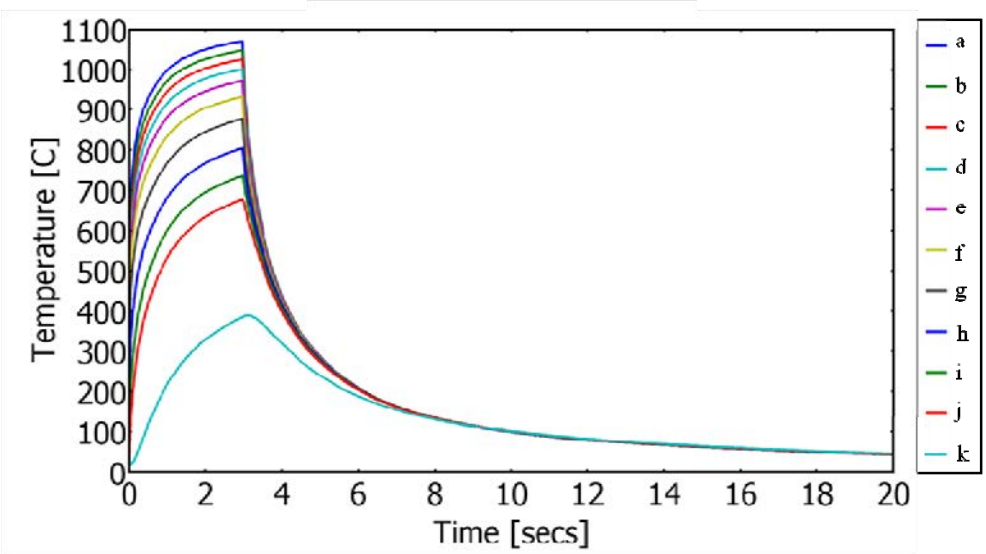

Fig. 11-4. Temperature as a function of time for the locations given in Fig. 11-3.